



The University of
Nottingham

UNITED KINGDOM • CHINA • MALAYSIA

**Design and characterisation of a label free
evanescent waveguide microscope**

REBECCA CHOI, MEng.

**Thesis submitted to the University of Nottingham for the degree of
Master of Philosophy
September 2014**

Abstract

This project aims to develop and characterise a label-free waveguide microscopy system as an alternative to objective-based total internal reflection microscopy to be applied in the qualitative detection of the adhesion of biological samples. The advantage of the waveguide system allows the use of lower numerical aperture objectives resulting in a larger field of view and a significant cost reduction. A LED illuminated waveguide system was developed in which light is coupled through a conventional microscope slide to produce total internal reflection at the glass-water interface. The evanescent field profile was characterised by displacing a tungsten tip from the glass/water interface and the scattered intensity from the tip was imaged using a low NA objective. A laser illuminated waveguide system was then developed and the microscope slides were modified by polishing the uneven edges, which allowed better control of the incidence angle and the evanescent field was characterised using the same method. To verify that the waveguide signal will only be detected when an objective is proximal to the surface, microspheres under Brownian motion were tracked under bright-field mode and laser waveguide mode. The evanescent field profile was best fitted with a double exponential, however, the evanescent field depth could not be defined due to the presence of an intensity offset of approximately 50% from the normalised intensity. The high intensity offset was reduced to 10% when the edges of the waveguide were polished and a collimated laser source was used. Under laser illumination, for high incident angles, the evanescent field profile showed deviation from the simple exponential function at short separation distances from the substrate. The evanescent field depth based on the best fitted function for incident angles 62.1° , 68.1° and 77.4° were $956\pm 55\text{nm}$, $366\pm 0.6\text{nm}$ and $211\pm 32\text{nm}$ respectively; demonstrating that the evanescent field depth can be controlled by changing the incident angle. Two out of seven tracked microspheres featured a coefficient of variation > 1 over time in the results of the waveguide mode and was not observed in the bright-field mode. The higher coefficient of variation was caused by an intensity spike when the microspheres moved in and out the evanescent field and confirms the validity

of the waveguide system. This system can potentially be compatible with standard tissue culture plastics and can be adoptable in an industrial manufacturing setting.

Acknowledgements

I am deeply grateful to my supervisors, Dr. Melissa Mather, Dr. Chung See, Prof. Mike Somekh, Dr. Virginie Sottile and Prof. John Crowe, for all the technical guidance and emotional support I have received. I have learnt a lot from you all.

Thanks to Ed for making the LED array and Stephanie for teaching me cell culture protocols. Also, I want to thank Jing and Suejit for holding my hand and guiding me through tough times. I would also like to thank Shivali, David and the person who claims to have done nothing, for proof-reading this thesis. Also, thank you to all the members of iBIOS, colleagues and friends in CBS and DTC in Regenerative Medicine. I really enjoyed your company.

I would like to thank my funding body, EPSRC, for which this work would not have been made possible without their support and Probe Technology for donating the tungsten probes that were used in the study.

Table of Contents

Chapter 1	Introduction.....	1
Chapter 2	Total internal reflection microscopy.....	5
2.1	Cell adhesion microscopy	5
2.2	Principle of evanescent field illumination	7
2.3	Materials and Methods.....	13
2.3.1	TIRM – Phase contrast microscopy system setup	13
2.3.2	Cell culture.....	13
2.3.3	Image processing	14
2.4	Results & Discussion	15
2.5	Conclusion	19
Chapter 3	Design and characterisation of LED illuminated waveguide evanescent microscopy	20
3.1	Introduction.....	20
3.2	Literature review on waveguide microscopy.....	21
3.2.1	Fluorescent waveguide systems.....	21
3.2.2	Label-free waveguide systems.....	23
3.3	Characterisation of the evanescent field profile.....	25
3.4	Materials and Methods.....	28
3.4.1	Waveguide	28
3.4.2	LED illumination setup.....	28
3.4.3	Evanescent field characterisation	29
3.4.4	Detection system.....	31
3.4.5	Image analysis	31
3.5	Results.....	32
3.6	Discussion	36

3.7	Conclusion	37
Chapter 4	Characterisation of evanescent field profile using laser illumination source	39
4.1	Introduction.....	39
4.2	Materials and Methods.....	41
4.2.1	Waveguide	41
4.2.2	Laser illumination setup	41
4.2.3	Evanescent field characterisation	42
4.2.4	Image analysis	43
4.3	Results.....	46
4.4	Discussion	55
4.5	Conclusion	59
Chapter 5	Tracking microsphere solution in bright-field and waveguide mode	60
5.1	Introduction.....	60
5.2	Materials and Methods.....	61
5.2.1	Experimental procedure.....	61
5.2.2	Hardware control	61
5.2.3	Image processing and single particle tracking.....	62
5.2.4	Analysing parameters from tracked objects	64
5.3	Results.....	66
5.4	Discussion	74
5.5	Conclusion	77
Chapter 6	Conclusion	78
6.1	Summary	78
	Bibliography	81
Appendix I	Derivation of evanescent field depth	87
Appendix II	Equations for three-layer transmittance model	90

Appendix III	Demonstration of the uneven surface of the waveguide edge	91
Appendix IV	Ray tracing inside waveguide for incident angle below the critical angle	93
Appendix V	Effects of analysis window size on the evanescent field depth	96
Appendix VI	Normalised mean intensity and standard deviation used to calculate the coefficient of variation in the three clusters	100
Appendix VII	Results for tracked particles 5, 6 & 7	101
Appendix VIII	Restriction of the incident angles produced by an LED source	105

Chapter 1 Introduction

The discoveries of more complex diseases have also resulted in the development of more complicated medicinal therapies. From chemically synthesised compounds and biologically produced recombinant proteins, to synthetic materials mimicking biomechanical structures, whole biological cells are now gaining regulatory approval to be used for therapeutic applications.

Currently, the Food and Drug Administration (FDA) has approved ten cell therapy products(1). These include Provenge® (Dendreon Corp., WA, US), an autologous treatment of prostate cancer using the patient's own modified T-cells(2), Carticel® (Genzyme Biosurgery, MA, US), an autologous therapy for cartilage repair(3) and other cord blood transplants to treat some forms of blood cancer, metabolic and immune system disorders. On top on this, other medical devices that are made of cells, such as Dermagraft® (Organogenesis, MA, US) and Apligraf ® (Organogenesis, MA, US) are skin grafts that have been on the market to treat venous leg ulcers and diabetic foot ulcers for over fifteen years(4,5). Furthermore, over 8000 clinical trials on cell therapy are currently open, indicating the high demand and potential for such treatments(6). In addition to using cells as a medicinal therapy, they are also used as a research tool for drug discovery, toxicology studies and modelling diseases(7–10).

As with many commercial products, the concept of quality is defined by the ability to manufacture a product consistently. This is determined by a number of factors including the source of the raw materials and the manufacturing processes. The FDA requires evidence detailing product safety, sterility, purity and identity prior to regulatory approval and the release of each batch on to the market(11).

The issue surrounding raw material occurs when the process involves the use of inconsistent material such as animal serum, which can vary between batches(12–14). Also, primary cells are known to alter their phenotype and genotype after a successive number of passages(15–19). In order to manufacture a product repeatedly, it is essential to minimise the number of

variables in the process and developments have thus been made towards serum-free cultures(20–24) and the creation of stable cell lines to overcome the problems of batch variation.

To ensure the manufacturing process is delivering the product as specified, quality testing is in place from the start, with raw materials, to sampling at various stage of the manufacturing process, to releasing the product batch at the end of the process. Current methods for cell characterisation can yield varying levels of cellular information; proteomic, genomic and transcriptomic studies are large studies that are possibly more useful as a reference for banking cell lines. For faster identity verification, only a certain number of phenotypes are recognised by measuring the expression of specific biomarkers, which are sets of molecules expressed by the cell that are involved in certain biological functions. Faster quantitative measurements of gene expression can be measured by RT-PCR and the corresponding protein expression can then be quantified using western blot(25).

Biomarker expression can also be quantified by various techniques that use monoclonal antibodies, due to their high specificity for certain biomarkers(26). Dyes or fluorescent labels are often attached to monoclonal antibodies to allow colorimetric or photometric measurements and this is utilised in methods such as immunocytochemistry, enzyme-linked immunosorbent assay (ELISA), fluorescent-activated cell sorting (FACS) and magnetic-activated cell sorting (MACS). These methods are used to determine cell identification and isolate different cell types within a mixed population(27). However, it is often the case where there is a lack of a putative biomarker and therefore other quantitative information are also used, such as cell size, cell morphology, and nuclei-to-cytoplasmic ratio(28). In addition, it has been reported that the phenotype may not correlate to the function of the cells and so functional assays could be a better indicator of product potency.

Due to the high specificity of antibodies, fluorescent labels can localise functional biochemical molecules. However, many of the fluorescent assays require the cell sample to be fixed, which means dynamic studies are not possible. Also, in cases where live cells fluorescent imaging is possible,

illuminating fluorescent molecules can cause phototoxicity to live cells and potentially compromising the results of the study(29–32). The disadvantages of using fluorescent labels can be avoided by using label-free methods, which quantify physical parameters using mechanical, electrochemical, acoustic and optical approaches. Optical imaging methods can provide highly resolved spatial information and is less invasive compared to the other techniques. In addition, optical imaging systems can gather real-time information of the cells with minimal disturbance during the manufacturing process; data can be gathered while the cells are inside the incubator. This can ensure the cells are as desired and problems such as contamination can be detected early, potentially reducing the quantity of end point assays where currently, extra portions of product are made and used for testing, which ultimately contributes towards the clinical cost of each patient.

The simplest optical technique to observe live biological cells is the bright-field microscope. However, image contrast is poor due to cells having a low absorbance. Dyes added to cells can enhance the contrast, but could also compromise their natural state as mentioned previously. Optical contrast enhancement can be performed by manipulating the amplitude and phase of the background and diffracted light at the back focal plane of the objective. Phase contrast microscopy was first described by Fritz Zernike in 1934 and has been extensively used in tissue culture laboratories to permit observation of live cells with enhanced contrast without polarisation or birefringence effects from tissue culture plastic. Detailed structures within the cytosol, cell morphology and nuclei-to-cytoplasmic ratio are also revealed.

Phase contrast can be easily implemented into existing microscopes by the addition of two components; a condenser annulus placed at the front focal plane of the condenser forming a ring of defocused light that passes through the sample, and a phase plate placed at the back focal plane of the objective, altering the amplitude and phase of the background and diffracted light. Light that has passed through the sample can either be non-deviated, which forms the background and is focused into a ring at the back focal plane of the objective where the phase plate lies, or diffracted in all directions and is focused across the entire back focal plane of the objective. At the back focal plane of the

objective, the background is a ring of illumination, which overlaps with some of the diffracted light. It can be considered as spatially separated from the diffracted light. Because the diffracted light is a result of passing through a structure of the cell that has a higher refractive index than its surrounding medium, the diffracted light is retarded in comparison to the background. The slight shift in phase causes a small change in amplitude, resulting in a low contrast bright-field image. By placing a phase ring at the back focal plane, the amplitude of the background is dampened by a layer of material that partially absorbs light and also, retards or advances the phase by a quarter of a wavelength, depending on whether it is a positive or negative phase contrast system. Since the image is the resultant of the background and diffracted light, shifting the phase by a quarter wavelength increases the amplitude difference and together with the dampened background, the overall contrast of the image is increased.

However, phase artefacts are also introduced causing halo effects surrounding the objects and so the intensity of the image does not correlate to the optical path length of the object. In addition, cell adhesion is a crucial process for cell growth, differentiation and survival, which is potentially a measurable criterion that can define cell quality(33–35) and techniques like phase contrast does not provide information at the interface between the cell and the substrate.

In the next chapter, optical techniques used to reveal cell adhesion are discussed and images taken using phase contrast combined with total internal reflection microscope (TIRM) system is presented. This system was built by Dr. Jing Zhang. Time-lapsed images of mesenchymal stem cells undergoing adipogenic differentiation and osteogenic differentiation were analysed qualitatively. In Chapter 3, the designs of waveguide systems reported in the literature are reviewed and methods to characterise the evanescent wave on the waveguide substrate are explored. An LED illuminated evanescent waveguide system is characterised and a high intensity offset was found. Chapter 4 describes a laser illumination waveguide system where the high intensity offset was significantly reduced and Chapter 5 concludes the feasibility of using the waveguide approach to detect cell adhesion and suggestions for future work are proposed.

Chapter 2 Total internal reflection microscopy

2.1 Cell adhesion microscopy

The importance of quality in cell-based products was previously discussed and the processes that occur at the cell-substrate interface can provide an additional layer of information to the current label-free optical approaches, which may be used to assess cell quality. Different optical systems used to image cell adhesion are discussed below.

In 1964, Curtis described an interference reflection microscopy (IRM) to determine the cell-substrate separation distance. The image was formed based on the interference of reflected light at different interfaces, but the image contrast was low and was later improved by using polarizers and antireflective objectives which included a quarter-wave plate to remove reflections inside the objective that could drown the signal(36,37). However, the interpretation of the result is difficult because the intensity of the interference signal can fluctuate as the separation distance increases. In order to determine the separation distance prior knowledge of the refractive index is required, but refractive index of the cell membrane is inhomogeneous, so great care must be taken during data interpretation(37).

The first report of total internal reflection microscopy (TIRM) was by described by Ambrose in 1956(38). The evanescent field was generated by a prism to illuminate the sample and an objective was placed on top of the prism to image the scattered light. Unlike IRM, the evanescent field decays exponentially from the interface in the orders of hundreds of nanometers, removing the ambiguity of distance dependent intensity fluctuations(39).

This technique was extended further by coating the prism with a thin metal film which causes electrons on the metal film to oscillate, known as surface plasmons(40,41). The electromagnetic field is further concentrated, resulting in increased sensitivity to binding events at the interface(40,41). In addition to the exponential decay perpendicular to the interface, surface plasmons also propagate parallel to the interface, and as result of this, the lateral resolution of the cell image is reduced significantly(42).

With the availability of high numerical aperture objectives, total internal reflection can be achieved through the objective resulting in images of cell adhesion with high lateral resolution. The principle of TIRM is discussed below.

2.2 Principle of evanescent field illumination

Evanescent fields are characterised by an exponential decay and it is this unique property that is being utilised in a number of important applications in the field of optics. The formation of evanescent fields can be achieved in a number of ways, by passing a beam of light through small apertures or diffraction gratings, or fulfilling the condition for total internal reflection between two mediums(43–46). TIRM, as the name suggests, produces total internal reflection at the interface between two media to result in the production of evanescent field illumination(38,39).

Two conditions must be satisfied for total internal reflection to occur. Light must strike the interface from a high refractive medium (n_1) to the low refractive medium (n_2) and the incident angle (θ_i) must be greater than the critical angle ($\theta_{crit.}$). The critical angle is dependent on the refractive index difference between the two media and can be calculated using Snell's Law in Eq. 2.1

$$\theta_{crit.} = \sin^{-1}\left(\frac{n_2}{n_1}\right)$$

Eq. 2.1

When a beam of light strikes the boundary of two dielectric media, a fraction of this light is transmitted through to the next medium and the remaining fraction is reflected back at the same incident angle. The amplitudes of the reflected light and transmitted light can be calculated using Fresnel equations. The evanescent field depth can be derived from the wave vector (k) triangles as shown in Appendix I.

Using Fresnel equations, the reflectance and transmittance between glass and water were calculated and plotted for a range of incident angles in MATLAB. The absolute values are displayed in Figure 2.1A and Figure 2.1B.

The reflectance for both s-polarisation and p-polarisation reaches unity beyond the critical angle, which shows that energy is conserved upon reflection. The real part of the transmittance is zero beyond the critical angle; however, due to the presence of the evanescent field, the imaginary part of the transmittance

reaches two at around 70.4° for s-polarisation and approximately 68.0° for p-polarised illumination.

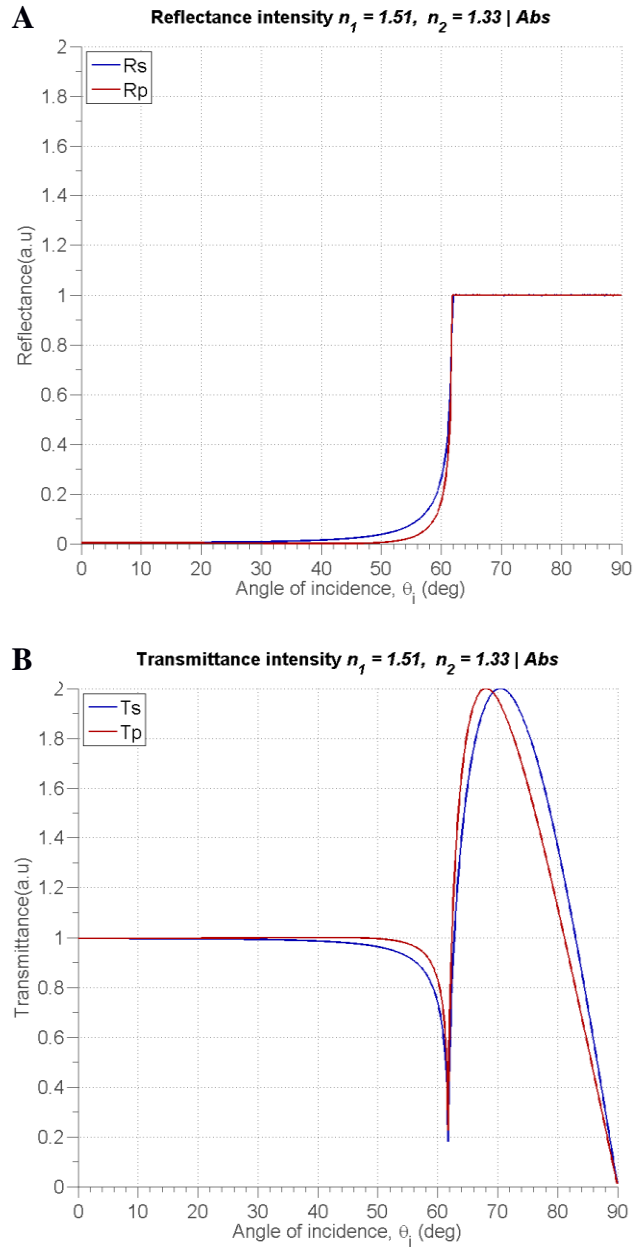


Figure 2.1 Absolute values of reflectance (A) and transmittance (B) intensities for glass/water interface. $\lambda_0 = 635\text{nm}$. Calculated using Fresnel equations, plotted on MATLAB.

The principle of evanescent field microscopy relies on the introduction of a sample with refractive index between the refractive indices of the two layers(38,39,43). If layer 1 has a refractive index of n_1 and layer 2 has a refractive index of n_2 , while both layers satisfy the condition of total internal reflection, the introduction of a sample with refractive index n_3 , where $n_1 > n_3 < n_2$, will perturb the evanescent field and scatter light in all directions; turning the confined standing wave in layer 2 to a propagating wave. This is also known as frustrated total internal reflection(43).

The amplitude reflection coefficient of a thin film (layer 2) between two semi-infinite isotropic dielectric media (layer 1 and layer 3) was solved by Försterling(47) by summing all the reflected amplitudes forming a geometric series. The sum of the geometric series to infinity is displayed in Eq. 2.2.

$$\Sigma E_r = E_i \left(\frac{r_{23}e^{i\delta} + r_{12}}{1 + r_{23}r_{12}e^{i\delta}} \right)$$

Eq. 2.2

Where,

E_i is the initial amplitude of the electric field

$$\delta = k\Delta l = \frac{2\pi}{\lambda} * 2n_2d \cos \theta_2$$

d is the thickness of the thin film

λ is the wavelength of the source

r_{12} , r_{23} are complex reflection coefficient between layers 1, 2 and layer 2, 3 respectively

Using this solution, Court & Willisen(48) derived the transmittance for evanescent field tunnelling. Layer 2 with refractive index of n_2 is sandwiched between two semi-infinite layers, layer 1 and layer 3, with refractive indices of n_1 and n_3 respectively. All three layers were assumed to be homogenous, lossless and dielectric. Figure 2.2 shows a schematic of this three layer model.

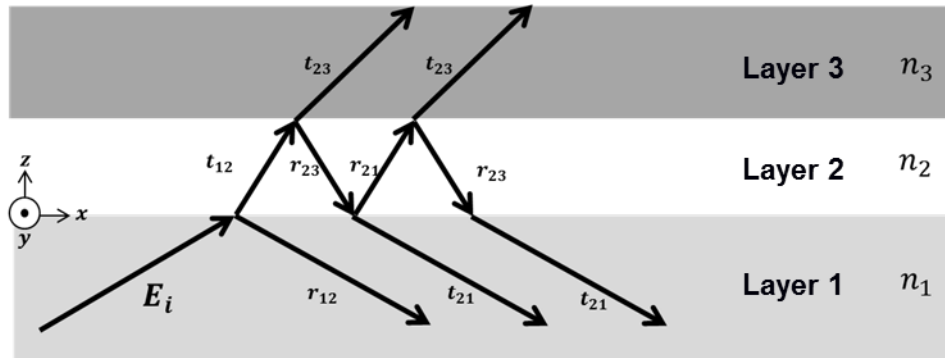


Figure 2.2 Schematic of the three layer model by Court & Willisen (48).

The set of equations derived by Court & Willisen(48) can be found in Appendix II . Figure 2.3 shows a plot where the transmittance is calculated for a range of incident angles; while the thickness of layer 2 is increased (i.e. layer 3 is displaced further away from layer 1).

Figure 2.3 illustrates that as layer 3 is displaced from layer 1, for incident angles below the critical angle, more frequent fluctuations are observed for s-polarised than p-polarised illumination. At the critical angle between layer 1 and layer 3 (67.9°), the transmitted intensity is zero; beyond this incident angle, at zero displacement, an intensity of 200% is shown for incident angles ranging from 72.5° to 75° . For incident angles beyond $\sim 75^\circ$, the maximum intensity is not at zero displacement, but within the first 200nm. Based on the conservation of energy, the 200% shown in the figure represents the evanescent field travelling up and down the layer 3 and it is twice the energy relative to the energy at the transmitted beam at layer 1/ layer 2 interface.

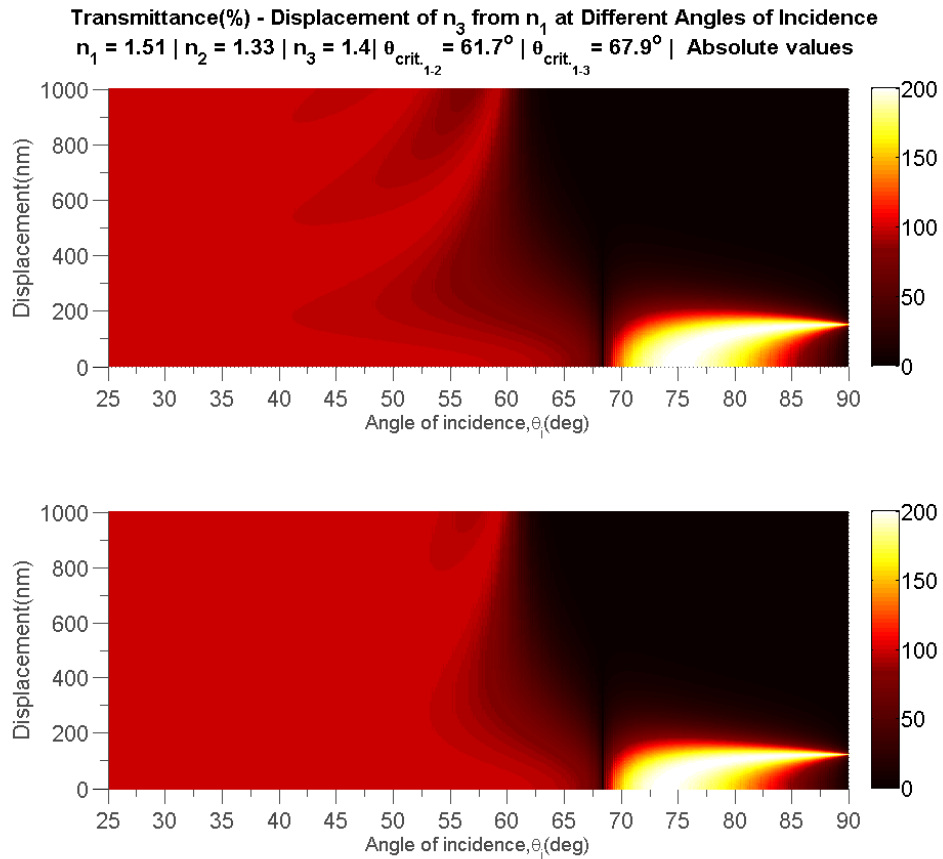


Figure 2.3 Transmittance in layer3; Displacement of layer 3 with refractive index of n_3 from layer 1 with refractive index of n_1 vs. the incident angle for s-polarised (top) and p-polarised (bottom) illumination. The refractive index of 1.4 was chosen for n_3 because it was in between the values of n_1 and n_2 and also, refractive index of 1.4 can be found in a cell.

The result above suggests that high transmittance in layer 3 is expected when the incident angle is slightly beyond the critical angle of layer 1 and layer 3. This is part of the mechanism of that TIRM utilises to create high contrast images. A higher transmittance also mean that light is more likely to transmit through to the next medium than a lower transmittance; i.e. light will transmit through an object with refractive index of n_3 . Capturing this with an objective from below the sample will produce a dark object and the area where the evanescent field is unperturbed, total internal reflection is satisfied resulting in a bright background.

In contrast to TIRM, total internal reflection fluorescence (TIRF) systems relies on illuminating the excitation source at an incident angle further away from the critical angle to produce a low evanescent field depth, which minimises the excitation of fluorophore located further away from the surface.

In addition, a high NA objective (>1.33) is used to allow incident angles beyond the critical angle to be focused onto the sample, which results in total internal reflection through the objective. Also, a low depth of field is produced to capture a thin focused section that eliminates scattered light from distances far away from the surface focused onto the image. The depth of field for 1.49NA objective using a light source of $\lambda = 635\text{nm}$ is approximately 430nm, by comparison, a low powered objective with 0.4NA yields a depth of field $\sim 4\mu\text{m}$.

To demonstrate the principles of TIRM microscopy, a TIRM-Phase contrast microscopy system built by Dr. Jing Zhang (unpublished work) was used to image differentiating mouse mesenchymal stem cells into adipocytes and osteoblasts. Images were qualitatively analysed to show the response from TIRM compared to the standard phase contrast microscopy.

2.3 Materials and Methods

2.3.1 TIRM – Phase contrast microscopy system setup

The system used two high powered LEDs of different wavelengths to separate each imaging mode. A red LED ($\lambda_{centre} = 660nm$, M660L3, Thorlabs, UK) was used to illuminate the TIRM branch of the system and a blue LED ($\lambda_{centre} = 455nm$, M455L3, Thorlabs, UK) was used for phase contrast images. Total internal reflection was achieved by placing an annulus in the back focal plane of the objective to allow a range of incident angles just beyond the critical angle to pass into the objective. The same 60x/1.49NA objective was used to collect the signal from both imaging modes and the signals for each channel were separated by placing filters in front of the four detectors; two field of views per channel. Köhler illumination was employed in both imaging modes to achieve even illumination across the sample. A schematic of the setup is displayed in Figure 2.4. Cells were kept in an incubator at 37°C, 5% CO₂ during the imaging process. Exposure time was 500ms for both imaging modes. An objective warmer was used to minimise the focal drift caused by the heat coupling through the immersion oil into the objective. Four CCD camera in total were used to image the two imaging modes, with one camera for small field of view (for both modes, 1.4MP, PL-B955, PixeLINK, Edmund Optics, UK) and one camera for large field of view per mode (for TIRM, 1.9MP, PL-B958, PixeLINK, Edmund Optics, UK; for phase contrast, 2MP, PCO.2000, PCO., DE).

2.3.2 Cell culture

Mouse mesenchymal stem cells were cultured on imaging dishes (μ -Dish 35 mm, iBidi, DE) using DMEM medium, 10% foetal calf serum, 1% glutamate, 1% non-essential amino acids, 0.5% penicillin/streptomycin antibiotic mix. The cells were rested for two days after seeding at 3000cells/ml; media was changed on the third day into adipogenic or osteogenic medium and the same type of medium was used throughout the course of differentiation. Media was changed every two days and the imaging dishes were kept in standard incubators prior to and after imaging. Images of each media condition were taken for 15minutes each day for 9 days.

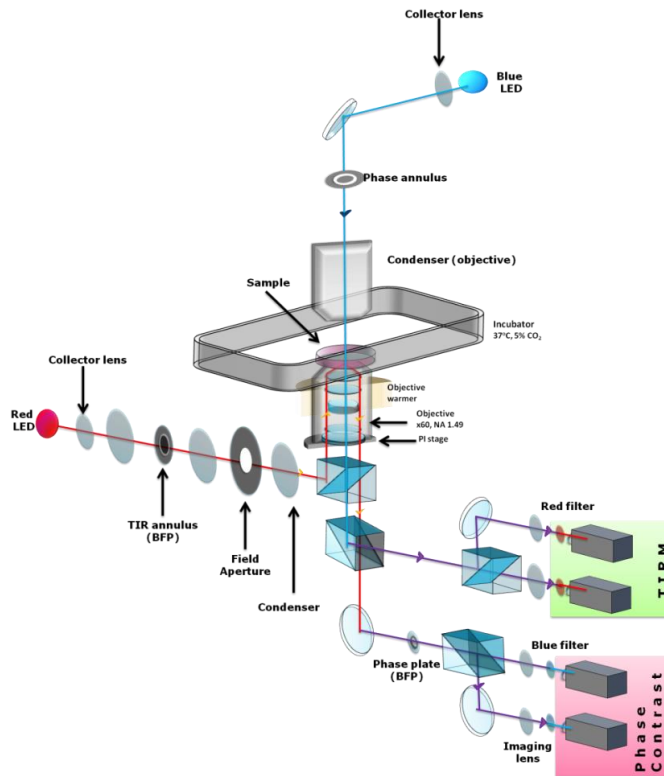


Figure 2.4 Schematic of the TIRM-Phase contrast system setup

2.3.3 Image processing

Image contrast was enhanced by histogram equalisation on every 8 by 8 tiles of the image. Area coverage of the cells on TIRM images was measured by taking the threshold of the cells and the number of pixels was counted. An example is shown in Figure 2.5.

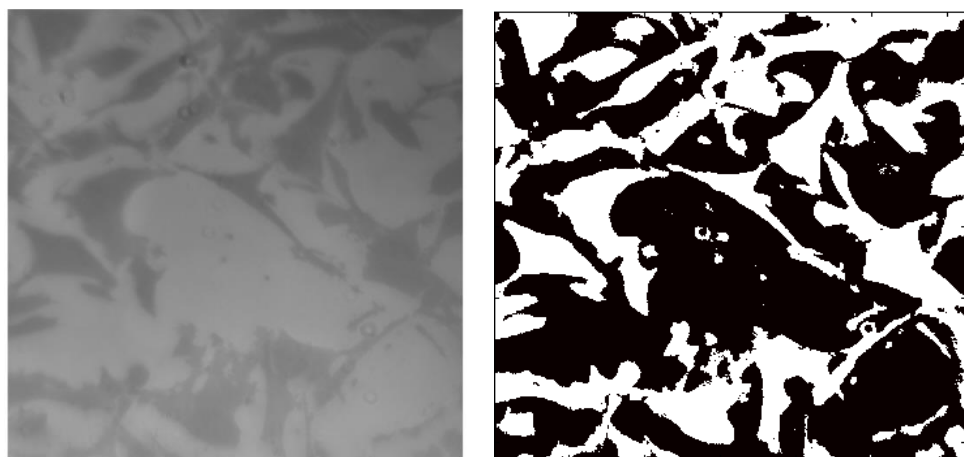


Figure 2.5 Original image (left) and the threshold image (right). The white pixels were counted as the area covered by the cells.

2.4 Results & Discussion

The process of osteogenic differentiation is displayed in Figure 2.6; from day 4 onwards, the images captured using the phase contrast channel showed full confluency, whereas in the TIRM channel, distinct areas of the cellular footprints are displayed. This suggests that not the entire cell body is attached to the surface. As the differentiation progressed, the borders of the cells also appeared less clear and fewer cells adhered to the surface. At day 11, dark fibrous structures were observed; appearing darker and more focused than cells, which suggests these fibrous structures were beneath the cells. A possible explanation for this is the extracellular matrix laid down on the surface by the cells forming a layer, making it more difficult to focus on the cells above.

Similarly, the confluency appears to be higher in the phase contrast channel than TIRM during adipogenic differentiation (Figure 2.7). Bright circular spots were observed from day 7 in the phase contrast channel, but appeared as dark spots in the TIRM image. These circular spots are thought to be lipids accumulated in adipocytes and are not always observed in the TIRM channel, because lipids are less dense than water, so they can float above the depth of focus. Unique streaks traversing the entire section of the cell can be seen during day 6. The long thin shape of the streaks suggests that they could be microfilaments of the cell, but further study using techniques such as fluorescent labelling the cell for actin and imaging using TIRF could be used to confirm the identity of the streaks. The streaks appeared one day before the appearance of the lipids, which suggests that the streaks could be an indicator during the adipogenic differentiation. The cells appear to be less confluent by day 11 compared to day 7, as they tend to lift off the surface once differentiated into adipocytes.

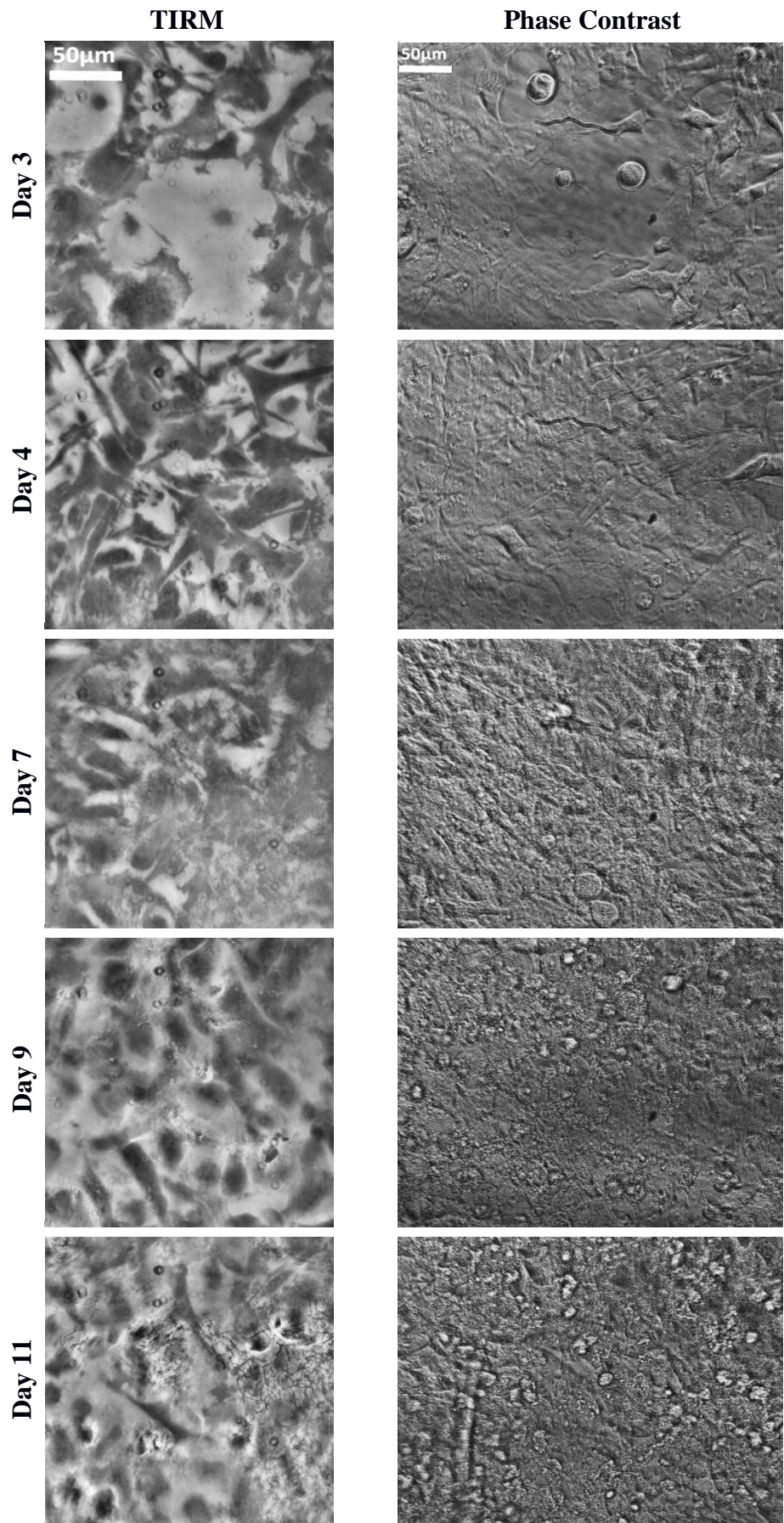


Figure 2.6 mMSCs under osteogenic differentiation; TIRM images (left) and the corresponding phase contrast image(right).

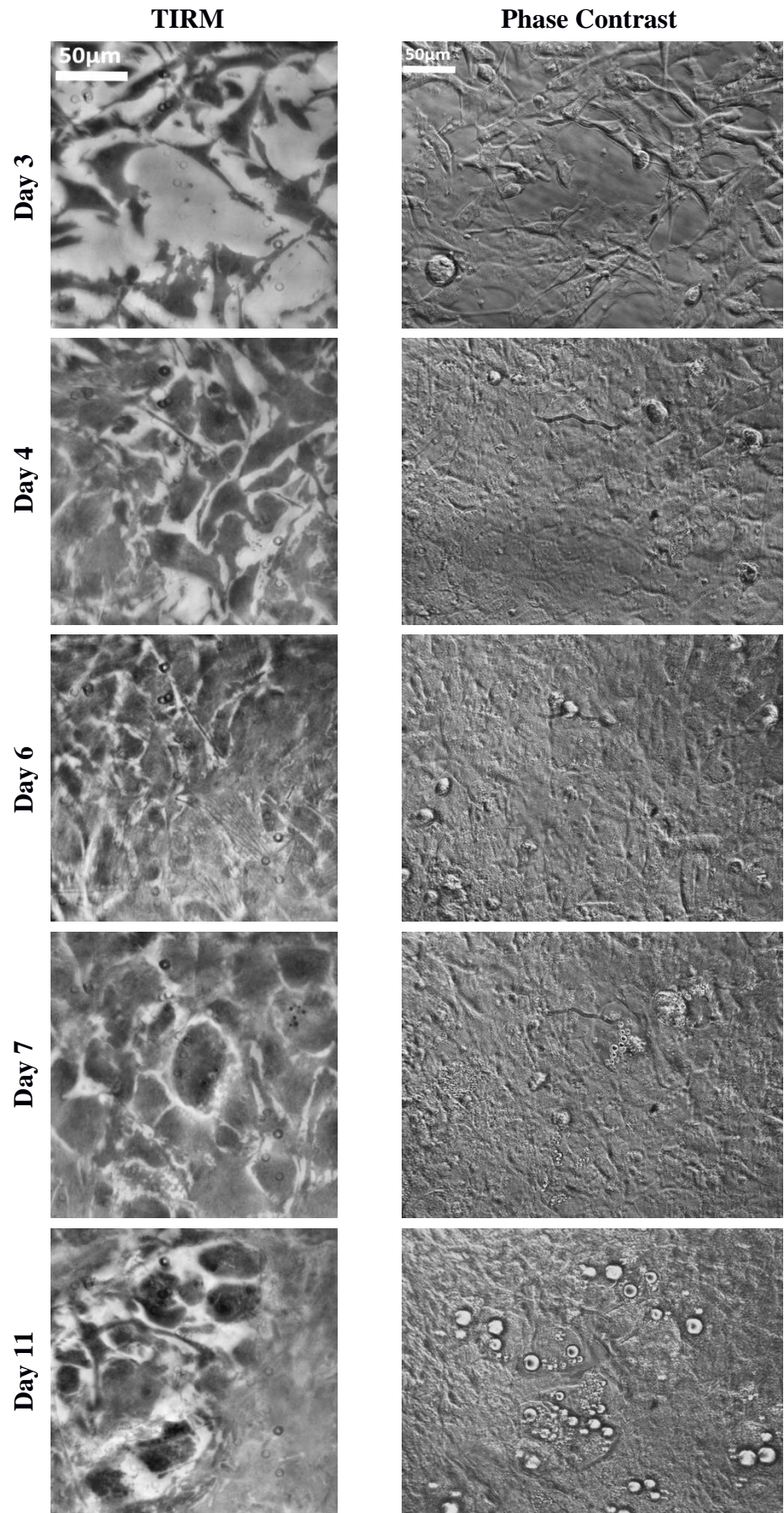


Figure 2.7 mMSCs under adipogenic differentiation. TIRM images (left) and the corresponding phase contrast image(right).

The area coverage by cells during differentiation measured using the TIRM channel is shown in Figure 2.8. Under adipogenic differentiation (blue), a sharp increase of the area coverage is observed from day 6 to day 7. Examining the TIRM images in Figure 2.7, the area covered by the cells on the images does not appear to have such a big difference (difference of ~30% in Figure 2.8), which suggests that the segmentation was not effective on the image for day 6. The cells on day 6 of differentiation appeared inhomogeneous in terms of grey scale values, which can cause a decrease in area coverage after segmentation based on grey scale values and hence, a sharp increase in area coverage on day 7, where the grey scale values are more homogenous within the cells.

During osteogenic differentiation (red), the area coverage was decreased towards the end of differentiation. This is due to cells lifting off from the surface as lipids accumulate inside the cell. Further, fibrous structures within the extracellular matrix layer beneath the cells are observed in day 11 and similarly, the segmentation process has resulted in higher area coverage than day 10.

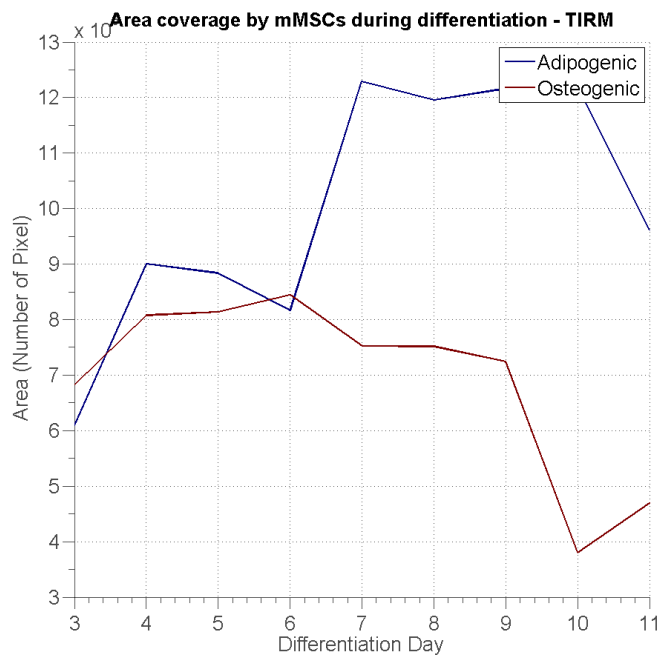


Figure 2.8 Area covered by cells in the TIRM channel under adipogenic and osteogenic differentiation. Data from single experiment.

2.5 Conclusion

Images from the TIRM channel have revealed an additional layer of information that cannot be acquired in the standard phase-contrast microscopy. The interaction between cell and the substrate can be studied using TIRM which shows the potential of using this technique for cell characterisation. The distinct spatial patterns formed at various stages of differentiation could be used as a blueprint to determine the level of differentiation and this is likely to be specific to a certain cell lineage or cell type. However, the data presented was only a single experiment and further studies should be conducted to verify the results.

Focal drift was present throughout the study because the heat from the incubator was coupled to the objective through the immersion oil. The effect was reduced by placing an objective warmer around the objective, but the effect was still significant. The cost associated with a high NA objective system and the narrow field of view have driven the development of a waveguide based system which is discussed in the next chapter.

Chapter 3 Design and characterisation of LED illuminated waveguide evanescent microscopy

3.1 Introduction

The availability of high numerical aperture objectives has enabled the formation of evanescent wave through the objective. Such imaging system results in the production of high lateral resolution images and the axial resolution is beyond the diffraction limit as illustrated in the previous chapter. This facilitates studies where the resolution of the image is of importance such as the morphology of the cellular footprint, the movement of intracellular organelles and single vesicle tracking.

However, as a manufacturing tool for quality assessment, using a high numerical aperture objective may not be the most suitable choice because of the small working distance which restricts the thickness of the substrate to 0.15-0.17mm where traditional cell culture T-flasks are about 2mm. At the moment of writing, long working distance objectives are commercially available up to a numerical aperture of 0.9. This means thin culturing flasks will need to be manufactured in order to be functional with high numerical aperture objectives. High numerical aperture objectives have high resolving power, but will also compromise the field of view of the image where only a small field is visible without aberrations. A small field of view is not an issue when the feature of interest is within the view. However, for manufacturing purposes such as the detection of contamination that has the potential spread across the culture, a system with a larger field of view will be beneficial for earlier detections.

The disadvantage of reduction in the field of view, the practical difficulties of using thin substrates in a manufacturing setting and the high cost associated using a high numerical aperture objective, have led to the development of waveguide microscopy. The advantages of waveguide microscopy include the formation of evanescent field across the surface of the waveguide, which results in larger area of illumination and the use of low NA objective to reduce the cost and increase the field of view, but as a result, the quality of the images

will also be compromised. Various groups have reported the development of fluorescence waveguide microscopy as an alternative for total internal fluorescence microscopy and these are reviewed in the following section.

3.2 Literature review on waveguide microscopy

The purpose of this review is to explore the type of waveguide systems that have been reported in the literature. The review is divided into fluorescence systems and label-free systems. Other specification of the system such as the type of illumination source and the type of signal detected by the system are noted. The illumination source can be coherent, i.e. lasers, where the bandwidth is low ($\pm 0.05\text{nm}$), the divergences of the rays are low and can easily be collimated to change the incident angle. Incoherent sources such as LEDs have wider bandwidths, typically $\pm 30\text{nm}$ and are more difficult to collimate because the source is large (an extended source), incident angle is a range of angles. The signal recorded can be in the form of an image produced by placing an objective perpendicular to the illumination direction, or the intensity of coupled light inside the waveguide can be monitored.

3.2.1 Fluorescent waveguide systems

Grandin et al.(49) reported a waveguide excitation fluorescence microscopy system that can be used to detect ligand-receptor binding events and focal adhesion points formed by cells attaching to the surface of the substrate. The system used a mono-mode laser as the excitation source, which was coupled into fibre optic cables with a collimated lens at the end of the cable. The collimated beam was aligned to an optical grating, which coupled the light source into the waveguide layer. The fibre was attached to a goniometer to allow the change of incident angle and a photodiode was placed at the end of the waveguide to monitor the coupling efficiency. The detection system including microscope objectives from x5 to x40 and CCD detector, were placed below the waveguide, perpendicular to the coupling light direction. Comparing the focal adhesion points of fibroblast cells stained for vinculin under epi-fluorescence and evanescent field excitation, the signal to noise ratio was increased by a factor of eight. However, artefacts within the waveguide itself resulted in dark lines across the fluorescence images and the homogeneity of the excitation illumination remains uncertain.

Another fluorescence system was reported by Haasanzadeh et al.(50) using $\text{Na}^+ \rightarrow \text{Ag}^+$ ion-exchanged waveguides. Similarly, the system utilises a grating to couple the laser source into the waveguide and the detection optics was placed perpendicularly below the waveguide to gather the fluorescence emission signal. They were able to characterise the evanescent field depth and calibrate the normalised intensity of the mode numbers with the separation distance from the interface(50,51). Based on the calibration, the separation distance for different surface contact points of a MC3T3-E1 cell were identified. However, a long exposure time of 26 seconds was reported on the evanescent field excitation image.

In a follow up study, images of HEK293 cells under waveguide evanescent field excitation and TIRF were compared(52). Focal adhesions were apparent in both type of illumination, but the authors have noted that there were scattered light from the waveguides that has caused epi-fluorescence signals mixed within the images. The resulting image displayed a weak outline of the entire cell and hazy cell information in the cytosol; the contrasts of focal adhesions were lower in comparison to TIRF images. The authors argued the additional information yielded from the scattered light was advantageous for dynamic studies because a TIRF system will need to take two images using two different incident angles to obtain the same information. In a more recent study, it was suggested that the outline of the cell can be removed by using a lower integration time(53). However, the high contrast of the TIRF system may be a result of the 100x/1.45 NA objective, which has a narrower depth of field in comparison to the 40x/0.9 NA objective used in waveguide system. Furthermore, the study did not use the same cell to compare the TIRF and waveguide imaging modes. Perhaps, it was the nature of the waveguide that was fabricated on a thick glass slab which exceeded the working distance of the TIRF objective and coverslips thickness was not suitable for the waveguide system, so no direct comparison between the two system on the same cell was made, but only cells of the same cell line was compared.

Agnarsson et al. (54) fabricated symmetric waveguides by matching the waveguide support layer with an optical polymer with the aqueous sample layer. Detection was from above the sample, using a 63x/1.2NA water-

immersion objective, fluorescence images of fixed cells were compared to images taken using confocal laser scanning microscopy and epi-fluorescence microscopy. An increased intensity was found at areas where the cell membrane is closer to the surface.

A LED illuminated waveguide fluorescence microscopy system was described by Ramachandran et al.(55). Six high powered LEDs were placed around a high reflective index circular cover slip, $n = 1.78$, to produce evanescent field on the surface which can excite fluorescent samples. Black rubber O-rings and light barriers were placed around the sample to avoid unwanted light entering the objective and direct illumination of the sample. However, the evanescent field depth was incorrectly determined as distance when the intensity reduces to 37% ($1/e$) of the maximum intensity, where it should have been 13.5% ($1/e^2$) of the maximum intensity instead. This is because the evanescent field depth is defined by the distance between the maximum amplitude and its decay to $1/e$ and since, the intensity is proportional to the square of the field amplitude, to determine the evanescent field depth using intensity values, the distance between the maximum intensity and its decay to $1/e^2$ should be taken. Applying the definition of evanescent field based on the decay of intensity to $1/e^2$, the evanescent field depth is $>900\text{nm}$ (beyond the axis on the figure displayed), instead of the reported 200nm . Despite the deeper evanescent field depth, substantial reduction of hazy signals within the cells was observed when compared to epi-fluorescent images of the same cell.

Most fluorescent waveguide systems used coherent illumination sources and optical gratings to couple the source into the waveguides apart from one system(55).

3.2.2 Label-free waveguide systems

Thoma et al.(56) used scattering waveguide microscopy to characterise thin films. The system used a laser source that was fixed to an optical table and the ion-exchanged slab waveguide together with the objective and camera were mounted on a rotation stage that allowed light to be coupled into the waveguide by rotation. The camera was placed perpendicular to direction of illumination to detect the scattered light. The system was able to resolve grating structures

of $<1\mu\text{m}$ using a 0.9NA objective and the image contrast of 40nm photoresist grids was increased as the mode number increased. The contrast was higher using s-polarisation than p-polarised illumination. Images taken using conventional dark-field microscope was reported to be weak in comparison to the ones produced under evanescent field illumination.

Reverse waveguides were described in a series of studies by Horvath et al.(57–59). Generally, waveguides are composed of a high refractive index guiding layer sandwiched in between two lower refractive index mediums. The medium on the bottom, called the substrate, onto which the waveguide is fabricated, normally has a higher refractive index than the medium on top of the guiding layer, called the cover layer, where the sample is normally in an aqueous solution. This yields an evanescent field penetrating the first 100–200nm of the cover layer, but because the source is guided in the guiding layer and the refractive index difference between the substrate and the cover layers, an evanescent field also exists on the substrate side which is longer and more intense than the cover side. By reversing the refractive indices between the cover and substrate layers, so that the refractive index of the cover is higher than the refractive index of the substrate, the sensitivity was improved by five-fold and the evanescent field was seven times deeper in TM mode(60).

In their live cell attachment experiment, the waveguide was mounted onto a rotation stage to change the incident angle of the laser which was aligned to the coupling gratings. The intensity coupled inside the waveguide was monitored using a fibre coupled photoreceiver at the end of the waveguide. Significant changes in the intensity peak area and peak shape were observed during cell sedimentation and attachment(60). They were also able to distinguish the difference between microexudate secretions by cells, filopodia formation and the amount of cell spreading by monitoring the in-coupling peak width and position(60,61).

An incoherent source was implemented in the system reported by Hill et al.(62). White light was coupled through a fibre optic cable into the rough edge of a glass microscope slide and images of plasmonic structures showed an increased contrast from conventional dark field microscopy and the polarisation can be

easily altered by placing the fibre optic cable at different positions around the microscope slide (62). Cell adhesion was quantified based on the intensity coupled inside the label-free waveguide, but this lacks the spatial information of the cells. Optical gratings can be avoided by coupling the light source from the side of the waveguide.

A simple system was built to image cell adhesion using an LED array as the illumination source. In contrast to TIRM, the image is formed by detecting the scattered light from cells close to the substrate. It is a darkfield technique where a bright signal is detected over a dark background. This is analogous to placing an annulus at the conjugate back focal plane of the TIRM objective so high incident angle are blocked to form the dark background and scattered light from the sample can be imaged.

The system built in this study aims to detect cell adhesion and it is essential to establish the distance between the cell and substrate for a response to occur. Characterising the evanescent field can quantify the thickness of the sensing layer. There is a large amount of literature on determining the evanescent field and this is briefly reviewed in the next section.

3.3 Characterisation of the evanescent field profile

Many examples of evanescent field depth characterisation in an objective based TIRF system can be found within the literature and it has been used to ensure TIRF systems can reproduce penetration depths for different experiments.

In the study by Steyer and Almers (63), fluorescent beads were adsorbed onto a curved lens surface and the lens was placed on top of a cover glass. Images of z-stacks were taken under epi-illumination where the beads came in and out of focus and the height of the bead was determined based on the maximum intensity of the bead through the z-stack and the initial bead adhered to the surface. This was compared to a z-stack of TIRF images and a plot between the height of the bead and the normalised intensity of the bead produced a single exponential profile. Although this method does produce a profile of the evanescent field, however, it relies on the difference in height between the centre of the first bead on the interface and the centre of the subsequent beads further away from the interface which meant there will always be a gap

between the interface and the radius of the bead on the interface. The study used beads with a radius of 140nm which implies their results were always the tail of an exponential decay with the profile of the first 140nm omitted. Improvements could be made by using smaller beads to minimise the gap between the interface and the centre of the surface bead.

Another study using fluorescent beads was reported where images of low refractive index fluorescent silica beads in matched index medium was used to prevent the scattering of excitation light(64). On contrary to the theoretical predictions and results from the study by Steyer and Almers(63), they found a double exponential profile, composed of a fast and slow decay components, which corresponded to 90% and 10% of the signal respectively at small separation distance to the substrate. The slow decaying component was attributed by scattered light within the objective and the authors noted that a double exponential was only a mathematical convenience where the slow decay component could be fitted with other functions. A small scattering signal was detected in both 1.4NA and 1.6NA objectives. Similarly, a double exponential was also found when the evanescent field depth was measured by displacing a fluorescent bead which was attached to the end of an atomic force microscopy (AFM) tip in the study by Ramachandran et al.(55). A high precision AFM scanner controlled the displacement of the tip and images at different displacements from the surface were captured and analysed. However, contrary to the results of Matthesyses and Axelrod(64), the intensity of the slow decay component at the surface was 30% of the full intensity instead of the reported 10%. The difference between the two studies was the illumination source; LED source was employed in the system reported by Ramachandran et al. and laser illumination was used in the system reported by Matthesyses and Axelrod. The different measurement methods used may also be a factor that contributes to the different results.

Another study used a tilted in-vitro generated fluorescent microtubule to characterise the evanescent field(65). One side of the microtubule was attached to the coverslip and the microtubule was tilted at an angle which was exposed to non-uniform evanescent illumination. Images of the TIRF and epi-illumination of the microtubule was used to determine the tilt angle and again,

a single exponential evanescent profile was found before and after accounting for two factors. One was the height dependent collection efficiency, which was corrected using an epi-illuminated vertically scanned image stack and the second factor was the point spread function in the z-direction, because the microtubule was tilted and was defocused along the axis of the microtubule.

Sarkar et al. (66) built an atomic force microscope combined with total internal reflection fluorescence microscope system, which produced a single exponential decay of the evanescent profile for various incident angles by scanning a quantum dot covered AFM tip along the z-axis. Another evanescent wave AFM system by McKee et al.(67) measured scattered light intensity using spherical particles with a radius ranging from 1-10 μ m and a sharp pyramid tip with radius of curvature below 60nm. The evanescent wave was generated by total internal reflection on a borosilicate prism between a flat surface and an aqueous solution and the AFM was used to accurately position the scattering objects. The study found exponential profile at larger separation distance from the interface when a spherical glass particle attached to the end of a tipless cantilever was used. Similarly, the results could be fitted with the sum of two exponentials. However, a pure exponential profile was found when a sharp pyramidal tip was used as the probe. The study also reported the polarisation of the illumination also affected the scattered evanescent wave profile. There was more deviation from the exponential function under s-polarisation than p-polarisation when borosilicate glass sphere was used. While the opposite response was observed when polystyrene glass beads was used to probe the evanescent field. The deviation from the exponential decay was explained by interference from reflections between the layers which was previously derived by Court and Willisen(48).

Within the reviewed literature, label-free methods were used to detect cell adhesion(60,61), but the result lacks spatial information of the adhesion process. Hence, a similar approach to the fluorescent system reported by Ramachandran et al.(55) can be applied to label-free cell adhesion studies. In this study, a conventional glass microscope slide was used as a waveguide and an LED array was used as the illumination source to generate evanescent field at glass/water interface. The evanescent field profile was characterised by

measuring the scattered light of a tungsten probe as it was displaced away from the glass/water interface. To change the depth of the evanescent field, an aperture array was placed in front of the LED to restrict the incident angle.

3.4 Materials and Methods

3.4.1 Waveguide

Glass microscope slides ($n=1.51$, 73mm by 23mm by 1mm thickness, Menzel-Gläser, Thermo Scientific, UK) with a cut edge finish were used as waveguides. A 200 μ l drop of distilled water was placed on the top surface of the unmodified planar waveguide and the evanescent field profile between glass/water interface was measured.

3.4.2 LED illumination setup

An array of 16 unpolarised surface mounted LEDs with a central wavelength of 525nm (bandwidth: ± 30 nm, KPHM-1608ZGC, KingBright, Farnell, UK) were used as an illumination source. The LEDs were mounted onto a custom made printed circuit board and was made by Dr. David Morris. The full width half maximum of the divergence angle was 120 $^\circ$ and the illumination profile could be considered as Lambertian. Baffles were placed on all sides on the LEDs to block any uncoupled light and to act as a holder for the waveguide.

In one condition, the LED array was placed directly next to the edge of the waveguide and since the thickness of the waveguide is 1mm, this acts as a 1mm aperture. In the second condition, the incident angle range was restricted by placing an aperture array with a thickness of 1mm and 16 apertures of 0.8mm diameter between the light source and waveguide. The 1mm thickness also meant the light source is displaced 1mm away from the edge of the waveguide. A schematic of the setup is shown in Figure 3.1.

To verify the incidence angle range, the pattern of a single aperture was projected onto a screen. The measured angle of incidence, θ_i , was 72.8 $^\circ$ and was higher than the designed value of 65 $^\circ$. The effect of the aperture size and displacement against angle of incidence is displayed in Figure 3.2.

3.4.3 Evanescent field characterisation

The evanescent field depth was probed in the z-direction, perpendicular to the waveguide surface, using a tungsten tip with curvature radius $0.5\mu\text{m}$ (Model 7B, Micromanipulator, NV, US) mounted onto a closed loop feedback piezoelectric stage (TSG001 & TPZ001, ThorLabs). A fine tip was chosen to act as a single point scattering object. The surface of the waveguide was placed in the focal plane of the objective and images were captured as the tip was lowered onto the surface without changing the focus. The exposure time was 400ms. An image was captured at every 25nm step displaced away from the surface. The evanescent field was probed across glass/liquid interface and glass/air interface.

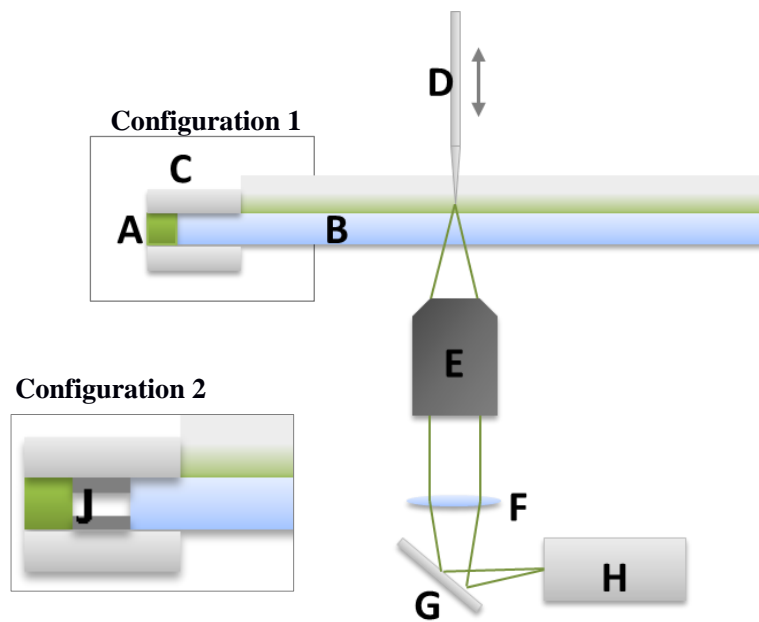


Figure 3.1 Schematic of the LED system setup. Configuration 1 is the 1mm aperture setup as the waveguide thickness is 1mm. Configuration 2 is the 0.8mm aperture setup. A - 525nm LED array. B - Glass waveguide. C - Baffles to block uncoupled light and to hold waveguide. D - $0.5\mu\text{m}$ tungsten probe controlled by piezo-electric stage. E - X8 0.18NA objective lens. F - Tube Lens $f=180\text{mm}$. G - Mirror. H - 12-bit monochrome CCD. J - Aperture array placed between LED array and edge of waveguide. The aperture is 1mm thick, so the waveguide is displaced 1mm away from the light source.

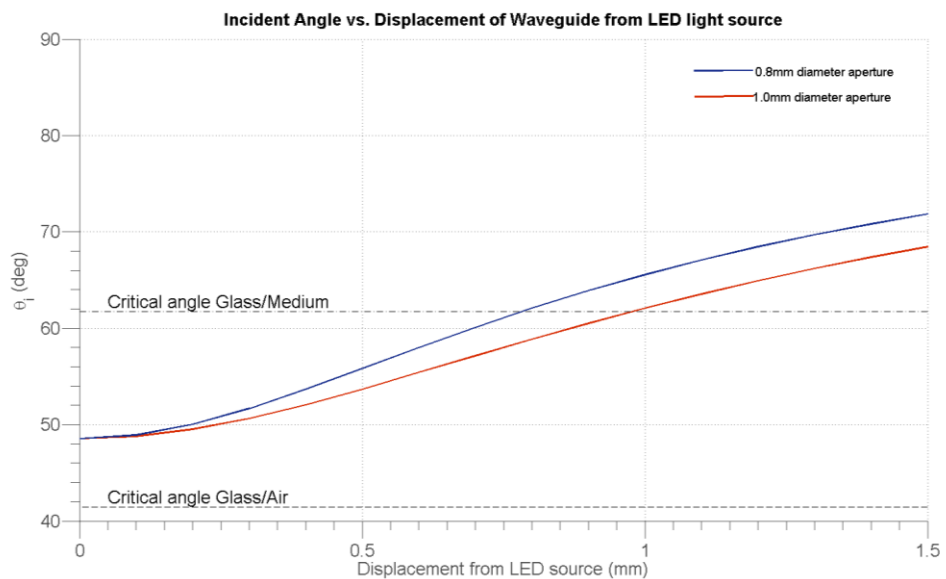


Figure 3.2 Effect of aperture size and displacement against angle of incidence

3.4.4 Detection system

A microscope system was setup on the bottom surface of the waveguide to detect the scattered signal from the tungsten tip. The detection system uses an objective lens with X8 magnification, 0.18 NA (Leica, UK). A tube lens ($f = 180\text{mm}$) is placed between the objective and a 1.45 megapixel monochrome 12-bit CCD camera (PL-B955, PixeLink, CA). A small magnification objective was chosen in order to achieve a larger field of view (0.8mm by 0.6mm), which eases the location of the probe tip on the image. In addition to this, a smaller magnification collects more photons over a smaller number of pixels on the detector, which in turn detects a higher signal from the tip. This implies that a shorter exposure time is possible compared to a larger magnification objective and can further minimise any drifting from the stage.

The lateral resolution based on Rayleigh's criterion(68) for such system is:

$$r = \frac{0.61\lambda}{NA} = \frac{0.61 \times 525\text{nm}}{0.18} \approx 1.8\mu\text{m}$$

Where,

r is the lateral resolution

NA is the numerical aperture of the objective lens

λ is the wavelength of the light source

Since the smallest resolvable object by the system was much larger than the probe, this meant the probe was not resolved on the images(43,68), but only the levels of intensity scattered at different separation distances were detected.

3.4.5 Image analysis

The effects of image analysis window size on the evanescent field depth are investigated and results are shown in Appendix V .A 3 by 3 pixel window within the image containing the probe tip was identified based on the high contrast of grey value compared to the dark background. Each datum points was normalised by dividing by its maximum value within the data set. This is because the shape of the curve intensity is more important than the actual intensity value and as shown in Figure 2.3, the transmittance is different for different angles of incidence. Normalisation was required to make the data sets

comparable and it was assumed that the maximum value is the intensity at the surface. The normalised mean of the 3 by 3 window was plotted against the tip displacement from the surface interface. It was not possible to fit the normalised data sets with an exponential function (Eq. 3.1) without removing the intensity offset. In this case, a double exponential was fitted as shown in Eq. 3.2. Subsequently, the intensity offset was removed and was fitted with an exponential function (Eq. 3.1) to determine the evanescent field depth at $1/e^2$ of intensity decay.

$$I(z) = e^{-Bz}$$

Eq. 3.1

$$I(z) = \frac{Ae^{-Bz} + Ce^{-Dz}}{A + C}$$

Eq. 3.2

Where,

$I(z)$ is the intensity value as a function of z

z is the tip displacement

A, B, C, D are fitting parameters to be determined

3.5 Results

The calculated evanescent field depths for both glass/air and glass/water interfaces are displayed in Figure 3.3. For both interfaces, as the incident angle increases from the critical angle, the evanescent field depth rapidly decreases. The measured angular range of the 0.8mm aperture was from 72.8° to 90° , which corresponds to a maximum field depth of 80nm between glass/air interface and 199nm between glass/water interface. For the 1mm aperture, the angular range was between 49° and 90° , which implies a maximum field depth of 143nm between glass/air interface and a deeper evanescent field depth was expected for glass/water interface because some incident angle will be closer to the critical angle.

Evanescent field depths could not be determined because according to its definition, it is the distance for the maximum intensity at the interface to decay

to $1/e^2$ (~13%). All results shown in Figure 3.4 displayed a slow decaying offset intensity that was observable at large displacements from the interface and the $1/e^2$ level was never reached within the $1\mu\text{m}$ range of measurement. The smallest offset was found to be 18% of the maximum intensity for 1mm aperture between glass/air interface and the largest was 55% when 0.8mm aperture was used between glass/water interface. For both apertures, the offset appeared to be higher between the glass/water interface than glass/air interface. Error bars of the glass/water results for both types of aperture were overlapping, which suggests there is no significant difference between the results. Furthermore, the results showed that using a 0.8mm aperture resulted in a higher offset than using a 1mm aperture.

The critical angle for glass/air interface was 41.5° and is lower than the critical angle for glass/water interface at 61.7° . The evanescent field depth is shorter for glass/air interface than between glass/water interface for the same incident angle. Shorter evanescent field depth also implies faster decay from the maximum intensity. The measured evanescent field profile displayed in Figure 3.4 indicates faster decays for glass/air interface than glass/water interface for both types of aperture.

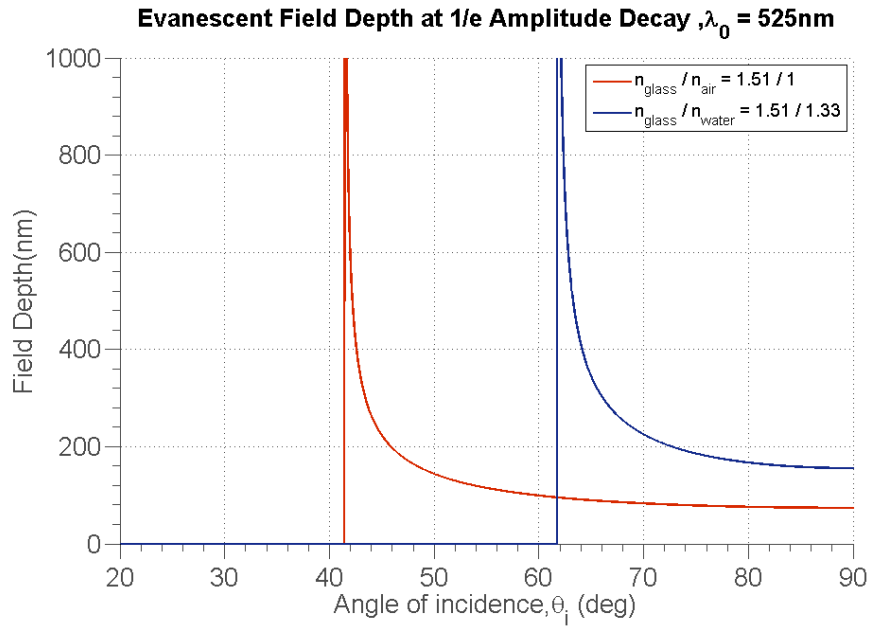


Figure 3.3 Evanescent field depth defined by 1/e amplitude decay plotted against angle of incidence for glass/air interface (red line) and glass/water interface (blue line).

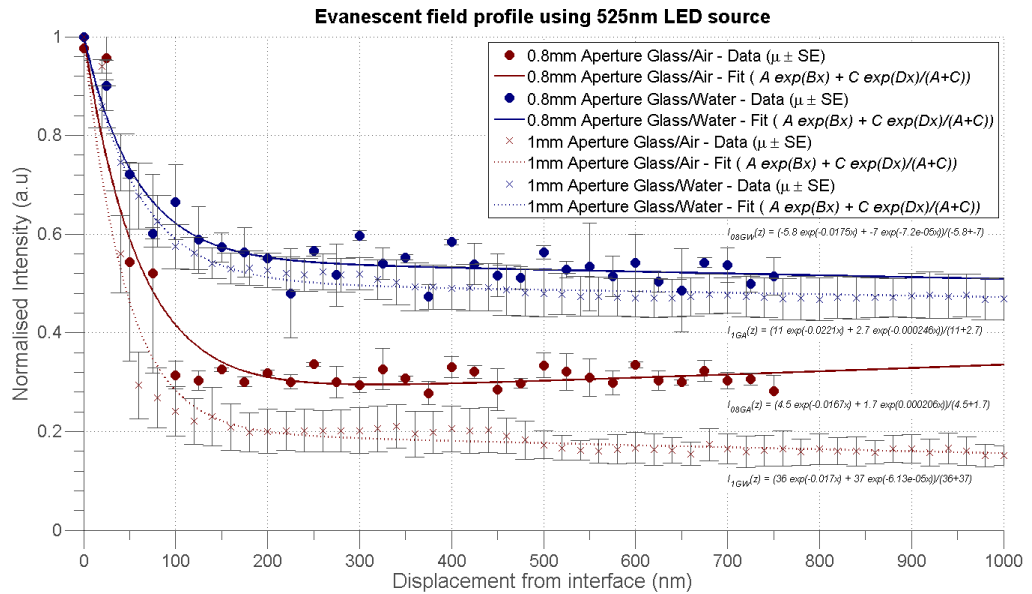


Figure 3.4 Measured evanescent field profile using 0.8mm aperture (circular markers) and 1mm aperture (cross markers) under glass/air interface (red) and glass/water interface (blue). Average data was fitted with double exponential function $\frac{Ae^{-Bz} + Ce^{-Dz}}{A+C}$.

The data was refitted with a single exponential function and double exponential functions after offset subtraction and the single exponential fit is displayed in Figure 3.5. The R^2 values of the both single exponential and double exponential fit were higher when a 1mm aperture was used than a 0.8mm aperture; these are displayed in Table 3.1. The distance at $1/e^2$ intensity decay was derived for the respective functions used to fit the data and are displayed in Table 3.2.

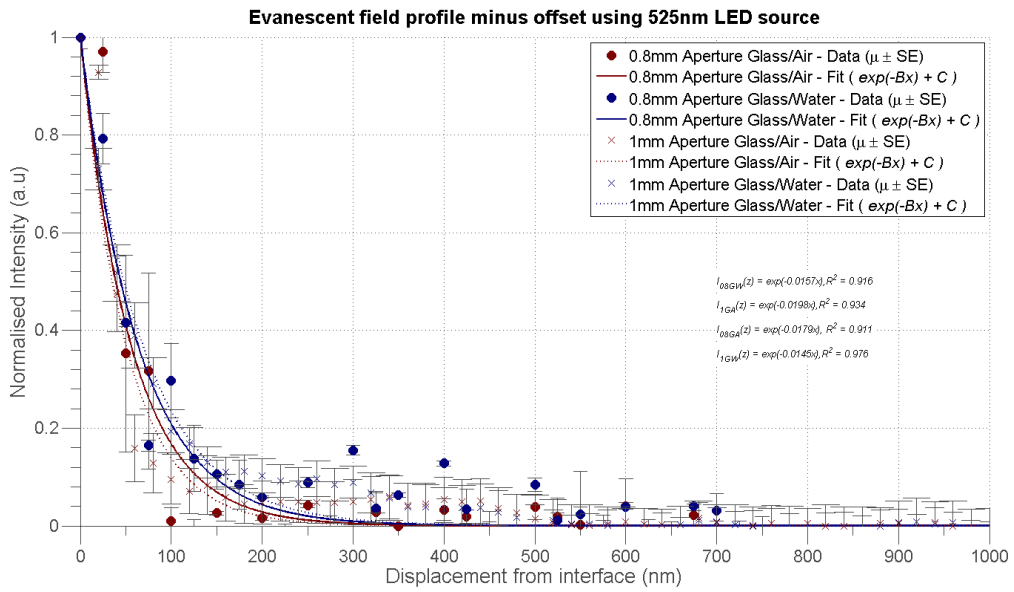


Figure 3.5 Measured evanescent field profile after offset removal by subtracting the average of the last 10 data points.

	R^2 value	
	e^{-Bz}	$Ae^{-Bz} + Ce^{-Dz}$
0.8mm Glass/Air	0.911	0.911
0.8mm Glass/Water	0.916	0.919
1.0mm Glass/Air	0.934	0.934
1.0mm Glass/Water	0.976	0.994

Table 3.1 R^2 values for single and double exponential functions used to fit the data.

	Distance at $1/e^2$ intensity decay (nm)		
	Designed value	e^{-Bz}	$Ae^{-Bz} + Ce^{-Dz}$
0.8mm Glass/Air	80	112 ± 39	112 ± 39
0.8mm Glass/Water	199	127 ± 46	130 ± 49
1.0mm Glass/Air	143	101 ± 88	101 ± 36
1.0mm Glass/Water	Close to crit.	138 ± 36	155 ± 5

Table 3.2 The distance at $1/e^2$ intensity decay for single and double exponential fit.

3.6 Discussion

Comparing the results from using a 0.8mm aperture to a 1.0mm aperture, the intensity profiles decayed slower when a 0.8mm aperture was used in comparison to a 1.0mm aperture, which suggests that the evanescent field depth was deeper when a 0.8mm was used. Larger evanescent field depths are normally achieved by lowering the incident angle so it is closer to the critical angle. The purpose of using a smaller aperture was to restrict the angular range of the LEDs so that the incident angle should be much larger than the critical. However, the results shown are contrary to the designed values.

Furthermore, high intensity offsets were observed in glass/water interface data sets at large displacements away from the interface. The offsets were slow decaying and almost constant, which suggests illumination in addition to the evanescent field was present. The experiment was carried out in a dark room and the equipment was placed inside blackout material, which implies the source was not from ambient light within the room. Moreover, the edge of the waveguide was found to be uneven and the pattern was different between waveguides. In contrast to the model used for the design, the edge of the waveguide is not flat and a ray of light that strikes the edge of the waveguide will refract differently to the designed value and will refract according to the surface of the edge. The result of this suggests that it is possible that some light was refracted from the edge so that the incident angle is below the critical angle resulting in propagating light in the second medium. A demonstration of the edge of the waveguide can be found in Appendix III .

It is common to assume that propagating light will refract out of the water layer after the first encounter and indeed, depending on the refracted angle, some light will refract out of the water layer. However, at a certain range of incident angle, this light will undergo total internal reflection at the water/air interface and refract back into the slide, which will again undergo total internal reflection when it reaches the glass/air interface. A more detailed examination is presented in Appendix IV . This suggests the high intensity offset could be a result of propagating light originating from the same LED source, but refracted below the critical angle of the glass/water interface.

In another LED illuminated waveguide study(55), an offset was not reported, but the displacement-intensity profile was found to best fitted with a double exponential profile; it consists of a fast decaying component and a slow decaying component. The intensity of the slow decay was around 34% at zero displacement from the surface, which was three times higher than the value reported in the objective-based system by Mattheyses and Axelrod(64). The differences between the two systems are the approaches to achieve total internal reflection, with the waveguide approach(55) and an objective-based approach(64), and the illumination sources, with one study using incoherent LED source(55) and the other using a coherent laser source(64). The difference in intensity offset could be explained by the fact that the use of a coherent laser source can provide a better control of the incident angle than using an incoherent LED source.

Although high intensity was detected at large distances from the interface in the study that used LEDs(55), the images captured using this method compared to epi-fluorescent had less hazy signals within the cell cytoplasm and focal adhesion points; these are areas where the base of the cell form close contacts with the surface, were more obvious. The result of this suggests that the presence of an offset in the evanescent field profile may still provide more illumination of the objects proximal to the surface than objects that are outside the evanescent field.

3.7 Conclusion

The results have shown an increasing intensity profile as an object approaches the interface. However, for all experimental conditions, an offset was present at large separation distance from the interface. This implies that a signal will be detected even if an object was present outside the evanescent field depth. Based on the results shown, an exponential increase in the intensity will be detected when the object moves within the first 200nm from the interface. However, if the object was a biological cell, the change in intensity may be caused by changes within the cell itself. The detection of intensity increase from the high baseline intensity may imply cell adhesion. If the cell is only detected within the evanescent field, then the signal can only be explained by

the evanescent field itself. Hence, the presence of the offset makes the detection of cell adhesion less effective.

The source of the offset was explained by the uneven edges of the waveguide that can refract light below the critical angle. This leads us to the next part of the study that uses optically polished waveguides and a collimated laser source to reduce the angle of incidence to a single angle.

Chapter 4 Characterisation of evanescent field profile using laser illumination source

4.1 Introduction

The purpose of illuminating an object with evanescent field in this system is to be able to distinguish the proximity of the object to the substrate. Depending on the incidence angle, the evanescent field can be confined within hundreds of nanometres from the interface. An object within the depth of the evanescent field will scatter light in all directions. The amount of light scattered by the object depends on the separation distance from the interface which follows an exponential profile.

In the previous section, an array of LEDs was used as the illumination source and was placed next to the edge of the waveguide to couple light into it. The evanescent field profile was characterised using a tungsten tip placed at various displacements from the boundary to scatter the evanescent field. The results displayed an exponential decay profile with a 50% offset of the full intensity at the glass/water interface. This implies the object could still be detected beyond the evanescent field, which makes the system less effective even though an exponential increase in intensity is expected as it enters the evanescent field. The source of the offset was likely to be caused by light striking the interface below the critical angle, which results in refracted light that propagates through the second medium and illuminates objects beyond the evanescent field.

One strategy to eliminate the offset would be to control the illumination angle so that all angles are beyond the critical angle. Using a coherent laser source allows accurate control of the incidence angle due to its narrow spectrum of wavelengths and low divergent beam, which will produce more defined evanescent fields and reduce refraction at the interface to an insignificant amount.

The following study aims to eliminate the offset at large separation distances by using a coherent laser light source. In addition to this, the edges of the

waveguide were polished to remove uneven surface. The combination of both changes has contributed in the improvement of reducing the intensity offset. The intensity offset was attributed to light striking the interface at a range of angles, which includes angles below the critical angle of the two media. The use of a coherent laser light source has helped to control the angle of incidence because of its low divergence property and the polished edges of the waveguide was essential for launching light at the desired angle of incidence.

Using the same method as the previous section, the evanescent field profile was characterised by detecting the scattered light from the tungsten probe which was placed at various separation distances away from the interface. This experimental procedure was performed on two types of waveguides with polished edges, unmodified waveguides and waveguides with a black rubber O-ring that was adhered to the surface using black silicone gasket. The purpose of adding the gasket was to investigate its effect on the evanescent field, which will be useful in future cell experiments where the gasket can act as a barrier to contain aqueous solution of the cell culture medium.

4.2 Materials and Methods

4.2.1 Waveguide

Glass microscope slides ($n=1.51$, 73mm by 23mm by 1mm thickness, Mönzel-Glasser, Thermo Scientific, UK) with the 1mm edges polished to an optical finish was used as the waveguide. Two conditions of the waveguide were tested; one was an unmodified waveguide and the other type had a black rubber O-ring attached onto the top surface of an unmodified waveguide using high modulus black silicone sealant (BOND~FLEX, Bostik, UK). In both types of waveguides, a 200 μ l drop of distilled water was placed on the top surface and inside the O-ring. The evanescent field depth was probed on the glass/water interface in the two conditions of liquid confinement. Two types of waveguide are shown in Figure 4.1.

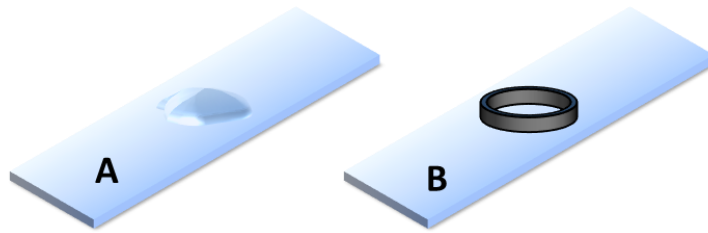


Figure 4.1 Schematic diagram of unmodified waveguide with water droplet (A) and waveguide with black rubber O-ring adhered using black silicone(B); water droplet was placed inside the O-ring.

4.2.2 Laser illumination setup

To control the angle of incidence, a 635nm 1mW collimated laser diode module (CPS180, Thorlabs, UK), with a beam diameter of 3.9mm was mounted onto a manual rotation stage. The divergence of the laser source is less than 0.3mrad. The laser diode itself is more than 90% linearly polarised and the diode was rotated such that the beam incident to the surface of the waveguide was mostly s-polarised. The edge of the waveguide was placed at the centre of the rotation stage and the beam was aligned such that upon rotation of the laser source, the beam will always strike the edge of the waveguide. As the waveguide itself was 1mm thick and the beam diameter was 3.9mm, a 0.4mm slit aperture was placed directly in front of the coupling edge of the waveguide to prevent light from scattering at the corners of the glass

slide. The whole waveguide illumination and sample holder was mounted onto two manual uniaxial stages in the x-direction for changing the area of sample being imaged and in the z direction to position the top surface of the sample on the focal plane of the objective. Figure 4.2 shows a schematic of the setup.

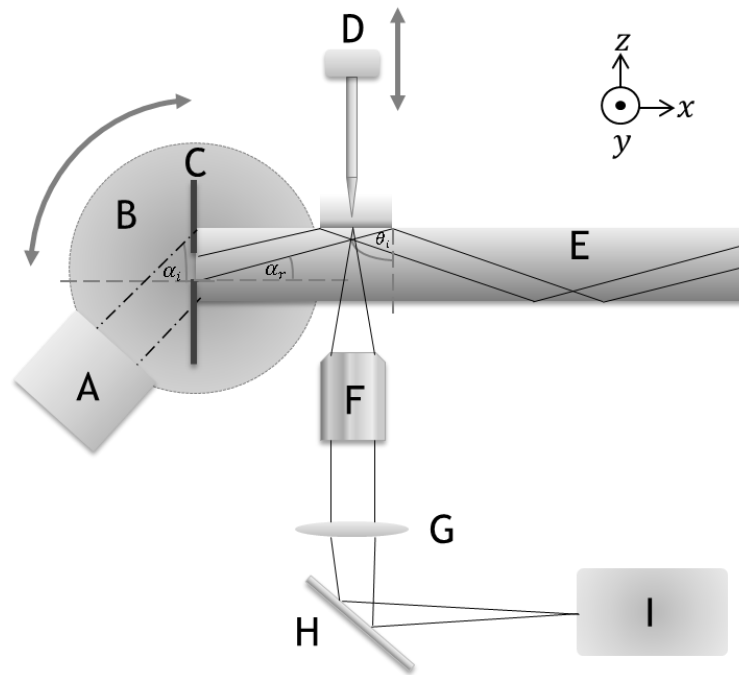


Figure 4.2 Schematic of system setup. A – 635nm Laser diode. B – Rotation stage. C – 0.4mm slit aperture. D – 0.5 μ m tip tungsten probe on piezo-electric stage. E – Glass Waveguide. F – X8 NA 0.18 objective lens. G – Tube Lens $f = 180$ mm. H – Mirror. I – 12-bit monochrome CCD

4.2.3 Evanescent field characterisation

To determine whether total internal reflection was satisfied across the glass/liquid interface, the evanescent field was determined by taking magnified images of the scattered light by a fine tungsten tip moving in the z-direction away from the glass/water interface.

The evanescent field depth was probed using a 0.5 μ m radius of curvature tungsten tip (Model 7B, Micromanipulator, NV, US) mounted onto a closed loop feedback piezoelectric stage (20nm resolution, TSG001 & TPZ001,

ThorLabs, UK) perpendicular to the waveguide surface. A tip size smaller than the illumination wavelength was chosen so that it acts as a single point scattering object. The image was first focused on the surface of the slide using small contaminants that were not removed during the cleaning process. The piezoelectric stage was equipped with a 5mm manual travel distance and the tip of the probe was manually positioned to the surface until it appeared on the image. The camera exposure was adjusted such that when the tip is on the surface of the interface, the image of the tip is below pixel saturation. Typical exposure time was 1 second and varied to 2.5 seconds depending on the angle of incidence. Higher exposure times were required when the angle of incidence was well above the critical angle. An image was taken at every 20nm step displaced away from the surface.

4.2.4 Image analysis

Image analysis was performed as described in section 3.4.5 . Figure 4.3 shows an example of the image analysis.

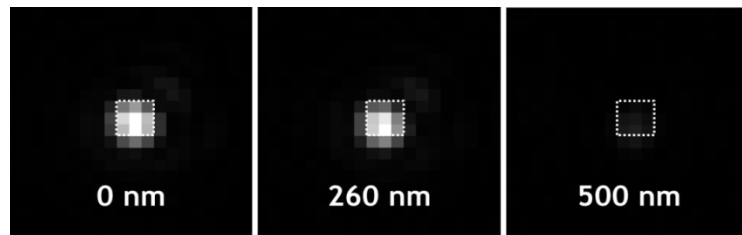


Figure 4.3 An example showing the area marked for image analysis. Cropped images of the probe tip with 3 by 3 pixel analysis window marked within the white dotted boxes at different displaced distance from the surface. The mean intensity within the analysis window was calculated and these were plotted against the displacement distance from the interface. Data set from incident angle, $\theta_i = 68.1^\circ$.

Three types of functions were fitted to the data and these were single exponential function written as Eq. 4.1, double exponential displayed as Eq. 4.2 and also, the three layer transmittance model(48) as described in section 2.2 and displayed as Eq. 4.3(48).

$$I(z) = e^{-\beta z}$$

Eq. 4.1

$$I(z) = \left(\frac{Ae^{-Bz} + Ce^{-Dz}}{A + C} \right)$$

Eq. 4.2

$$I(z) = \left(\frac{C}{A \sinh^2 Bz + C} \right)$$

Eq. 4.3

The evanescent field depth was calculated based on the definition of its amplitude decay to a factor of e^{-1} . Since, the intensity is proportional to the square of the amplitude of the electric field(43), the evanescent field depth can be calculated as the intensity decay of e^{-2} . The evanescent field depth, z , based on intensity value would become Eq.4.4 and in essence, the evanescent field depth calculated using intensity is half of the depth calculated based on the amplitude:

$$I(z) = I_0 e^{-2\beta z}$$

Eq. 4.4

I_0 is the intensity at zero displacement from the interface and $I(z)$ is the intensity at a particular displacement from the surface, z . For the other two types of fits, the evanescent field depth was calculated as the separation distance for the intensity to reduce from its maximum to its $\frac{1}{e^2}$ value. The goodness of fit was assessed using the R^2 value.

The effect of window size used in the analysis on the evanescent field depth was investigated and the change in evanescent field depth was between - 9.8% and 9% for silicone waveguides and unmodified waveguides respectively. The

window size used in the analysis ranged from 1 by 1 pixel up to 21 by 21 pixels. Further details can be found in Appendix V .

4.3 Results

The images in Figure 4.4 showed the illumination within the field of view was shifted when the incidence angle was changed slightly. This suggests total internal reflection was achieved because only a discrete number of locations on the waveguide are illuminated when laser was used as the source of illumination. In addition, the illumination shift shows the angle of incidence can be changed as desired. The number of locations for total internal reflection to occur depends on the incidence angle. Figure 4.5 aims to explain the shift of the total internal reflection location across the waveguide. Starting from the left hand side, two rays with the same beam diameter and different incidence angles above the critical angle ($\theta_i = 62^\circ$ (solid line), $\theta_i = 80^\circ$ (dashed line)) were traced inside the waveguide. In Figure 4.5, the number of total internal reflections for $\theta_i = 62^\circ$ were 12 within the length of the waveguide and 4 total internal reflections were observed for $\theta_i = 80^\circ$. The locations of total internal reflection also occurred at different points along the waveguide due to the different incidence angles. Focusing on the first total internal reflection from the left, as θ_i is increased from 62° to 80° , the location of total internal reflection is shifted towards along the waveguide, which is similar to the results shown in Figure 4.4.

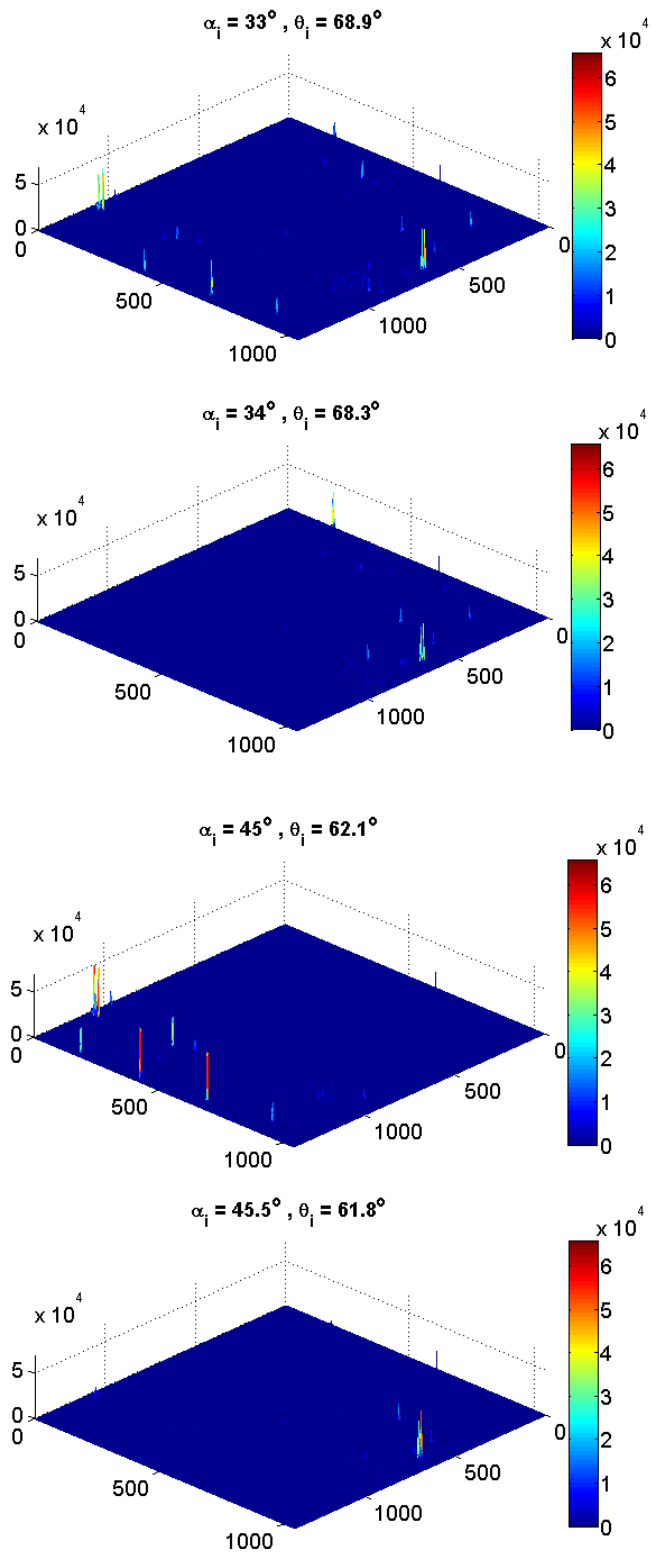


Figure 4.4 Images showing how changing the angle of incidence slightly can shift the illumination across the image. All four images were taken at the same location on an unmodified waveguide

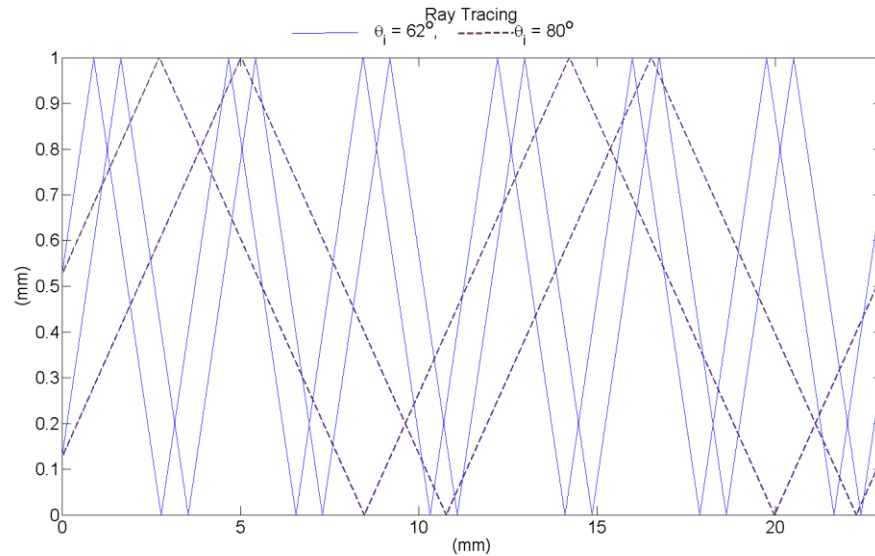


Figure 4.5 Ray tracing inside the waveguide using two incidence angles with the same beam diameter. Solid line - $\theta_i = 62^\circ$, Dashed line - $\theta_i = 80^\circ$. An increase in incidence angle results in less regions along the waveguide being illuminated, but area of illumination is also larger than lower incidence angles which suggests the power is distributed over a larger area and so the scattered signal is expected to be less at higher incident angles

The theoretical values of the evanescent field calculated for a range of incidence angles are presented as the blue line in Figure 4.6. The plot shows the evanescent field depth tends to infinity at the critical angle, $\theta_{crit.} = 61.7^\circ$ and the evanescent field depth decays rapidly as the incidence angle is increased. The same trend was observed when silicone gasket waveguides were used, however, for unmodified waveguides, the average evanescent field depth at $\theta_i = 68.1^\circ$ was found to be 25.6% smaller than the depth at $\theta_i = 77.4^\circ$. Whereas the evanescent field depth of the theoretical value for $\theta_i = 68.1^\circ$ was 43.9% larger than $\theta_i = 77.4^\circ$. Also, the theoretical evanescent field depth for $\theta_i = 62.1^\circ$ was larger than $\theta_i = 68.1^\circ$ by a factor of three, however, the measured values were higher by a factor of 1.34 and 0.93 for unmodified waveguides and silicone gasket waveguides respectively.

The intensity profiles fitted with a simple exponential function for both types of waveguides are displayed in Figure 4.7. It can be seen that the simple exponential function does not fit properly for $\theta_i = 77.4^\circ$ using unmodified waveguides and $\theta_i = 68.1^\circ, 77.4^\circ$ using silicone gasket waveguides. For the

data set where the angle of incidence was near the critical angle on silicone gasket waveguides, it displayed a slow exponential decaying profile.

A summary of the measured evanescent field depth based on the definition of intensity decay to $1/e^2$ on unmodified glass waveguide and glass waveguide with black silicone gasket are shown in Table 4.1. The evanescent field depth at $\theta_i = 77.4^\circ$ was higher when measured using the unmodified waveguides than silicone gasket waveguides. The difference was 35.6% with simple exponential fit, 68.0% for double exponential fit and 41.2% when fitted with the three layer transmittance model. On the contrary, the evanescent field depth at $\theta_i = 68.1^\circ, 62.1^\circ$ were both lower using unmodified waveguides than silicone waveguides. The differences were -58.8% and -31.0% for simple exponential fit, -59.0% and -24.5% for double exponential fit and -38.1% and -19.2% with the three layer transmittance model.

Fitting the data with a double exponential resulted in the average increase of evanescent field by 2.26% for unmodified waveguides and an average decrease of -16.4% for silicone gasket waveguides. Conversely, fitting the data with the three layer model resulted in an average decrease of -13.4% for unmodified waveguides and -22.3% for silicone gasket waveguides.

		Mean ± Standard Error (nm)					
	Theoretical value (nm)	Unmodified Waveguide			Silicone Gasket Waveguide		
		$e^{-\beta z}$	$\frac{Ae^{-Bz} + Ce^{-Dz}}{A + C}$	$\frac{C}{Asinh^2Bz + C}$	$e^{-\beta z}$	$\frac{Ae^{-Bz} + Ce^{-Dz}}{A + C}$	$\frac{C}{Asinh^2Bz + C}$
77.4°	212	418 ± 17	422 ± 11	359 ± 20	269 ± 53	135 ± 27	211 ± 32
68.1°	305	311 ± 4	312 ± 6	265 ± 5	494 ± 27	469 ± 27	366 ± 0.5
62.1°	1229	728 ± 6	768 ± 7	646 ± 6	954 ± 55	956 ± 55	770 ± 15
$\theta_{near\ crit.}$	-	-	-	-	3250 ± 318	2858 ± 212	2101 ± 271

Table 4.1 Comparison of evanescent field depth between theoretical and experimental values on unmodified waveguide and black silicone gasket waveguide. The theoretical value was from a simple exponential decay for different angles of incidence. The experimental values of the evanescent field depth was based on the reduction of the intensity to $1/e^2$ for both simple exponential fit ($e^{-\beta z}$), normalised double exponential ($\frac{Ae^{-Bz} + Ce^{-Dz}}{A + C}$) and normalised three layer model fit ($\frac{C}{Asinh^2Bz + C}$). Data for unmodified waveguide at $\theta_{near\ crit.}$ was not collected.

		R ² value					
	$e^{-\beta z}$	Unmodified Waveguide			Silicone Gasket Waveguide		
		$\frac{Ae^{-Bz} + Ce^{-Dz}}{A + C}$	$\frac{C}{Asinh^2Bz + C}$	$e^{-\beta z}$	$\frac{Ae^{-Bz} + Ce^{-Dz}}{A + C}$	$\frac{C}{Asinh^2Bz + C}$	
77.4°	0.9481	0.9543	0.9597	0.9613	0.9629	0.9941	
68.1°	0.9186	0.9419	0.8824	0.9194	0.9194	0.9992	
62.1°	0.9800	0.9873	0.9275	0.9921	0.9921	0.9799	
$\theta_{near\ crit.}$	-	-	-	0.9800	0.9825	0.8693	

Table 4.2 Goodness of fit based on R² value for three types of normalised functions: simple exponential ($e^{-\beta z}$), double exponential ($\frac{Ae^{-Bz} + Ce^{-Dz}}{A + C}$) and three layer model ($\frac{C}{Asinh^2Bz + C}$). Values are highlighted showing the highest R2 value out of the three types of fit.

The goodness of fit based on the R² value is shown in Table 4.2. Experimental data for the silicone gasket waveguide fitted with a single exponential function resulted R² values of 0.9926 and 0.9811 for incident angles of 62.1° and angles close to the critical angle respectively. While fitting the data with the three layer transmittance model for the same angles of incidence corresponded to R² values of 0.9799 and 0.8693. Similarly, for unmodified waveguides, the R² values for single exponential fit were 0.9214 and 0.9882 for $\theta_i = 68.1^\circ$ and $\theta_i = 62.1^\circ$, while fitting with the three layer model resulted with R² values of 0.8824 and 0.9275 respectively. At $\theta_i = 62.1^\circ$, both single and double

exponential functions had the same R^2 value of 0.9921 and was higher than the three layer transmittance model of 0.9799.

The data which had best fitted with the three layer transmittance model function were re-plotted on a log scale to show the deviation from the simple exponential function. Figure 4.8 shows the deviation from exponential fit on a log scale. The measured evanescent field profile is not a simple exponential for $\theta_i = 77.4^\circ$ when a unmodified slide was used and the deviation is apparent between $z = 0$ and 200nm. In the case where a silicone gasket was attached to the waveguide, for $\theta_i = 77.4^\circ, 68.1^\circ$ the deviation is observed between $z = 0$ to 80nm and $z = 0$ to 200nm respectively. In comparison to the transmittance curve generated by varying the distance of on a three layer model, where $n_1 > n_2 < n_3$ (14), the transmittance curve also deviates from the exponential function from $z = 0$ to 250nm and $z = 0$ to 200nm for $\theta_i = 77.4^\circ, 68.1^\circ$ respectively.

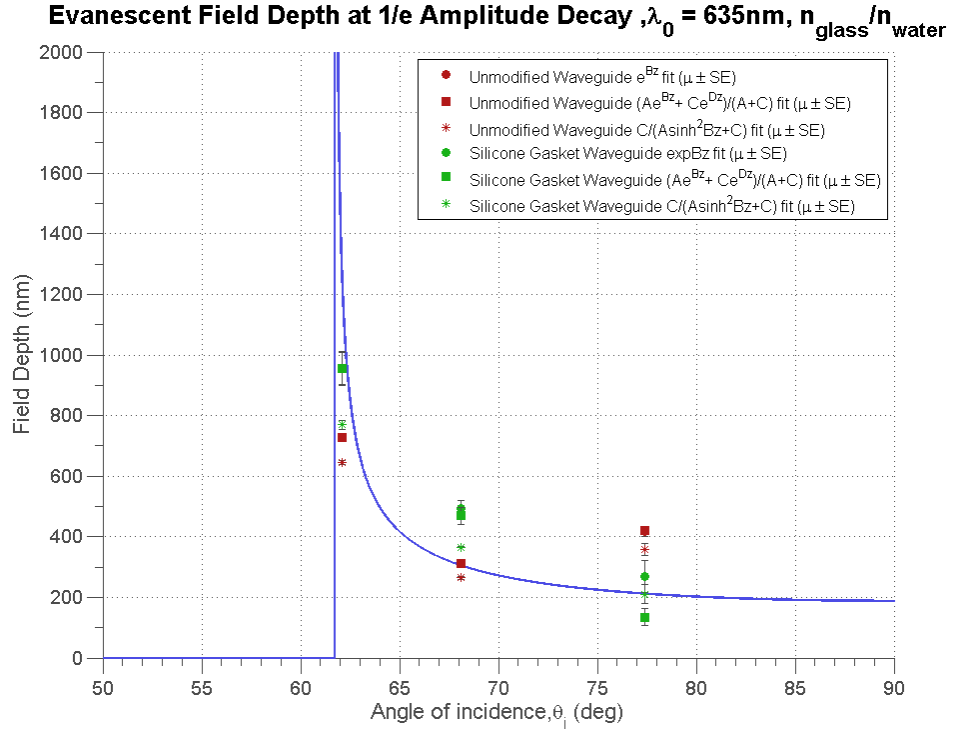
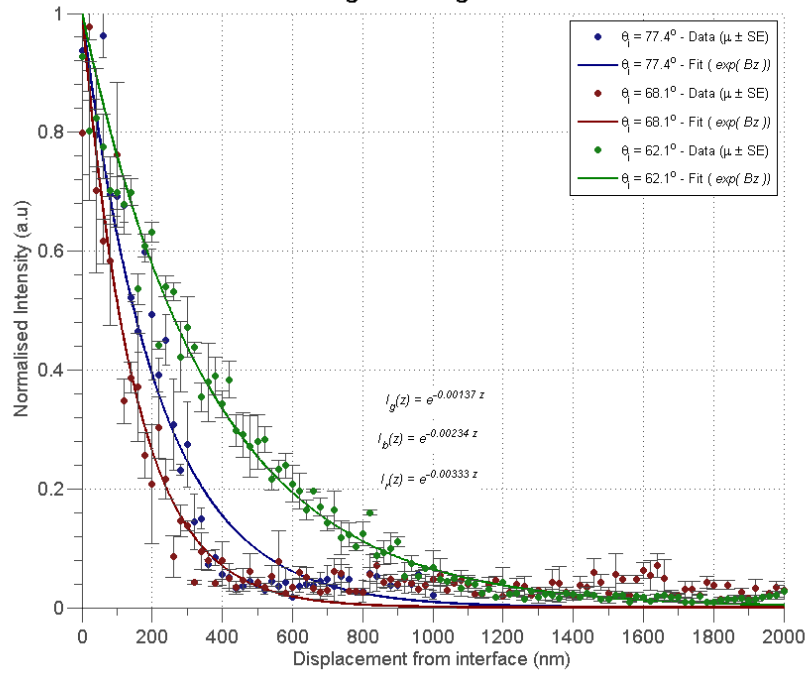


Figure 4.6 Comparison of evanescent field depth at a range of angle of incidence. Blue line represents the theoretical values calculated by $\beta = \frac{1}{k_0 \sqrt{(n_{\text{glass}}^2 \sin^2 \theta_i - n_{\text{water}}^2)}}$, $k_0 = \frac{2\pi}{\lambda}$. Green and red markers are experimental values of evanescent field depth based on $1/e^2$ intensity decay using unmodified waveguides and silicone gasket waveguides respectively. Circle markers are evanescent field depth values based on simple exponential fit ($e^{-\beta z}$), square markers are value derived from double exponential fit ($\frac{Ae^{-Bz} + Ce^{-Dz}}{A+C}$) and star markers are field depths based on the three layer model ($\frac{C}{A \sinh^2 Bx + C}$).

A

Evanescent field depth at Glass/Water Interface on unmodified Waveguide using 635nm LASER source

**B**

Evanescent field depth at Glass/Water Interface Confined within Black Rubber & Silicone Gasket using 635nm LASER

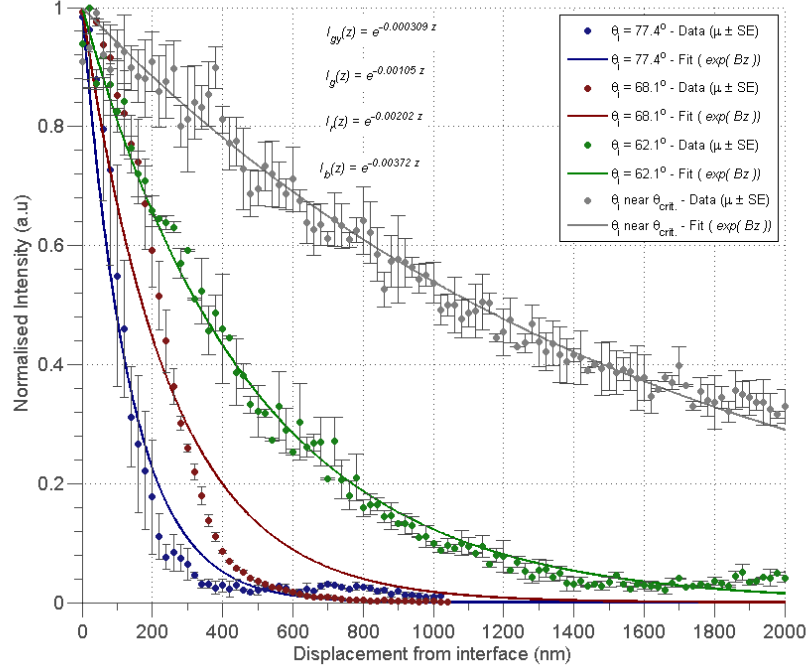


Figure 4.7 Intensity profile of a tungsten tip with increasing displacement from glass/water interface on unmodified waveguides(A) and silicone gasket waveguide(B). All data were fitted with a simple exponential function $e^{-\beta z}$.

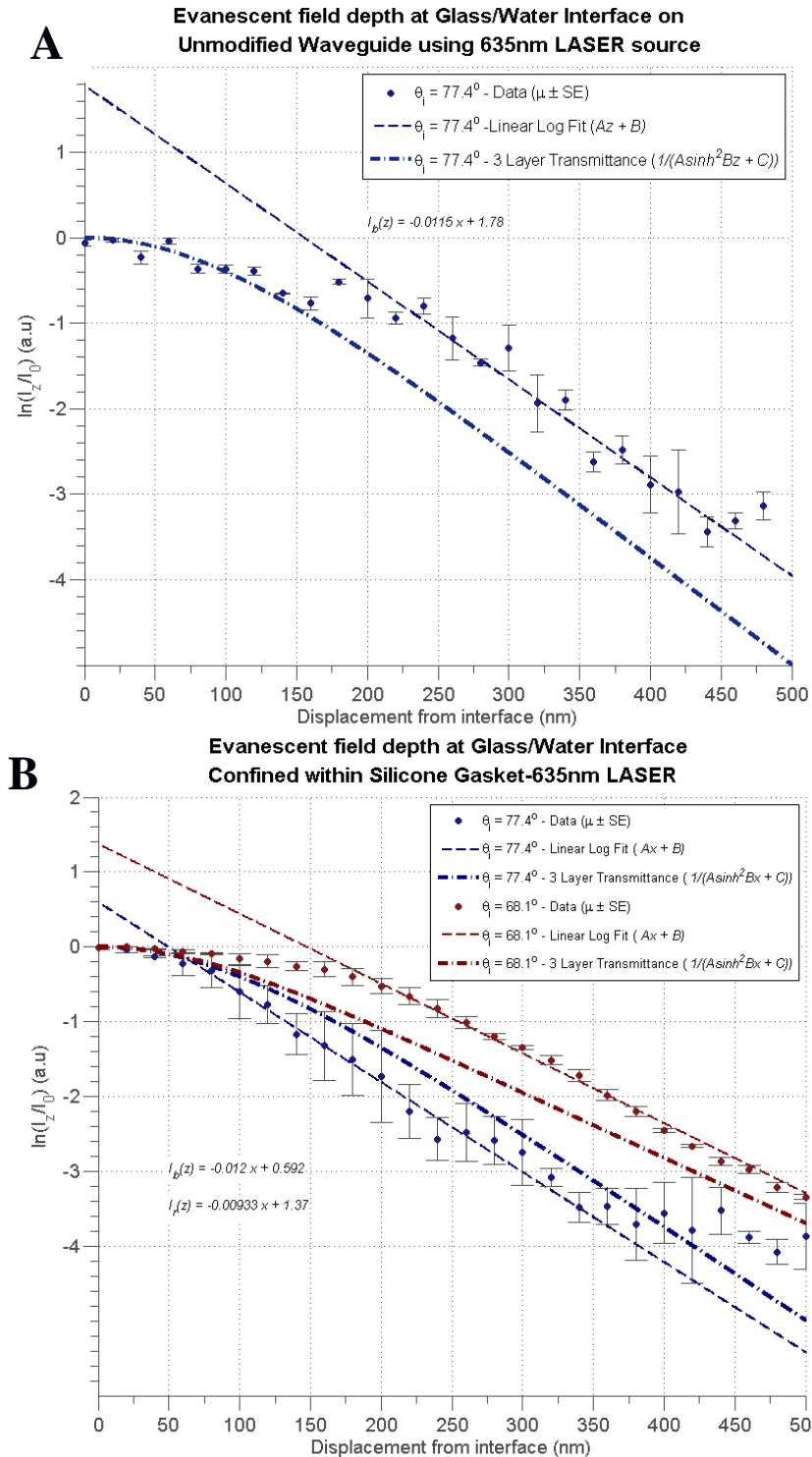


Figure 4.8 Intensity profile on a log scale against the displacement from glass/water interface to show the deviation from a simple exponential function on unmodified waveguides (A) and silicone gasket waveguides (B). Only data sets that did not fit well to an exponential function were plotted.

4.4 Discussion

The measured value of the evanescent field differed largely in comparison to the theoretical value. The difference ranged from -0.47% up to 99.0% depending on the function of fit, the results displayed a trend of decreased evanescent field depth as the incidence angle was increased which was consistent with theoretical calculations. There is one anomalous result when unmodified waveguides were used at $\theta_i = 77.4^\circ$, where the evanescent field depth was measured to be just under two times the theoretical value and higher than the evanescent field depth at $\theta_i = 68.1^\circ$.

About half of the data indicated a shorter evanescent field depth than the theoretical value and one explanation for this is because it is not possible to determine the exact position of the tip in relation to the surface of the interface without damaging the tip itself using the current setup. However, if an atomic force microscope system was used, then it can reference the position of the slide surface to the tip which means it will be possible to probe closer to the interface. Furthermore, a manual rotation stage was used to control the angle of incidence, so it is not possible to precisely determine the angle of incidence.

Although this method only measures the scattered evanescent field and is not a direct measurement of the evanescent field, the results suggest that the scattered intensity is a function of the separation distance from the interface and the angle of incidence. However, in terms of how much light is scattered between different samples, the result will depend on the sample itself. Biological samples are likely to possess variable scattering properties and therefore, the scattered field as a function of the separation distance from the interface should be quantified with the sample of interest.

Additionally, the signal detected well beyond the evanescent is not absolutely zero, but it is below 10% of the maximum signal which is low compared to the maximum signal at the interface. This is a reduction from 40% using LEDs sources to 10% using a coherent laser source. It is noted that at higher exposure times (~ 6 seconds), the tungsten probe tip can be seen even when it is well beyond the evanescent field depth, but if the tip was within the evanescent field, the image of the tip will become saturated after exposing the detector for the

same duration. For the purpose of detecting an object that is close to the interface, a threshold can be placed on the signal level so that a signal will only appear when an object is well within the evanescent field.

The fluctuating signal that was detected beyond the evanescent field is likely caused by several factors. Low signal is expected when the probe moves further away from the interface and such signal is likely to be shot noise limited and a noisy signal is expected. Another factor is the objects on the surface of the slide that was not removed during the cleaning process. These objects are likely to turn evanescent field into propagating light in all directions and in turn, scatters from the tungsten tip and contributes to the signal detected at large separations distances. The study by Hulst et al.(69) also reported an increase of radiative scattered field when the fibre optic probe was placed further away from the sample.

It is not possible to distinguish whether the angle is supra-critical or sub-critical. Since the evanescent field depth tends to infinity at the critical angle and the decay profile is much slower for angles of incidence closer to the critical angle, so it is possible to obtain such evanescent field depth. Conversely, if the angle of incidence was sub-critical, the beam would get refracted at the interface and the illumination is constant in the z-direction assuming the beam itself is uniform. The intensity profile for an angle of incidence well below the critical angle can be measured to verify this. However, this is not possible at the moment due to the limitation of mechanical components within the system.

It can be seen that the measured profile for the evanescent field is not a pure exponential especially for regions closest to the interface. Similar deviations were observed in other studies and the three layer transmittance model as described in section 2.2 . The deviation in the model was explained by interference between the reflected beam and the transmitted beam between layers. Based on theoretical calculations for a three layer model, the deviation increases for higher angles of incidence which are contrary to the results, however, a single exponential function was fitted better than the three layer model for angles closer to the critical angle. For angle of incidence at 68.1° , a simple exponential function was better fitted than the three layer model for

unmodified waveguides, whereas the opposite was true for the silicone gasket waveguides. For unmodified waveguides, the best fitted function was the three layer model for $\theta_i = 77.4^\circ$ and double exponential functions were best fitted for $\theta_i = 68.1^\circ$ and 62.1° . For silicone waveguides, the three layer transmittance model was best fitted at $\theta_i = 77.4^\circ$ while, the double exponential function was also best fitted for the incidence angle near the critical angle. This is possibly due to the positioning of the tip further away from the interface and hence, failed to capture this data.

The observation of non-exponential profile was also reported in other studies including Reddick et al.(70) and Tsai et al.(71), where a photon scanning tunnelling microscopy was used to measure the evanescent field profile. The illumination of the photon scanning tunnelling microscopy occurs beyond the critical angle so that total internal reflection is achieved. Subsequently, a chemically sharpened fibre optic was used to probe the evanescent field and by principles of frustrated total internal reflection, non-radiative evanescent field turns into propagating waves and was carried through the fibre optic onto photomultiplier tubes. The non-exponential profile of the evanescent field was reported to be an artefact of the tip shape/ sample surface and the same findings were shown when the same system was used to probe silicon oxynitride planar waveguides(71).

A similar system reported by Hulst et al. (69), also found the evanescent field to have non-exponential profile and the polarisation of illumination as well as the tip shape had affected the measurements. When the probe tip was scanned across a periodic grating in constant height mode under p-polarised illumination, the signal was more stable and was higher by 66% than s-polarised illumination. The authors suggested the use of p-polarisation to be used for vertical features and s-polarisation for features in the lateral direction. Modelling results by Labani et al.(72) also confirmed the same findings.

Prieve and Walz(73) modelled the multiple reflection effects between a polystyrene sphere using ray-optics scattering model and validated the results experimentally. The difference between the ray model and the transmittance model is that the sphere has a finite size and finite number of reflection,

whereas the transmittance model was derived by the sum to infinity. Also, a sphere scatters evanescent field in all direction, but only those rays that appear in the same direction will interfere and be detected in the farfield. They found little effects of multiple reflections for polystyrene sphere between $7\mu\text{m}$ and $30\mu\text{m}$. The effect is less apparent when the film is thick (i.e. separation distance between interface and scatterer is large) and the transmittance reduces to an exponential profile. Hence scattered intensity at large displacement follows the exponential model as illustrated in their simulation and experimental results.

Similarly, a simulation of the scattered evanescent field by micrometre sized spherical particles in suspension was reported by Helden et al.(74). The evanescent field was generated under prism-based TIRM configuration and the discrete source method was used. Deviations from simple exponential function was reported when the penetration depths are large and under s-polarised illumination.

The results shown in this chapter are attributed to two changes; polished edges of the waveguide and changing the light source from an LED to a collimated laser. Without polishing the edges of the waveguides, the refracted angle within the waveguide cannot be predicted and hence light can strike the glass/water interface below the critical angle, causing propagating light and in turn results in the large intensity offset as shown in chapter 3. Switching to a low divergence laser source from an LED source provides better control over the angle of incident and it can be certain that the angle of incident is beyond the critical angle. In turn, the evanescent field depth can be controlled, which was demonstrated in this chapter. In theory, the evanescent field could be generated using an LED light source in combination with a polished waveguide by adopting approaches in Appendix VIII.

Lastly, in this study, the black silicone as an adhesive on the surface of the waveguide resulted in more accurate evanescent field depths for $\theta_i = 77.4^\circ, 62.1^\circ$ than unmodified waveguide. The variation in the result may only be due to using a manual rotation stage and not a result of using the silicone as

an adhesive. This suggests that black silicone is a suitable material to attach physical barriers to contain cell culture medium for future experiments.

4.5 Conclusion

In conclusion, the combination of using a polished waveguide and a collimated laser source instead of large angle LEDs have reduced the intensity offset by a factor of 4. The depth of the evanescent field can be controlled by changing the incident angle and although the evanescent field characterised using this method did not conform to a simple exponential function as reported in the literature, the scattered intensity was a function of the separation distance from the interface and the potential of using a waveguide system to detect the adhesion of biological materials has been demonstrated.

Chapter 5 Tracking microsphere solution in bright-field and waveguide mode

5.1 Introduction

The principle of evanescent field illumination is to illuminate only a thin section proximate to the interface, which can potentially be used to determine the distance between an object and the interface, as well as the level of adhesion of biological materials.

In the previous section, the evanescent field was characterised using a fine tungsten probe to scatter the evanescent field at various displacements away from the interface. Although the result of the evanescent field profile appeared sigmoidal rather than a simple exponential, some form of rapid decay was present in the profile, suggesting the presence of the evanescent field. In parts of the data, a small intensity response was measured at large displacements from the interface, which implies the presence of propagating light other than the illumination from evanescent field. Furthermore, the result obtained using LEDs, which emit light with a large range of angles, including angles below the critical angle, has demonstrated similar effects. One feasible explanation for this is the presence of propagating light generated by parts of the illuminating light under the critical angle.

This study aims to demonstrate that light detected on the waveguide channel is mainly due to evanescent field illumination and there is potential for depth discrimination.

To demonstrate this, microspheres in solution were imaged consecutively under laser waveguide illumination and bright-field illumination. Microspheres were tracked through the image sequence and the response on the bright-field channel was compared to that on the waveguide channel.

5.2 Materials and Methods

5.2.1 Experimental procedure

The experimental setup was as described in section 4.2.2 . A glass microscope slide waveguide with polished edges was used as a waveguide and black silicone gasket was used to hold 200 μ l of distilled water. The time-lapse image capture was initiated before the addition of microspheres. Dry $\text{\O}1.4\mu\text{m}$ polystyrene microspheres were added to the water by inserting the tip of a pipette that has been in contact with the dry microspheres into the distilled water. To avoid distorting the surface of the waveguide, the tip of the pipette was lowered into the distilled water without touching the waveguide surface. In one case, excess microspheres were added and clusters were formed. Image capture continued until the water within the gasket has completely evaporated.

5.2.2 Hardware control

To capture both bright-field and waveguide images in quick succession; the illuminations of both modes were toggled on and off so only one imaging mode is exposed at a time. The illumination sources used were a 1mW laser diode with a wavelength of 635nm for the waveguide illumination (CPS180, Thorlabs, UK) and a 4mW LED with a central wavelength of 635nm for the bright-field illumination (LED631E, Thorlabs, UK).

The sequence of hardware control was composed of a loop which was repeated for a specified number of times and the sequence within the loop was as follows: the laser source was kept on until the camera has finished capturing an image, then the laser source was toggled off, while the LED source was switched on to capture the bright-field image. After the bright-field image was captured, the loop was repeated until the specified number of loops has been reached. Figure 5.1 shows a flow diagram of the hardware control loop.

A relay switch was used to toggle between the waveguide illumination and bright-field illumination and the relay was driven by a USB data acquisition card (USB-1208FS, Measurement Computing, USA). The sequence of the image capture and illumination modulation was programmed in LabVIEW (National Instruments, UK). The exposure time was 500ms and 1ms for the waveguide mode and bright-field mode respectively and the gain was set to

zero in both modes. The difference in exposure time was because the scattered signal was lower in the waveguide mode and also, the LED illumination source was four times more powerful than the laser.

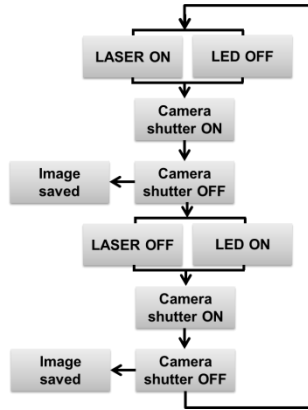


Figure 5.1 Flow diagram of hardware control loop

5.2.3 Image processing and single particle tracking

The microspheres were expected to appear within the depth of focus in bright-field images, whereas the microspheres will only be seen when it is within the evanescent field in the waveguide mode. To track microspheres based on this hypothesis, the microspheres within the bright-field mode were segmented and a threshold mask was created. The same mask was applied to the waveguide image to locate the position of the microspheres.

To segment the microspheres in the bright-field channel, the background was first removed by subtracting each frame from an initial image that was taken before the addition of particles. Since bright-field images have the characteristics of objects appearing dark over a bright background, by applying image subtraction, the resulting image turns into a darkfield image, where the object of interest is bright over a dark background. Next, the background was removed by adjusting the contrast of the image. The object itself also becomes smaller after contrast adjustment and subsequent steps of image dilation and image close was applied to adjust the size object. An example of the segmentation process is shown in Figure 5.2. All image processing was performed using a commercial software package (MATLAB, R2012a, The MathWorks Inc., Natick, MA, US).

Each segmented object was labelled and a tracking program called SimpleTracker (SimpleTracker, MATLAB Central, available on: <<http://www.mathworks.co.uk/matlabcentral/fileexchange/34040-simple-tracker>> [01/09/2014]) was used to track objects between frames based on the shortest distance travelled. The program is capable of tracking multiple objects, but images were cropped to track only one particle because different microspheres move at different velocities across the image, this required different tracking parameters. Tracking objects in cropped images resulted in better tracked paths and hence, the images were cropped such that the path of the microsphere fits inside the image.

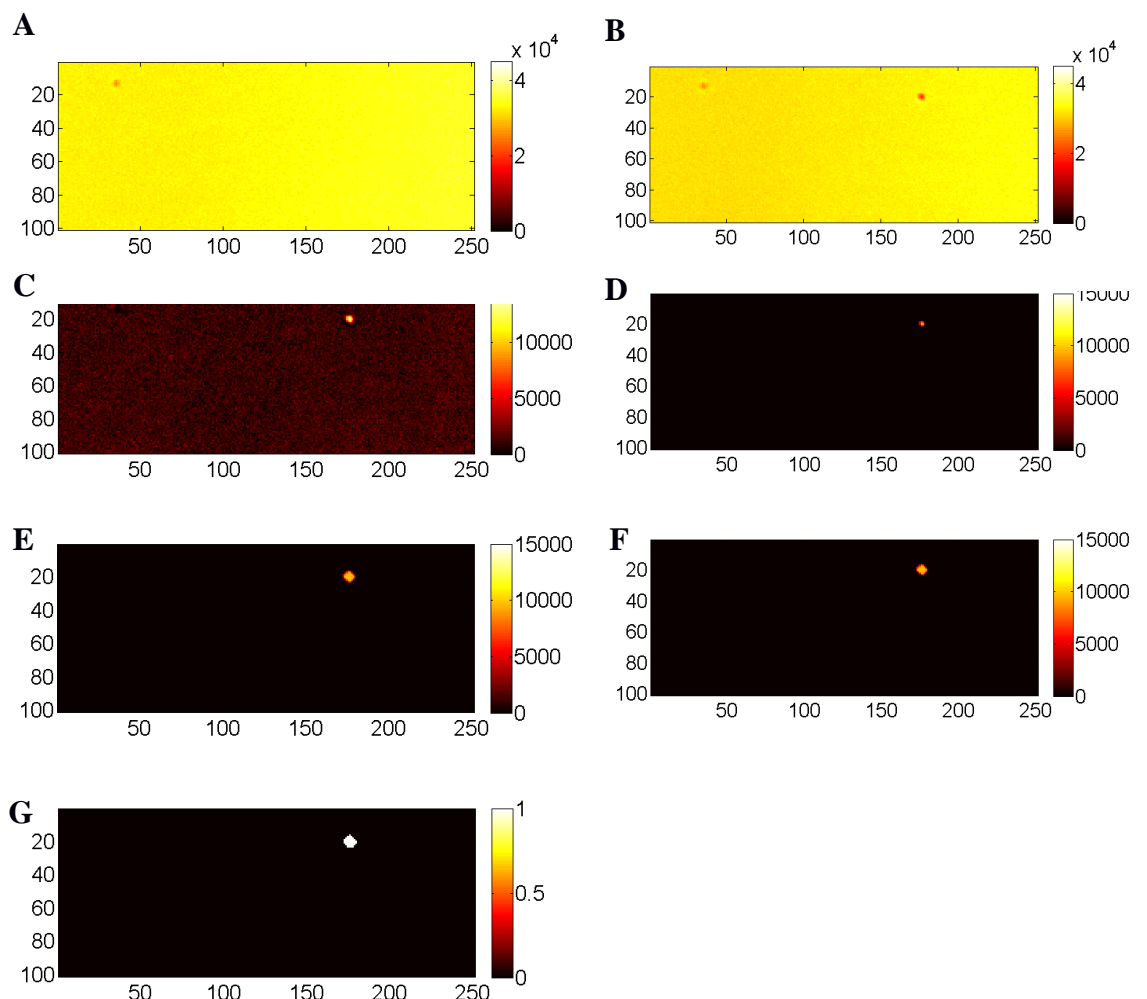


Figure 5.2 Example of object segmentation sequence. Images were cropped to the size of the tracked path and corresponds to tracked object number three in the results at $t = 4000s$. **A** – Initial image before particles were added to solution at $t = 0$. **B** – Frame of interest with at $t = 4000s$. **C** – Image subtraction to remove background, frame B from frame A. **D** – Adjust image contrast to remove noisy background. **E** – Dilate image object with disk shape, size = 2. **F** – Close image objects with disk shape, size = 8. **G** – Ostu segmentation resulted in a binary image of the object of interest. This mask was then applied on to the waveguide channel image to locate the microsphere and extract values including the mean and maximum intensity. Axes of the figures are in pixels, $50\text{pixels} \approx 28.7\mu\text{m}$

The images in both channels were subtracted by an initial image of the respective channel to remove any background artefacts and parameters were extracted from the subtracted image. The parameters for each tracked object in both bright-field and waveguide channels were the mean intensity, maximum intensity, area and centre position.

As a control for monitoring the background intensity of the tracked path, where possible, the mean intensity of two 20 by 20 pixels reference windows located 5 by 5 pixels away from the entire tracked path are monitored in both channels. The reference windows were placed outside the tracked path to avoid the signal of the tracked object. In some data sets, it was not possible to include both reference windows because one reference window was located outside the image. Figure 5.3 illustrates the location of reference windows in relation to the tracked path.

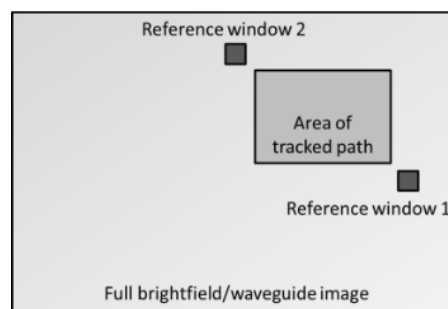


Figure 5.3 A schematic showing the location of reference windows 1 and 2. The size of the reference windows were 20 by 20 pixels and were located 5 by 5 pixels away from the top left vertex and bottom right vertex of the tracked path.

5.2.4 Analysing parameters from tracked objects

The mean and maximum intensity of the tracked objects were calculated for each frame and were normalised across the tracked duration. The normalised values were plotted against time in both channels. Also, the normalised mean intensity, standard deviation and range (difference between the maximum grey value and the minimum grey value) over the duration of the entire track were calculated.

To compare the variation between the bright-field data and the waveguide data, the coefficient of variation for each channel was calculated by taking the standard deviation of the entire track over the mean of the entire track for seven

different particles. The coefficient of variation provides an indication of how the variability of data is compared to the mean.

$$\text{Coefficient of variation} = \frac{\sigma}{\mu}$$

Eq. 5.1

5.3 Results

In-focus clusters of microsphere at several time points, under bright-field and waveguide illumination are shown in Figure 5.4. A 20 by 20 pixel window was located inside three white clusters of each image; the greyscale values were normalised in both channels and the coefficient of variation are shown in Table 5.1. All results displayed higher coefficient of variation in the waveguide channel than the bright-field channel, which suggests that there is a difference in signal response under the two types of illumination.

Image	Coefficient of Variation					
	Bright-field			Waveguide		
	Cluster 1	Cluster 2	Cluster 3	Cluster 1	Cluster 2	Cluster 3
t = 100	0.396	0.301	0.190	0.586	0.729	0.583
t = 110	0.354	0.301	0.190	0.553	0.541	0.543
t = 120	0.322	0.367	0.236	0.553	0.684	0.586
t = 325	0.296	0.158	0.384	0.509	0.634	0.611

Table 5.1 Coefficient of variation for clusters of microsphere under bright-field and waveguide illumination.

Figure 5.5 A – H are images of out of focus moving microspheres in solution at different time intervals. The images were normalised in both channels to see if the out of focus clusters appear in the waveguide channel. The normalised images suggest that the out of focus microsphere are not observable in the waveguide results.

A summary of the normalised mean intensity over time, standard deviation and coefficient of variation are presented in Table 5.2. For all tracked objects, the normalised mean intensity over time in the bright-field channel was higher than that in the waveguide channel. The coefficients of variation of tracked object numbers 2 and 3 were greater than one in the waveguide channel, whereas tracked objects numbers 1, 4 – 7, displayed coefficient of variation between 0.346 and 0.675. The coefficients of variation for the bright-field channel ranged from 0.181 to 0.452. Similarly, reference windows that were positioned outside the tracked path were analysed and yielded coefficient of variations ranging from 0.283 to 0.383 for the waveguide channel and 0.272 to 0.764 in the bright-field channel.

Tracked Object Number	Normalised Mean Intensity (a.u)		STD		CV	
	Bright-field	Waveguide	Bright-field	Waveguide	Bright-field	Waveguide
1	0.344	0.178	0.156	0.120	0.452	0.675
2	0.717	0.032	0.203	0.044	0.297	1.379
3	0.507	0.043	0.124	0.084	0.245	1.960
4	0.413	0.275	0.128	0.129	0.310	0.468
5	0.730	0.313	0.132	0.138	0.181	0.442
6	0.640	0.230	0.132	0.117	0.207	0.508
7	0.723	0.425	0.170	0.147	0.235	0.346

Table 5.2 Summary of normalised mean intensity, standard deviation(STD) and coefficient of variation (CV) for each tracked object in bright-field channel and waveguide channel. Arbitrary units = a.u

Examining Figure 5.7Figure 5.8A and Figure 5.7Figure 5.8B of tracked objects 2 and 3, intensity spikes were observed in the waveguide channel and the same spikes were not observed in the bright-field channel or in the reference windows. For tracked object number 2, the maximum mean intensity over time reached 712a.u and the maximum max intensity over time was 2448a.u. Similarly, for tracked object number 3, the spike in mean intensity reached 800a.u and the maximum intensity over time reached 3280a.u. For detailed results of tracked objects 5, 6 and 7, please refer to Appendix VII

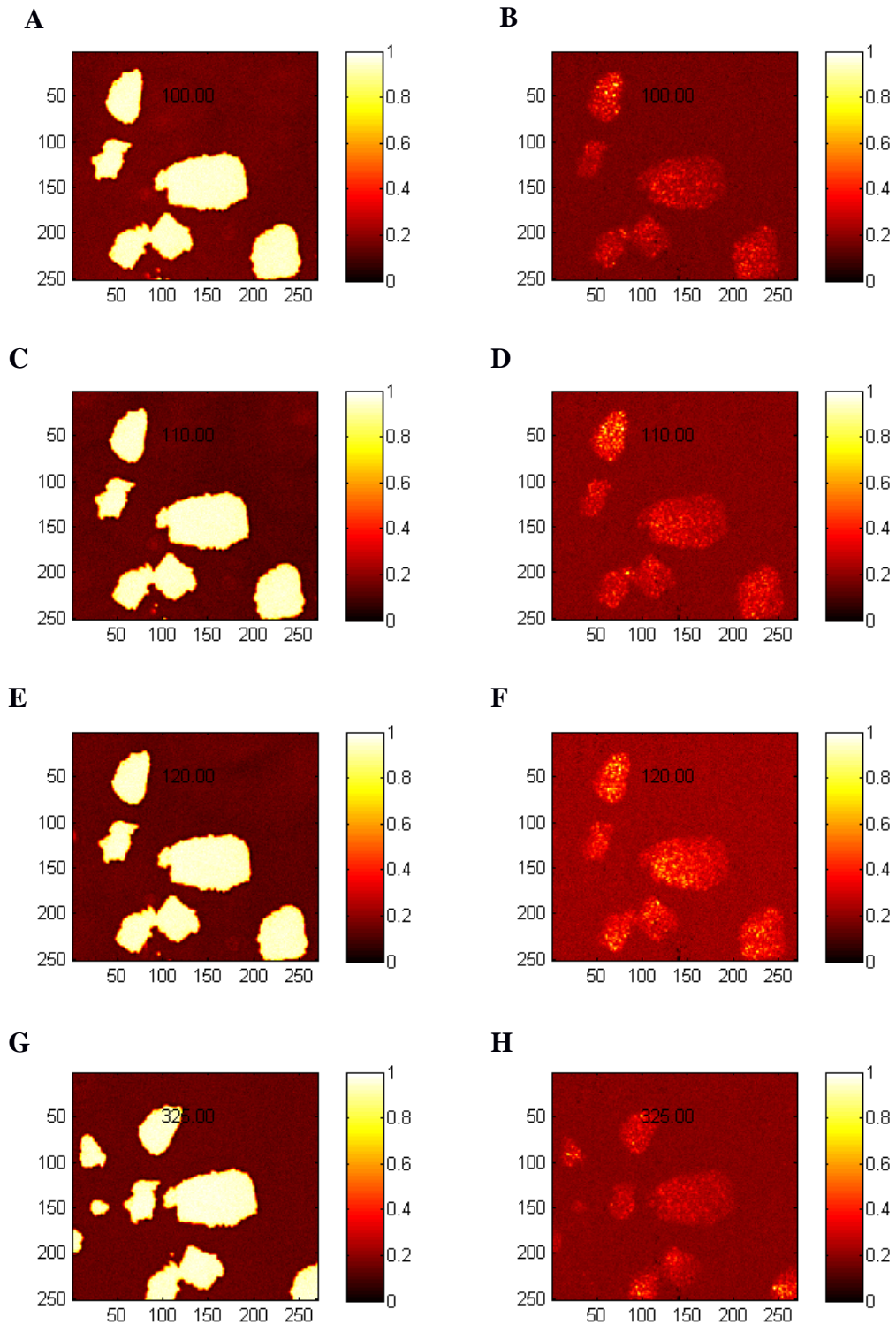


Figure 5.4 Snapshots showing image sequence of microspheres moving in an aqueous solution under bright-field illumination and waveguide illumination at time points 100s (A,B), 110s(C,D), 120s(E,F) and 325s(G,H). Bright-field channel(left) and waveguide channel(right). In focus clusters can be seen under both channel, but the variation inside the clusters are higher in the waveguide results than the bright-field results after normalisation. Note: This data set was collected in the same way as described in materials and methods, but only part of the data is presented. This data set was not used for tracking because particles were clumped together, but is included for qualitative analysis of the response of out-of-focus and in-focus objects in both bright-field and waveguide channels. Axes of the figures are in pixels, 50pixels \approx 28.7 μ m.

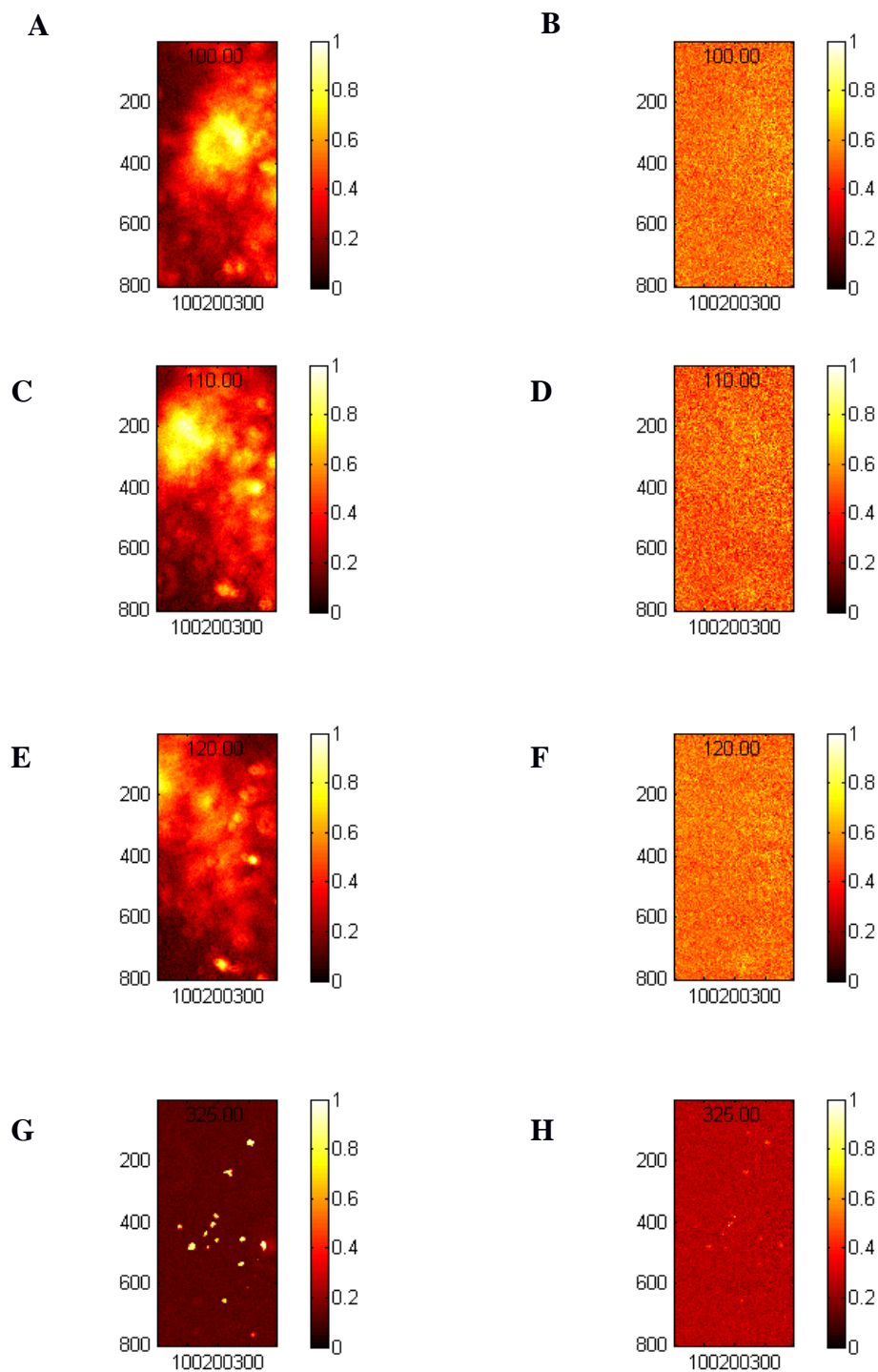


Figure 5.5 Snapshots showing image sequence of microspheres moving in an aqueous solution under bright-field illumination and waveguide illumination at time points 100s (A,B), 110s(C,D), 120s(E,F) and 325s(G,H). Bright-field channel(left) and waveguide channel(right). Floating out-of-focus cluster of microspheres can be seen clearly under bright-field illumination and appears to be undetected under waveguide illumination. Note: This data set was not used for tracking because particles were clumped together, but is included for qualitative analysis of the response of out-of-focus and in-focus objects in both bright-field and waveguide channels. Axes of the figures are in pixels, 100pixels \approx 57.5 μ m

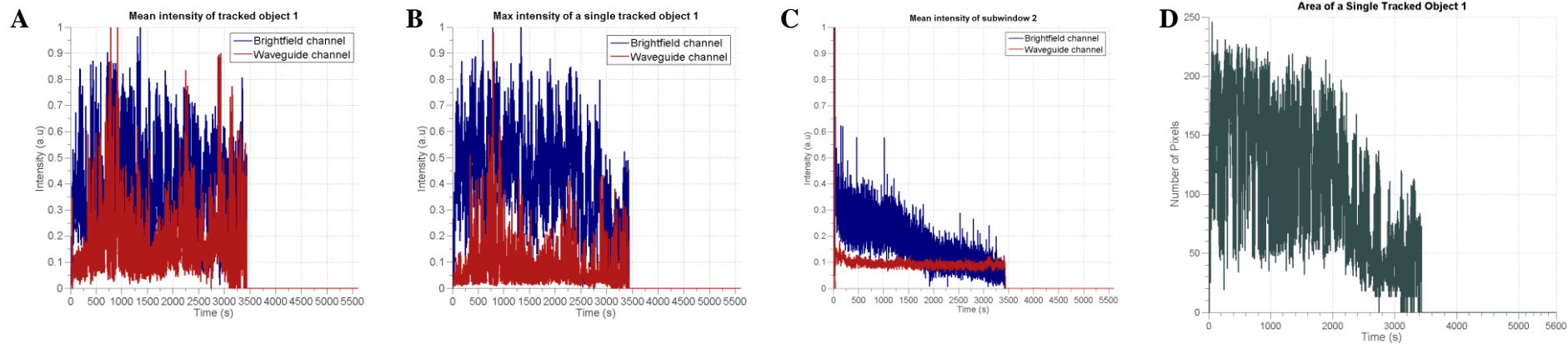
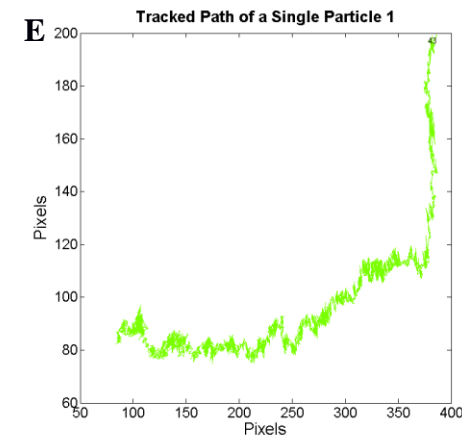


Figure 5.6 Tracked object 1 – A - Mean intensity of the tracked object vs. time in both bright-field and waveguide channels. B - Maximum intensity of the track object against time. C - Mean intensity of reference window2 outside the path of the tracked object. D - Area of the tracked object against time. E - Path taken by the tracked object in green.

Table 5.3 Data statistics of the tracked object throughout its tracked path in both brightfied(BF) and waveguide(WG) channels . STD = Standard deviation; CV = coefficient of variation.

	Data statistics of the tracked object across the tracked path							
	Mean(a.u)		STD(a.u)		Range(grey value)		CV	
	BF	WG	BF	WG	BF	WG	BF	WG
A. Mean intensity of tracked object	0.3439	0.178	0.1555	0.1201	2513	696	0.4523	0.6745
B. Max intensity of tracked object	0.4248	0.0816	0.1746	0.0758	8704	10128	0.411	0.9295
C. Mean intensity of subWindow2	0.1752	0.0956	0.0986	0.0366	86.6	195.3	0.563	0.383



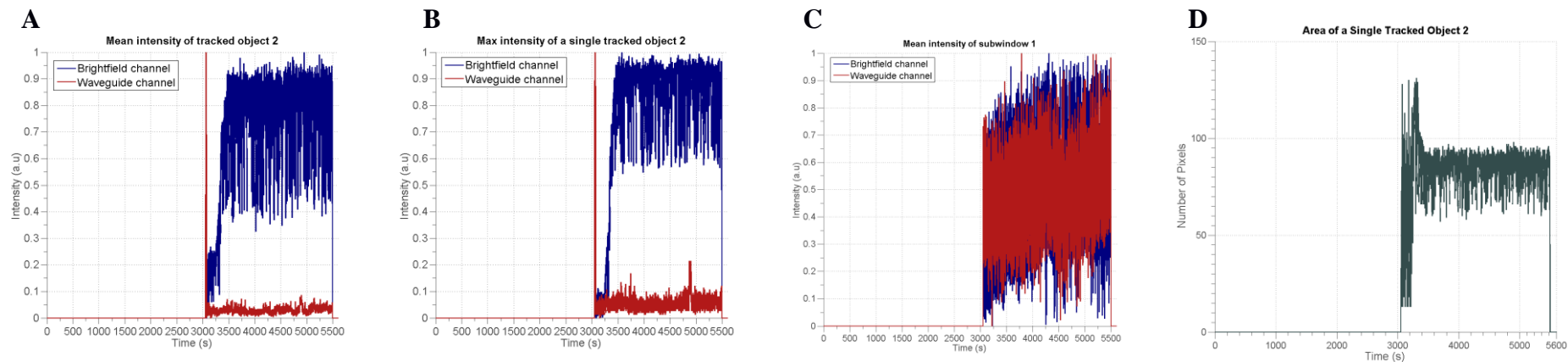
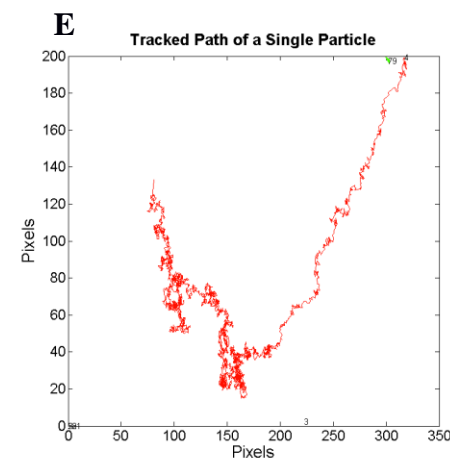


Figure 5.7 Tracked object 2 – A - Mean intensity of the tracked object vs. time in both bright-field and waveguide channels. B - Maximum intensity of the track object against time. Smaller plots in both A and B shows the enlarged regions of the waveguide channel and arrows indicating the intensity spike. C - Mean intensity reference window 2 outside the path of the tracked object. D - Area of the tracked object against time. E - Path taken by the tracked object in red.

Table 5.4 Data statistics of the tracked object throughout its tracked path in both brightfield(BF) and waveguide(WG) channels. STD = Standard deviation: CV = coefficient of variation.

	Data statistics of the tracked object across the tracked path							
	Mean(a.u)		STD(a.u)		Range(a.u)		CV	
	BF	WG	BF	WG	BF	WG	BF	WG
A. Mean intensity of tracked object	0.7168	0.0321	0.2026	0.0442	5702	706.1	0.297	1.379
B. Max intensity of tracked object	0.7873	0.0559	0.2655	0.0609	27424	2384	0.337	1.089
C. Mean intensity of subWindow1	0.3919	0.4937	0.199	0.1397	556	11.5	0.508	0.283



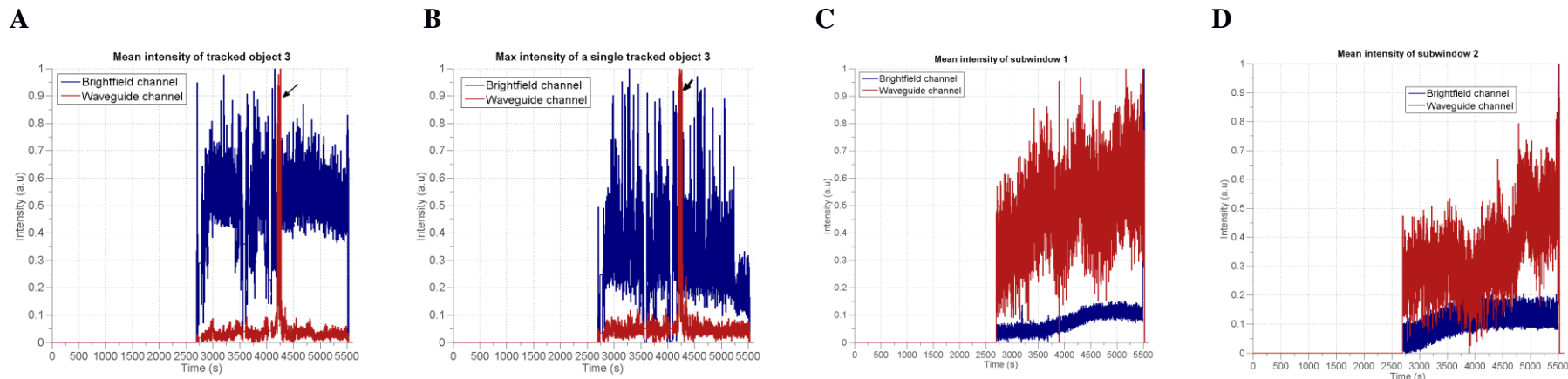
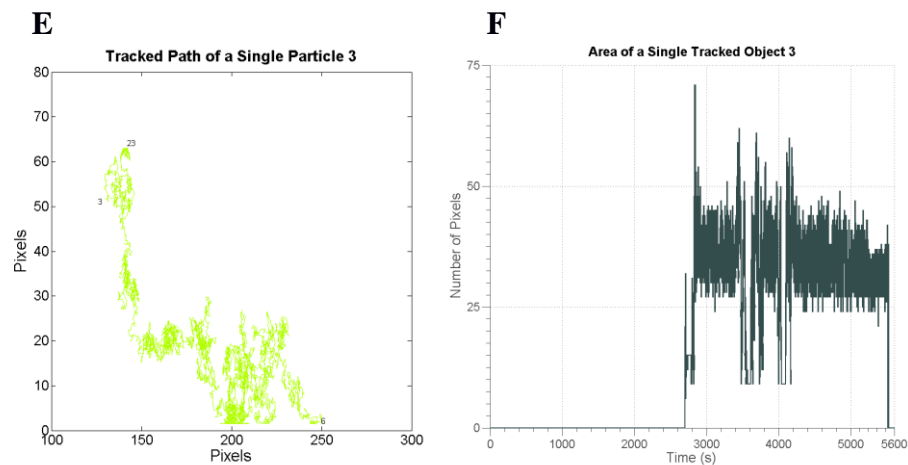


Figure 5.8 Tracked object 3 – A - Mean intensity of the tracked object vs. time in both bright-field and waveguide channels. B - Maximum intensity of the track object against time. C , D - Mean intensity of reference window 1 and reference window 2 outside the path of the tracked object. E - Area of the tracked object against time. F - Path taken by the tracked object in lime green.

Table 5.5 Data statistics of the tracked object throughout its tracked path in both brightfied(BF) and waveguide(WG) channels. STD = Standard deviation; CV = coefficient of variation.

	Data statistics of the tracked object across the tracked path							
	Mean(a.u)		STD(a.u)		Range(a.u)		CV	
	BF	WG	BF	WG	BF	WG	BF	WG
A. Mean intensity of tracked object	0.5071	0.0429	0.1244	0.0841	5417	800	0.245	1.960
B. Max intensity of tracked object	0.3019	0.059	0.1452	0.1079	18320	3280	0.481	1.829
C. Mean intensity of subWindow1	0.0784	0.4934	0.0599	0.1422	2812	15.7	0.764	0.288
D. Mean intensity of subWindow2	0.1009	0.3476	0.068	0.1188	2820	23.3	0.674	0.342



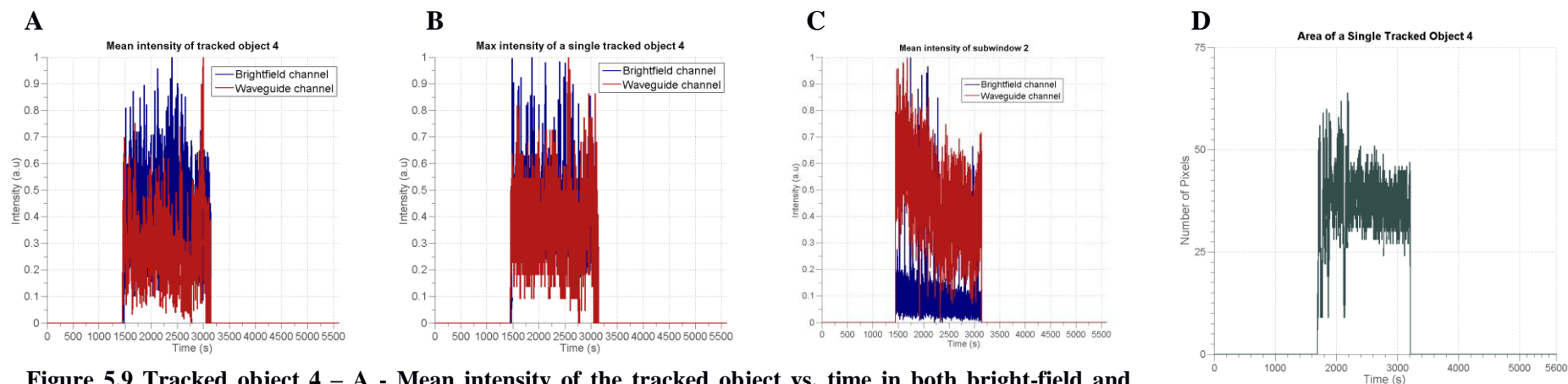
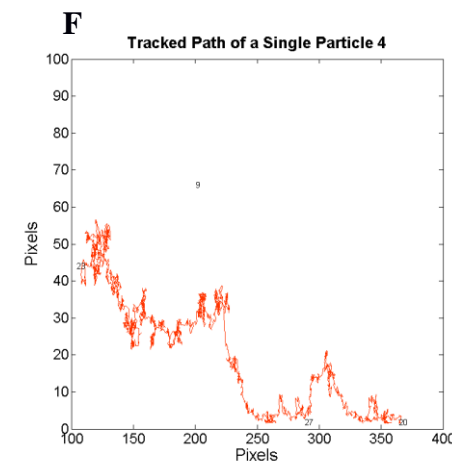


Figure 5.9 Tracked object 4 – A - Mean intensity of the tracked object vs. time in both bright-field and waveguide channels. B - Maximum intensity of the track object against time. C – Mean intensity of reference window 2 placed outside the path of the tracked object. D - Area of the tracked object against time. E - Path taken by the tracked object in orange.

Table 5.6 Data statistics of the tracked object throughout its tracked path in both brightfied(BF) and waveguide(WG) channels. STD = Standard deviation; CV = coefficient of variation.

	Data statistics of the tracked object across the tracked path							
	Mean(a.u)		STD(a.u)		Range(a.u)		CV	
	BF	WG	BF	WG	BF	WG	BF	WG
A. Mean intensity of tracked object	0.4125	0.2754	0.1277	0.1291	5230	70.7	0.310	0.469
B. Max intensity of tracked object	0.3897	0.363	0.1292	0.127	13702	256	0.332	0.350
C. Mean intensity of subWindow2	0.0908	0.4604	0.0647	0.1499	NA	14.8	0.713	0.326



5.4 Discussion

Qualitatively, the difference in the effect of transmission illumination and evanescent field illumination can be seen in Figure 5.4A-G. The two clusters of microspheres appeared to have similar intensity values in the bright-field, whereas the intensity for some clusters in the waveguide were less uniform and varied between time points. Normally, low variation in signal is a desired quality, but in this case, variation in intensity could imply the penetration of the evanescent field at different depths. The coefficient of variation for the clusters were higher in the waveguide results than the bright-field results, which suggests that the source of illumination had caused this effect and using evanescent field illumination makes depth discrimination feasible. In addition to this, moving clusters of out-of-focus microspheres were detected in the bright-field channel and not in the waveguide channel. This suggests that the sensitivity to floating object is higher using transmission illumination than evanescent field illumination.

In the waveguide channel, a signal is expected only when an object is within the evanescent field and when an object is outside the evanescent, little or no signal is expected. When an object moves into the evanescent field, an increase in intensity is detected and when it moves outside the evanescent field, the intensity will decrease. Two out of the seven tracked objects displayed high variation of signal due to an intensity spike within the data and this suggests the objects were briefly moved into the evanescent field, which scattered more light onto the detector; when it moved outside of the evanescent field, the scattered light dropped back to the previous level of signal.

It can be seen that in the waveguide channel of tracked objects 2 and 3, the coefficient of variation for mean intensity of the tracked object were above 1 which meant the overall standard deviation was greater than the mean and suggest the data points have large variations from the mean. On contrary to this, the coefficients of variation in the bright-field channel were only 0.297 and 0.245 respectively. This implies the variation with respect to the mean intensity in the bright-field channel was smaller than the waveguide channel.

Reviewing the data of tracked object number 2, it shows that the position of the waveguide spike was at the beginning of the tracked path and although there was also an increase in the bright-field channel, the bright-field value remained high which does not explain the spike in the waveguide channel. Also, the coefficients of variation for reference window 1 were 0.508 and 0.283 in the bright-field and waveguide channel respectively. Reference window 1 was a fixed part of the image that was outside the view of the tracked path and it was assumed that the signal from reference window 1 was the background signal and was unaffected by the tracked particle. Since the coefficients of variation for reference window 1 were lower for both channels, this implies the large variation in the waveguide channel was not a result of the background variation.

Similarly, an intensity spike was observed in the waveguide channel of tracked object number 3 and was not observed in the bright-field channel or in reference window 1 and reference window 2. The coefficient of variation for reference window 1 and reference window 2 was 0.764 and 0.674 for the bright-field channel and 0.288 and 0.342 in the waveguide channel. Again, the lower variation in the sub-windows implies the spike was not caused by background variations and was only detected in the waveguide channel. This could be as a result of the microsphere moving at close proximity to the interface and scattering the evanescent field.

Another observation is a variation of the bright-field mean intensity throughout the tracked path and this can be attributed to the area of the tracked object. Comparing Figure 5.8A for the mean bright-field intensity and Figure 5.8E of the tracked object area, it can be seen that there is a similarity between the profile of the bright-field mean intensity and the object area. Both mean intensity and the object area were decreased at around 3500s and 4000s, which suggests the variation of the bright-field mean intensity over time was caused by the segmentation of the track object between frames during image processing.

Figures 5.6-9 E shows the path taken in the image by the tracked object and the random motion suggests the objects were under Brownian motion. This indicates the possibility that random movements generated the spikes within

mean intensity values and the tracked object scattering the evanescent field may cause the spikes.

It is also apparent that the coefficient of variation of the tracked objects for the bright-field channel was always lower than the waveguide channel. The result of this suggests the signal in the waveguide channel was more variable than the bright-field signal. An explanation for this is that little or no signal is expected when an object is outside the evanescent field. Therefore, the signal is shot noise limited, but in bright-field illumination, an object is always illuminated in the field of view and the signal is always high, hence the shot noise becomes insignificant compared to other sources of noise; when an object scatters the evanescent field, the number of photons hitting the detection pixel is much higher as seen in the spiked intensity of tracked objects 2 and 3 and again, the shot noise becomes indistinguishable compared to other types of noise. Shot noise can be reduced by using a higher powered illumination source or increasing the exposure time, but motion blur effects from the moving particle will also become more apparent when the exposure time is increased, where a trail of the microsphere is left across the image. Another factor that could contribute to the higher variation in the waveguide channel is the difference in exposure times between the two channels. The exposure times were 1ms and 500ms for the bright-field and waveguide channel respectively and gain was not used. The large difference in exposure times was because the power difference between the two illumination sources and the scattered signal is low in the waveguide channel compared to the transmitted signal in the bright-field channel. The motion of the object within the 500ms of exposure time can have motion blur effects and lead to higher variation in the waveguide channel than the bright-field channel.

For tracked object 1, although the coefficient of variation is less than one for the waveguide channel, the maximum intensity reached 10128a.u. which was higher than the maximum intensity for tracked object 2 (2384a.u.) and tracked object 3 (3280a.u.). The coefficient of variation was lower for tracked object 1 than for tracked objects 2 and 3 because the signal from tracked object 1 was frequently high, which lowers the standard deviation and also the coefficient of variation. Such high intensity was not observed in the reference window that

lies outside the tracked path and also, the coefficient of variation in the sub-window was only 0.383 opposed to 0.675 for the tracked object in the waveguide channel. Also, the profile of the variation was different for the bright-field and waveguide channels, together with the bright-field channel profile matching the tracked area profile; all of this implies that the signal of the waveguide channel could be a result from the scattered evanescent field.

5.5 Conclusion

Tracking microspheres under Brownian motion in solution was used to test the principle of evanescent field illumination. Some microspheres moved in and out of the evanescent field that resulted in an intensity spike that was only observable in the waveguide channel and not the bright-field channel. In turn, this led to a higher coefficient of variation between the intensity data of the two channels. Other microspheres remained outside of the evanescent field and little signal was measured in the waveguide channel and led to a lower coefficient of variation. In one case, the microsphere was within the evanescent field for most of the tracked path and so high intensity was observed more frequently which lowered its coefficient of variation.

Comparing the effects of evanescent field illumination and bright-field illumination, the ability of depth discrimination under evanescent field illumination using a laser source was shown. Also, only some of the microspheres were observed suggesting that the main contribution of the signal in the waveguide image is from evanescent field illumination. Otherwise, all microspheres would be visible with a lower intensity. This study demonstrated the potential use of evanescent field illumination through a waveguide to determine the adhesion of biological materials to the surface.

Chapter 6 Conclusion

6.1 Summary

The advantage of evanescent illumination was shown in Chapter 2 . Using an objective based TIRM system, high resolution label-free images exposed a fraction of the cell membrane and the extracellular matrix layer was imaged during osteogenic differentiation. The TIRM system uses a high NA objective which is costly, reduces the field of view and couples heat from the incubator through the immersion oil causing focal drift. The demand for adaptability in a manufacturing setting has led to the development of an alternate solution based on evanescent waveguide system.

Opposed to TIRM, the image of the waveguide system is formed by collecting the scattered signal from frustrated total internal reflection; this results in a dark field image where the object of interest appears bright over a dark background. Under waveguide configuration, less alignment is required due to the lack of condenser compared to the prism configuration. Total internal reflection can be achieved over a larger area by illuminating from the edge of the waveguide and on thicker substrates; making low powered objectives more suitable in this imaging mode.

In the studies discussed in previous chapters, two types of evanescent waveguide systems were evaluated; an LED illuminated system was presented in Chapter 3 and the laser illuminated system was presented in Chapter 4 . Under LED illumination, a high intensity offset was visible at large separation distances from the glass/water interface. This was attributed to the rough edge of the waveguide which refracted light to strike the interface at angles below the critical angle. It was shown that by using a polished waveguide and a collimated laser source, the high intensity offset was reduced from 50% to 10%. Tracking microspheres in both bright-field mode and waveguide mode further validated the detection of waveguide signal only when an object is within the evanescent field.

An advantage of using a coherent source is the ease of changing the evanescent field depth by changing the incident angle as presented. However, due to the

setup of the system disclosed, the power input to the waveguide with respect to the incident angle changes as a function of cosine; this needs to be calibrated for future experiments where the separation distance is quantified by the intensity at illuminating at different incident angles.

Additionally, the speckle effects produced by interference of reflected rays are yet to be evaluated for biological samples. Placement of a diffuser within the optical path can produce spatially incoherent illumination, but this will also change the incident angle. Also, most laser sources will illuminate the sample unevenly with a Gaussian distribution, which could mislead the interpretation of displacement intensity across the sample.

It is still worth pursuing a LED waveguide system given the advantages of using an incoherent source. The restriction of incident angles produced by the LED source was attempted by placing an aperture in front of the waveguide and by displacing the waveguide away from the source. It is noted that this is not the most effective method and other methods are discussed in Appendix VIII.

Although the LED illuminated system presented in Chapter 3 appears to be unsuitable for the application of detecting adhesion of biological materials to the surface, there are still advantages compared to a dark field microscope. Kawano et al. (75) reported a similar system that coupled an array of LEDs at the edge of the microscopy slide to illuminate the entire sample. The internal reflected light travelled through the sample and was reflected back into the slide when it reached the air interface; this is analogous to the waveguide system presented. The dark field internal reflection illumination (DIRI) was made to be a part of current microscope systems and was applied to whole slide imaging for tissue sections where a large field of view was advantageous to see the entire slide. The advantages of DIRI over conventional transmission dark field system are the lack of condenser, removing the need to align with the objective which is critical in conventional dark field microscopy; less halo effects in DIRI images, the objects within the image are more accurately presented and out of focus dust on slide is less apparent using DIRI than transmission dark field illumination.

The waveguide system used in the studies cannot accommodate live cells and it is an important feature for live cell studies. In a manufacturing setting, the optimal solution would be to build the imaging system within a standard incubator using standard tissue culture flasks as the waveguide. So images of the flask can be acquired *in-situ* without disturbance.

Bibliography

1. Research C for BE and. FDA: Marketed Cell Therapy Products [Internet]. Center for Biologics Evaluation and Research; [cited 2015 May 11]. Available from: <http://www.fda.gov/BiologicsBloodVaccines/CellularGeneTherapyProducts/ApprovedProducts/>
2. Cheever MA, Higano CS. PROVENGE (Sipuleucel-T) in prostate cancer: the first FDA-approved therapeutic cancer vaccine. *Clin Cancer Res.* 2011 Jun 1;17(11):3520–6.
3. Knee Cartilage Repair and Pain Treatment Options | CARTICEL® [Internet]. [cited 2015 May 14]. Available from: <http://www.carticel.com/>
4. Apligraf : What is Apligraf? [Internet]. [cited 2015 May 14]. Available from: http://www.apligraf.com/professional/what_is_apligraf/
5. Dermagraft [Internet]. [cited 2015 May 14]. Available from: <http://www.dermagraft.com/home/>
6. Search of: cell therapy | Open Studies - List Results - ClinicalTrials.gov [Internet]. [cited 2014 Sep 27]. Available from: <https://clinicaltrials.gov/ct2/results?term=cell+therapy&recr=Open>
7. Fang Y. Label-free cell-based assays with optical biosensors in drug discovery. *Assay Drug Dev Technol.* 2006 Oct;4(5):583–95.
8. Zang R, Li D, Tang I-C, Wang J, Yang S-T. Cell-Based Assays in High-Throughput Screening for Drug Discovery. *Int J Biotechnol Wellness Ind.* 2012;1(1):31–51.
9. Ebert AD, Liang P, Wu JC. Induced pluripotent stem cells as a disease modeling and drug screening platform. *J Cardiovasc Pharmacol.* 2012 Oct;60(4):408–16.
10. Singh VK, Kalsan M, Kumar N, Saini A, Chandra R. Induced pluripotent stem cells: applications in regenerative medicine, disease modeling, and drug discovery. *Front cell Dev Biol.* 2015 Jan;3:2.
11. CFR - Code of Federal Regulations Title 21.
12. Eloit M. Risks of virus transmission associated with animal sera or substitutes and methods of control. *Dev Biol Stand.* 1999 Jan;99:9–16.
13. Shah G. Why do we still use serum in the production of biopharmaceuticals? *Dev Biol Stand.* 1999 Jan;99:17–22.

14. Wessman SJ, Levings RL. Benefits and risks due to animal serum used in cell culture production. *Dev Biol Stand.* 1999 Jan;99:3–8.
15. O'Driscoll L, Gammell P, McKiernan E, Ryan E, Jeppesen PB, Rani S, et al. Phenotypic and global gene expression profile changes between low passage and high passage MIN-6 cells. *J Endocrinol.* 2006 Dec;191(3):665–76.
16. Esquenet M, Swinnen J V, Heyns W, Verhoeven G. LNCaP prostatic adenocarcinoma cells derived from low and high passage numbers display divergent responses not only to androgens but also to retinoids. *J Steroid Biochem Mol Biol.* 1997 Aug;62(5-6):391–9.
17. Briske-Anderson MJ, Finley JW, Newman SM. The influence of culture time and passage number on the morphological and physiological development of Caco-2 cells. *Proc Soc Exp Biol Med.* 1997 Mar;214(3):248–57.
18. Chang-Liu CM, Woloschak GE. Effect of passage number on cellular response to DNA-damaging agents: cell survival and gene expression. *Cancer Lett.* 1997 Feb 26;113(1-2):77–86.
19. Wenger SL, Senft JR, Sargent LM, Bamezai R, Bairwa N, Grant SG. Comparison of established cell lines at different passages by karyotype and comparative genomic hybridization. *Biosci Rep.* 2004 Dec;24(6):631–9.
20. Jayme DW, Smith SR. Media formulation options and manufacturing process controls to safeguard against introduction of animal origin contaminants in animal cell culture. *Cytotechnology.* 2000 Jul;33(1-3):27–36.
21. Castle P, Robertson JS. Summary and conclusion. Animal sera, animal sera derivatives and substitutes used in the manufacture of pharmaceuticals. *Dev Biol Stand.* 1999 Jan;99:191–6.
22. Merten OW. Development of serum-free media for cell growth and production of viruses/viral vaccines--safety issues of animal products used in serum-free media. *Dev Biol (Basel).* 2002 Jan;111:233–57.
23. Keenan J, Pearson D, Clynes M. The role of recombinant proteins in the development of serum-free media. *Cytotechnology.* 2006 Mar;50(1-3):49–56.
24. Brunner D, Frank J, Appl H, Schöffl H, Pfaller W, Gstraunthaler G. Serum-free cell culture: the serum-free media interactive online database. *ALTEX.* 2010 Jan;27(1):53–62.

25. Healy L, Young L, Stacey GN. Stem cell banks: preserving cell lines, maintaining genetic integrity, and advancing research. *Methods Mol Biol.* 2011 Jan;767:15–27.
26. Choi HS, Kim W-T, Ryu CJ. Antibody approaches to prepare clinically transplantable cells from human embryonic stem cells: identification of human embryonic stem cell surface markers by monoclonal antibodies. *Biotechnol J.* 2014 Jul;9(7):915–20.
27. Sergent-Tanguy S, Chagneau C, Neveu I, Naveilhan P. Fluorescent activated cell sorting (FACS): a rapid and reliable method to estimate the number of neurons in a mixed population. *J Neurosci Methods.* 2003 Oct 15;129(1):73–9.
28. Watt FM, Jordan PW, O’Neill CH. Cell shape controls terminal differentiation of human epidermal keratinocytes. *Proc Natl Acad Sci U S A.* 1988 Aug;85(15):5576–80.
29. Schilling Z, Frank E, Magidson V, Wason J, Lončarek J, Boyer K, et al. Predictive-focus illumination for reducing photodamage in live-cell microscopy. *J Microsc.* 2012 May;246(2):160–7.
30. Dixit R, Cyr R. Cell damage and reactive oxygen species production induced by fluorescence microscopy: effect on mitosis and guidelines for non-invasive fluorescence microscopy. *Plant J.* 2003 Oct;36(2):280–90.
31. Rieder CL, Cole R. Microscopy-induced radiation damage, microtubules, and progression through the terminal stage of G2 (prophase) in vertebrate somatic cells. *Cold Spring Harb Symp Quant Biol.* 2000 Jan;65:369–76.
32. Magidson V, Khodjakov A. Circumventing photodamage in live-cell microscopy. *Methods Cell Biol.* 2013 Jan;114:545–60.
33. N B, P J. Extracellular matrix and integrin signalling: the shape of things to come. Portland Press Ltd.; 1999 May 1;
34. Barczyk M, Carracedo S, Gullberg D. Integrins. *Cell Tissue Res.* 2010 Jan;339(1):269–80.
35. Heino J, Huhtala M, Käpylä J, Johnson MS. Evolution of collagen-based adhesion systems. *Int J Biochem Cell Biol.* 2009 Feb;41(2):341–8.
36. Ploem JS. Reflection-contrast microscopy as a tool for investigation of the attachment of living cells to a glass surface. *Mononucleated phagocytes immunity, Infect Pathol Blackwell, Oxford.* 1975;405–21.
37. Verschueren H. Interference reflection microscopy in cell biology: methodology and applications. *J Cell Sci.* 1985;301:279–301.

38. Ambrose EJ. A Surface Contact Microscope for the study of Cell Movements. *Nature*. 1956 Nov 24;178(4543):1194–1194.
39. Byrne GD, Pitter MC, Zhang J, Falcone FH, Stolnik S, Somekh MG. Total internal reflection microscopy for live imaging of cellular uptake of sub-micron non-fluorescent particles. *J Microsc*. 2008 Jul;231(Pt 1):168–79.
40. Raether H. *Surface plasmons on smooth surfaces*. Springer; 1988.
41. Rothenhäusler B, Knoll W. *Surface plasmon microscopy*. Nature Publishing Group; 1988;
42. Giebel K-F, Bechinger C, Herminghaus S, Riedel M, Leiderer P, Weiland U, et al. Imaging of cell/substrate contacts of living cells with surface plasmon resonance microscopy. *Biophys J*. Elsevier; 1999;76(1):509–16.
43. Hecht E. *Optics*. Addison-Wesley; 2002.
44. De Fornel F. *Evanescent Waves: From Newtonian Optics to Atomic Optics*. Springer; 2001.
45. Marciante JR, Hirsh JI, Raguin DH, Prince ET. Polarization-insensitive high-dispersion total internal reflection diffraction gratings. *J Opt Soc Am A Opt Image Sci Vis*. 2005;22(2):299–305.
46. Popov E, Mashev L, Maystre D. Back-side diffraction by relief gratings. *Opt Commun*. 1988;65(2):97–100.
47. Försterling K. Über die Messung der optischen Konstanten sehr dünner Metallschichten. *Ann Phys*. 1937;422(8):745–51.
48. Court IN, Willisen FK Von. Frustrated Total Internal Reflection and Application of Its Principle to Laser Cavity Design. *Appl Opt*. 1964;3(6):719.
49. Grandin HM, Städler B, Textor M, Vörös J. Waveguide excitation fluorescence microscopy: A new tool for sensing and imaging the biointerface. *Biosens Bioelectron*. 2006;21(8):1476–82.
50. Hassanzadeh A, Nitsche M, Mittler S, Armstrong S, Dixon J, Langbein U. Waveguide evanescent field fluorescence microscopy: Thin film fluorescence intensities and its application in cell biology. *Appl Phys Lett*. 2008;92(23):1–4.
51. Hassanzadeh A, Armstrong S, Dixon SJ, Mittler S. Multimode waveguide evanescent field fluorescence microscopy: Measurement of cell-substratum separation distance. *Appl Phys Lett*. 2009;94(3):1–4.

52. Hassanzadeh A, Nitsche M, Armstrong S, Nabavi N, Harrison R, Dixon SJ, et al. Optical waveguides formed by silver ion exchange in Schott SG11 glass for waveguide evanescent field fluorescence microscopy: evanescent images of HEK293 cells. *J Biomed Opt.* 2010;15(3):036018.
53. Knight DK, Stutchbury R, Imruck D, Halfpap C, Lin S, Langbein U, et al. Focal contact formation of vascular smooth muscle cells on Langmuir-Blodgett and solvent-cast films of biodegradable poly(ester amide)s. *ACS Appl Mater Interfaces.* 2012;4(3):1303–12.
54. Agnarsson B, Ingthorsson S, Gudjonsson T, Leosson K. Evanescent-wave fluorescence microscopy using symmetric planar waveguides. *Opt Express.* 2009;17(7):5075.
55. Ramachandran S, Cohen D a, Quist AP, Lal R. High performance, LED powered, waveguide based total internal reflection microscopy. *Sci Rep.* 2013;3:2133.
56. Thoma F, Langbein U, Mittler-Neher S. Waveguide scattering microscopy. *Opt Commun. Elsevier;* 1997;134(1):16–20.
57. Horváth R, Pedersen HC, Larsen NB. Demonstration of reverse symmetry waveguide sensing in aqueous solutions. *Appl Phys Lett.* 2002;81(12):2166–8.
58. Horváth R, Lindvold LR, Larsen NB. Reverse-symmetry waveguides: Theory and fabrication. *Appl Phys B Lasers Opt.* 2002;74(4-5):383–93.
59. Horvath R, Pedersen HC, Skivesen N, Svanberg C, Larsen NB. Fabrication of reverse symmetry polymer waveguide sensor chips on nanoporous substrates using dip-floating. *J Micromechanics Microengineering.* 2005;15(6):1260–4.
60. Horvath R, Pedersen HC, Skivesen N, Selmeczi D, Larsen NB. Monitoring of living cell attachment and spreading using reverse symmetry waveguide sensing. *Appl Phys Lett.* 2005 Feb 7;86(7):071101.
61. Aref A, Horvath R, McColl J, Ramsden JJ. Optical monitoring of stem cell-substratum interactions. *J Biomed Opt.* 2013;14(1):010501.
62. Hill DJ, Pinion CW, Christesen JD, Cahoon JF. Waveguide Scattering Microscopy for Dark-Field Imaging and Spectroscopy of Photonic Nanostructures. *ACS Photonics.* 2014;140722113925003.
63. Steyer JA, Almers W. Tracking single secretory granules in live chromaffin cells by evanescent-field fluorescence microscopy. *Biophys J. Elsevier;* 1999;76(4):2262–71.

64. Mattheyses AL, Axelrod D. Direct measurement of the evanescent field profile produced by objective-based total internal reflection fluorescence. *J Biomed Opt. International Society for Optics and Photonics*; 2006;11(1):14006.
65. Gell C, Berndt M, Enderlein J, Diez S. TIRF microscopy evanescent field calibration using tilted fluorescent microtubules. *J Microsc. Wiley Online Library*; 2009;234(1):38–46.
66. Sarkar A, Robertson RB, Fernandez JM. Simultaneous atomic force microscope and fluorescence measurements of protein unfolding using a calibrated evanescent wave. *Proc Natl Acad Sci U S A. National Acad Sciences*; 2004;101(35):12882–6.
67. McKee CT, Clark SC, Walz JY, Ducker W a. Relationship between scattered intensity and separation for particles in an evanescent field. *Langmuir*. 2005;21(13):5783–9.
68. Pedrotti FL, Pedrotti LS, Pedrotti LM. *Introduction to Optics*. Pearson Prentice-Hall; 2007.
69. Hulst van NF, Boer de NP, Bölger B. An evanescent-field optical microscope. *J Microsc. Wiley Online Library*; 1991;163(2):117–30.
70. Reddick RC, Warmack RJ, Chilcott DW, Sharp SL, Ferrell TL. Photon scanning tunneling microscopy. *Rev Sci Instrum*. 1990;61(12):3669–77.
71. Tsai DP, Jackson HE, Reddick RC, Sharp SH, Warmack RJ. Photon scanning tunneling microscope study of optical waveguides. *Appl Phys Lett. AIP Publishing*; 1990;56(16):1515–7.
72. Labani B, Girard C, Courjon D, Labeke D Van. Optical interaction between a dielectric tip and a nanometric lattice: implications for near-field microscopy. *JOSA B. Optical Society of America*; 1990;7(6):936–43.
73. Prieve DC, Walz JY. Scattering of an evanescent surface wave by a microscopic dielectric sphere. *Appl Opt*. 1993;32(9):1629–41.
74. Helden L, Eremina E, Riefler N, Hertlein C, Bechinger C, Eremin Y, et al. Single-particle evanescent light scattering simulations for total internal reflection microscopy. *Appl Opt. Optical Society of America*; 2006;45(28):7299–308.
75. Kawano Y, Higgins C, Yamamoto Y, Nyhus J, Bernard A, Dong HW, et al. Darkfield Adapter for Whole Slide Imaging: Adapting a Darkfield Internal Reflection Illumination System to Extend WSI Applications. *PLoS One*. 2013;8(3).

Appendix I Derivation of evanescent field depth

A schematic of the propagation vectors \mathbf{k} is displayed as Figure I.1, where a plane wave travels from layer 1 with refractive index of n_1 , at an incident angle of θ_i to layer 2, with refractive index of n_2 with a transmitted angle of θ_t .

\mathbf{k}_1 represents the reflected wave vector and \mathbf{k}_2 represents the transmitted propagation vector. k_{1x} and k_{2x} are the x-components of the respective wave vectors, while k_{1z} and k_{2z} are the z-components of the respective wave vectors. k_0 is the magnitude of the initial propagation vector, where $k_0 = 2\pi/\lambda$.

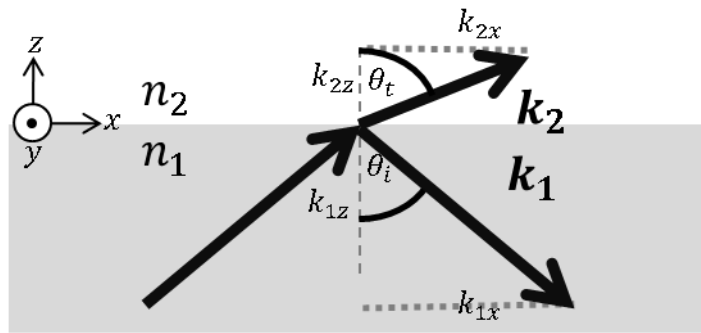


Figure I.1 A schematic of a beam of light striking the boundary of two mediums. \mathbf{k}_1 and \mathbf{k}_2 are propagating vectors of the reflected beam and transmitted beam respectively.

The following set of equations can be derived from the vector triangles:

$$k_{2z}^2 = \mathbf{k}_2^2 - k_{2x}^2 = n_2^2 k_0^2 - k_{2x}^2$$

Eq. I.1

$$k_{2x} = \frac{\sin \theta_t}{k_2}$$

Eq. I.2

Using Snell's Law, Eq. I.2 becomes

$$k_{2x} = n_1 k_0 \sin \theta_i$$

Eq. I.3

Placing Eq.I.3 into Eq.I.1

Eq. I.4

$$(k_{zz})^2 = n_2^2 k_0^2 - n_1^2 k_0^2 \sin^2 \theta_i = k_0^2 (n_2^2 - n_1^2 \sin^2 \theta_i)$$

Eq. I.5

The expression suggests if $n_2 < n_1 \sin \theta_t$, then $(k_{zz})^2$ is negative and k_{zz} becomes imaginary. Assuming this is the case, this can be written as:

$$k_{zz} = \pm i\beta = \pm \sqrt{-1} \sqrt{k_0^2 (n_1^2 \sin^2 \theta_i - n_2^2)}$$

Eq. I.6

Placing this back into the transmitted electric field vector:

$$\mathbf{E}_2 = E_{0,2} e^{i(\mathbf{k}_2 \cdot \mathbf{r} - \omega t)} = E_{0,2} e^{i(k_{zz}z + k_x x - \omega t)} = E_{0,2} e^{\pm \beta z} e^{i(k_x x - \omega t)}$$

Eq. I.7

Where,

\mathbf{E}_2 is the transmitted electric field vector

$E_{0,2}$ is the maximum amplitude of the electric field

\mathbf{k}_2 is the wave vector, $\mathbf{k}_2 = k_{zz} \mathbf{i} + k_x \mathbf{j}$

\mathbf{r} is the position vector, $\mathbf{r} = z \mathbf{i} + x \mathbf{j}$

t is time

ω is the angular temporal frequency with $\omega = 2\pi f$, where f is the frequency

Taking only the amplitude and its decay component:

$$E_2 = E_{0,2} e^{\pm \beta z}$$

Eq. I.8

Depending on the sign of β , the z component can increase or decrease exponentially and since it is not possible for the electric field to increase exponentially with distance, β has to be negative. Based on the definition of evanescent field depth, the amplitude of the electric field $E_{0,2}$ decays to the value of $1/e$ when:

$$z = \frac{1}{\beta} = \frac{1}{\sqrt{k_0^2(n_1^2 \sin^2 \theta_i - n_2^2)}} = \frac{\lambda}{2\pi\sqrt{(n_1^2 \sin^2 \theta_i - n_2^2)}}$$

Eq. I.9

The reflected coefficient($r_{s,p}$) beyond the critical angles can be derived from Fresnel equations and written in exponential form:

$$r_{s,p} = \left(\frac{E_{0r}}{E_{0i}} \right)_{s,p} = e^{i2\phi_{s,p}}$$

Eq. I.10

Where,

E_{0r} is the amplitude of the reflected electric field

E_{0i} is the amplitude of the initial electric field

Subscripts s,p represents s-polarisation or p-polarisation

$$\phi_s = \tan^{-1} \left(\frac{\beta}{k_{1z}} \right) = \tan^{-1} \left(\sqrt{\frac{n_1^2 \sin^2 \theta_i - n_2^2}{n_1^2 \cos^2 \theta_i}} \right)$$

Eq. I.11

$$\phi_p = \tan^{-1} \left(\frac{n_1^2 \beta}{n_2^2 k_{1z}} \right) = \tan^{-1} \left(\frac{n_1^2}{n_2^2} \sqrt{\frac{n_1^2 \sin^2 \theta_i - n_2^2}{n_1^2 \cos^2 \theta_i}} \right)$$

Eq. I.12

This shows the amplitude remains to be unchanged after reflection, no energy is loss and phase change upon reflection is $2\phi_{p,s}$.

References

Pedrotti FL, Pedrotti LM, Pedrotti LS. *Introduction to Optics*. Third edition. London. Pearson's Education; 2007.

Cronin NJ. *Microwave and optical waveguides*. London. Institute of Physics; 1995.

Hecht E. *Optics*. Fourth Edition. Addison Wesley; 2002.

Appendix II Equations for three-layer transmittance model

$$T = \frac{1}{\alpha \sinh^2 y + \beta}$$

$$y = \frac{2\pi n_1 d \sqrt{(N^2 \sin^2 \theta_i - 1)}}{\lambda_0}$$

$$\alpha_s = \frac{(N^2 - 1)(n^2 N^2 - 1)}{4N^2 \cos \theta_i (N^2 \sin^2 \theta_i - 1) \sqrt{(n^2 - \sin^2 \theta_i)}}$$

$$\beta_s = \frac{(\sqrt{n^2 - \sin^2 \theta_i} + \cos \theta_i)^2}{4 \cos \theta_i \sqrt{n^2 - \sin^2 \theta_i}}$$

$$\alpha_p = \frac{\alpha_s}{n^2} \{(N^2 + 1) \sin^2 \theta_i - 1\} \{(n^2 N^2 + 1) \sin^2 \theta_i - n^2\}$$

$$\beta_p = \frac{(\sqrt{n^2 - \sin^2 \theta_i} + n^2 \cos \theta_i)^2}{4n^2 \cos \theta_i \sqrt{n^2 - \sin^2 \theta_i}}$$

$$n = \frac{n_2}{n_1}, N = \frac{n_1}{n_3}$$

n_1, n_2, n_3 are refractive indices of layer 1, layer 2 and layer 3 respectively.

θ_i is the angle of incidence

λ_0 is the wavelength of the light source

d is the thickness of layer 2

α_s, β_s are parameters for s-polarisation

α_p, β_p are parameters for p-polarisation

T is the transmittance

Appendix III Demonstration of the uneven surface of the waveguide edge

The edges of the waveguides used for the evanescent field characterisation experiment was found to be uneven. The effect of the uneven surface was demonstrated by shining a collimated laser beam to the edge of the waveguide and a camera placed at the other end to record the image. A slit was placed between the first edge of the waveguide and the laser to restrict the area of illumination onto the edge of the waveguide. In addition, glass coverslips were placed at the first edge and/or second edge of the waveguide using immersion glass to match the index of the glass. Images were taken to record the effect. A schematic diagram of the setup is displayed in the figure below:

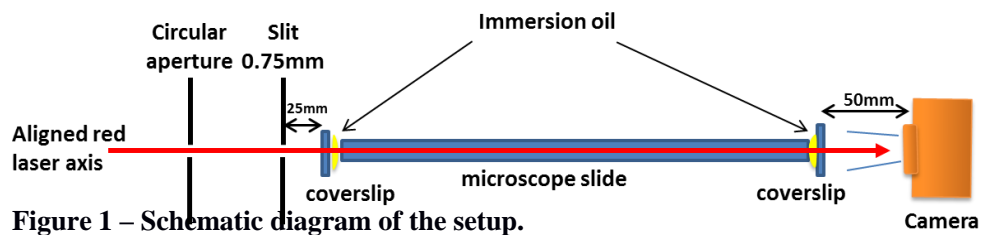


Figure 2 shows the images captured after the beam of laser has passed through various components. Using Figure 2A as the reference image with no waveguide in the path, the effect of the uneven surface of the waveguide can be seen in Figure 2B. The change in the light distribution from a collimated beam suggests this can also change the angle within waveguide after passing through the first edge. Hence, the inconsistent results from characterising the evanescent field profile using LED source could be explained by this. Improvements to the surface can be made by coupling the edge of the waveguide with immersion oil and a flat coverslip and the results are apparent in Figures 2C/D. The result of this has led to the use of polished edges for future experiments.

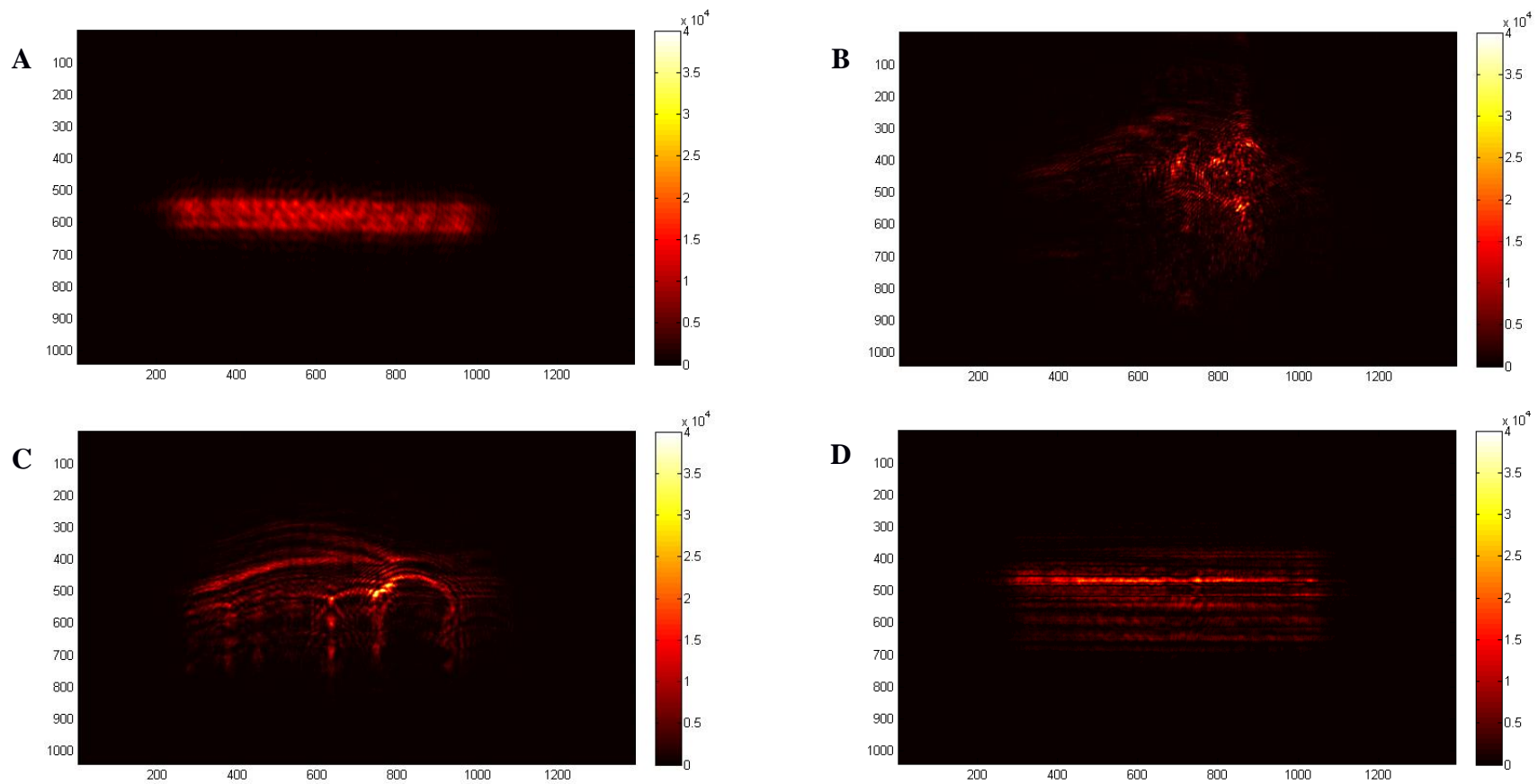


Figure 2 A) Image of laser beam passing through a 0.75mm slit. B) Image of laser beam passing through a 0.75mm slit and through the edges of the waveguide. C) Image of laser beam after passing through a 0.75mm slit and the edges of the waveguide where a coverslip was placed on one edge using immersion oil. D) Image of a laser beam after passing through a 0.75mm slit and the waveguide with both edges coupled to a glass coverslip using immersion oil. Axes of image are in pixels; 100pixels \approx 546 μ m. Colour bar to the right of each image represents the intensity level.

Appendix IV Ray tracing inside waveguide for incident angle below the critical angle

When a ray of light strikes the edge of the waveguide, there can be two outcomes and the result is dependent on the angle of incidence and the refractive indices of the material. The outcome can be calculated simply using Snell's Law. Figure 1 is a schematic diagram of a light ray entering the waveguide and it is shown to clarify the terms used in the section that follows.

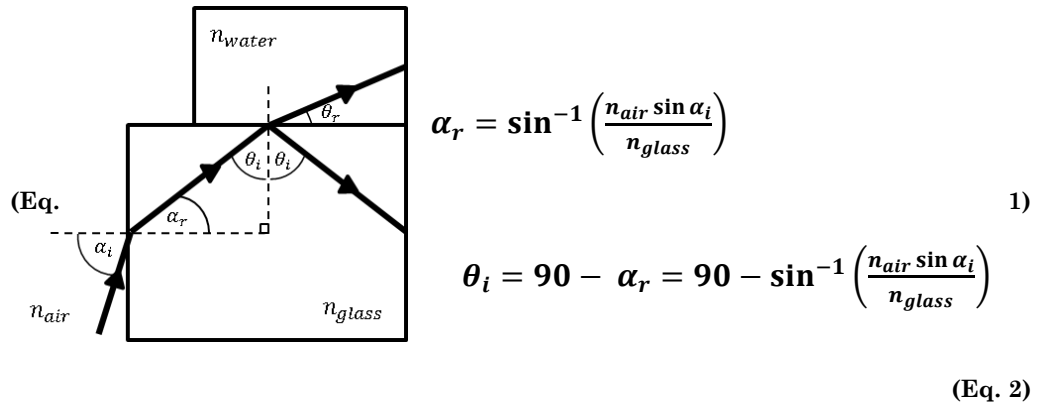


Figure 1 Schematic diagram of the waveguide with glass as the waveguide layer and water layer, where the sample will be placed. Illumination source is coupled from the left hand side of the waveguide and the refracted angle (α_r) is translated into θ_i normal to the surface of the slide

Case one

$\theta_i < \theta_{crit.glass \rightarrow water}$ – The incidence angle is smaller than the critical angle of glass and water, so light refracts out of the glass slide into the water layer. Depending on θ_i , the wave can either refract out of the water layer into air, or reflect internally back into the water layer and the glass slide. A full evaluation of the possible angular range at the interface is discussed later.

Case two

$\theta_i > \theta_{crit.glass \rightarrow water}$ – The incidence angle is greater than the critical angle of glass and water. This means the condition for total internal reflection is satisfied and an evanescent field is present in the lower refractive index side of the interface. In this case, the evanescent field is located in the water layer from the glass/water interface. The nature of an evanescent field is that its amplitude

decays exponentially as it is displaced further into the water layer. Therefore, only object of interest that is proximal to the glass surface is illuminated.

The critical angles between different layers calculated using Snell's Law are summarized in the following table:

Material 1, n_{in}	Material 2, n_{out}	Critical angle, θ_{crit} (deg.)
Glass, $n = 1.51$	Air, $n=1.00$	41.47°
Glass, $n=1.51$	Water, $n=1.33$	61.74°
Water, $n=1.33$	Air, $n=1.00$	48.75°

Table 1. Critical angles for different refractive indices

An examination of the possible angles that can be coupled into the slide starting from the illumination source can be calculated based on Snell's Law and simple geometry as depicted in figure 1. Starting with an illumination source containing a possible range of angle of incidence α_i ($0^\circ \geq \alpha_i \geq 89.99^\circ$), the range of angles refracted in the glass slide is $0^\circ \geq \alpha_r \geq 41.47^\circ$. When the ray approaches the surface of the slide, θ_i lies within the range of 48.53° to 89.99° .

$$0^\circ \geq \alpha_i \geq 89.99^\circ$$

$$0^\circ \geq \alpha_r \geq 41.47^\circ$$

$$48.53^\circ \geq \theta_i \geq 89.99^\circ$$

In order to demonstrate the refraction of light wave out of the water/air layer, the refracted angle in the water layer needs to be less than the critical angle for water/air interface ($\theta_r < 48.75^\circ$, $\theta_i < 41.47^\circ$). However, since the minimum angle of incidence, $\theta_{i_{min}} = 48.53^\circ$, $\theta_{r_{min}} = 58.29^\circ$, which is greater than $\theta_{crit.wawter \rightarrow air} = 48.75^\circ$. This concludes that it is not possible for any wave to refract out of the water layer into air. Furthermore, for any wave that refracts into the water layer from the glass layer, the wave will always result in total internal reflection back into the water layer and may refract back into the glass slide depending on its displacement from the edge of the water region. This is one form of sample illumination that is not the evanescent field.

For total internal reflection to be satisfied, the angle of incidence must be above the critical angle for glass/water interface ($\theta_i > 61.74^\circ, \alpha_r < 28.26^\circ, \alpha_i < 45.63^\circ$) to produce an evanescent field with amplitude that decays exponentially in the water layer of the glass/water interface.

In summary, coupling light wave from the perpendicular edge from the surface yields two possible outcomes of illumination at the glass/water interface:

- 1 Total internal reflection illumination in the water layer and does not have the property of depth discrimination because the illumination is assumed to be uniform throughout the propagation of a collimated beam. This is will be addressed as propagating wave illumination.
- 2 Evanescent field illumination generated from glass/water interface where the amplitude of the field decays exponentially as it is displaced further into the water layer.

The two types of illumination for a collimated beam are illustrated in Figure 2:

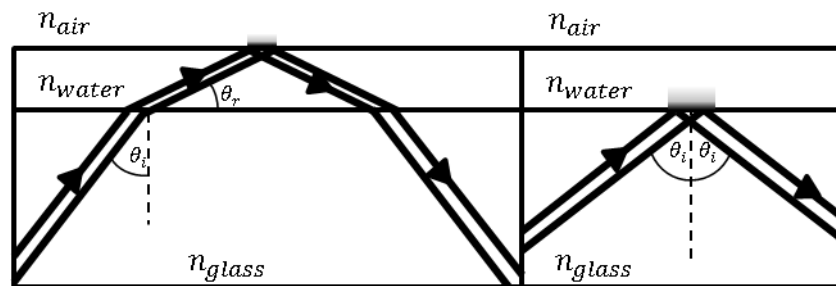


Figure 2 An illustration of the two possible types of illumination. Propagating light illumination (left) and evanescent field illumination (right)

Appendix V Effects of analysis window size on the evanescent field depth

A tungsten tip was used as a tip to scatter the evanescent field at 20nm displacement steps away from the glass/water interface. The scattered intensity at each step was captured by a X8 magnification microscope system and the intensity of probe on each image was plotted against the displacement from the interface.

To analyse the intensity-displacement profile of the probe, the area of the scattered intensity on the image is located based of the maximum intensity value and the change of intensity between the initial images. The effect of analysis window size on the evanescent field depth was examined by fitting the normalised intensity-displacement profile with either a simple exponential model $I(z) = e^{-bz}$ or a double exponential model $I(z) = A * e^{-bz} + C * e^{dz}$.

The evanescent field experiment was carried out using the glass waveguide under two conditions as described in the methods of section 4.2.1 . One data set from each condition was chosen for the window size analysis and data points close to the interface were omitted in this analysis for a better exponential fit.

Fit Model	Unmodified slide		Black Silicone Slide	
	exp(-bz)	a*exp(-bz) + c*exp(dz)	exp(-bz)	a*exp(-bz) + c*exp(dz)
<i>n</i> by <i>n</i> pixels	Evanescent Field Depth (nm)		Evanescent Field Depth (nm)	
1	156	137	229	221
3	156	141	233	217
5	158	146	220	213
7	159	147	227	209
9	162	150	228	207
21	167	148	229	206
201	N/A	158	6911*	210
Range	11	17	13	15
SD	4	6	4	6

*omitted from range and SD calculation

The evanescent field depths are displayed in the table above. Increasing the analysis window size on unmodified slides also increased the exponential field

depth of up to 7% and 9% using a single exponential fit and double exponential fit respectively. Whereas for silicone waveguides, the change in evanescent field depth was up to -3% for a single exponential fit and -9.8% for a double exponential fit.

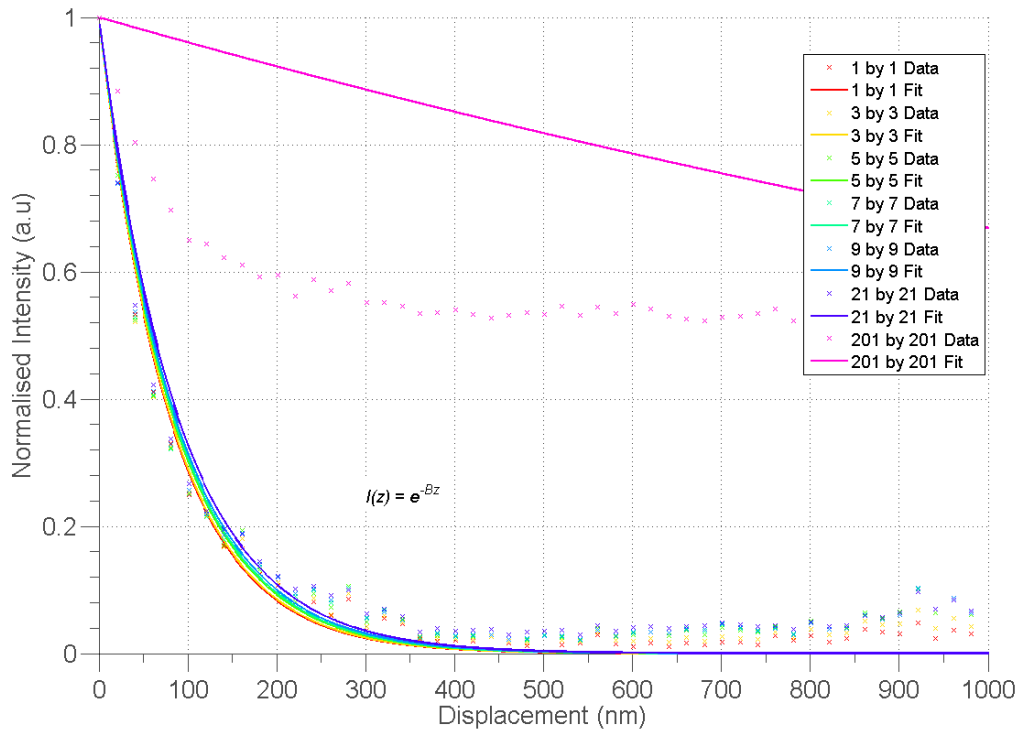
As a result of increasing the analysis window size, the intensity baseline at large displacement distances away from the interface was also increased and can be observed most obviously when the analysis window size was increased to 201 by 201 pixels. The increase in the baseline level can be explained by fixed intensity level on the image with respect to the displacement. One potential source of the baseline could be the unremoved particles on the surface of the slide and a larger analysis window size will include more signals resulting from these particles. The increase in baseline level can hide the exponential decay as shown in figures below.

The range of the evanescent field depth is within 17nm and this is within the step size of 20nm. The standard deviation is 4nm and 6nm for the single exponential model and double exponential model respectively. This suggests that the analysis window size below 21 by 21 pixels has little effect on the evanescent field depth.

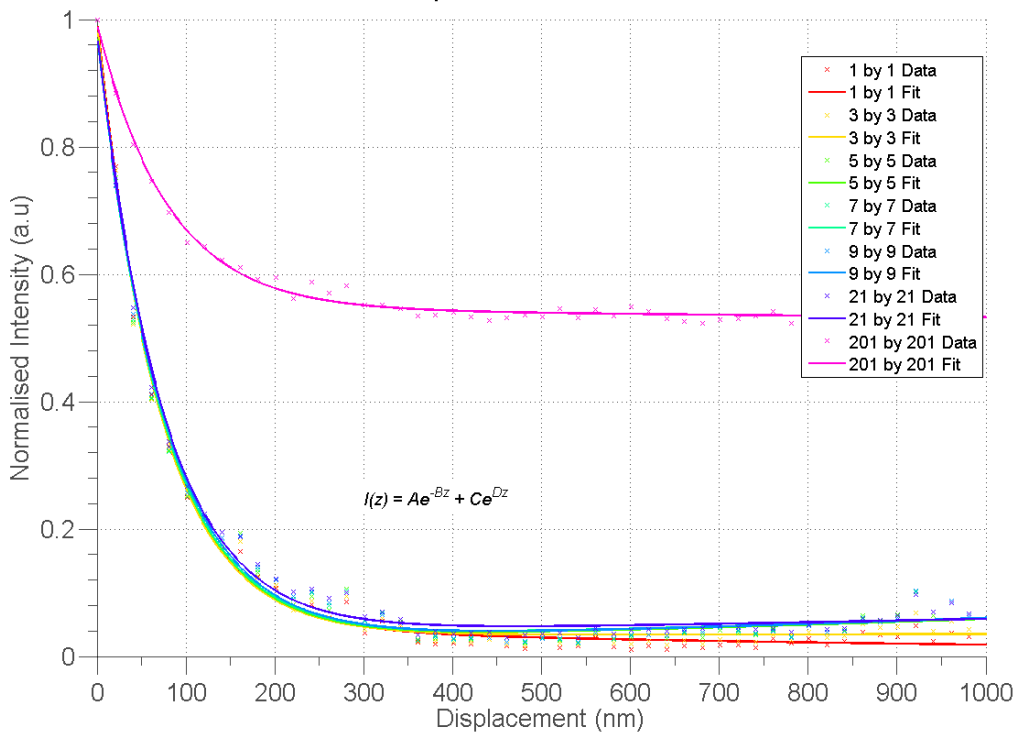
The goodness of fit based on R^2 values are displayed in the table below.

Fit Model	Unmodified slides		Black Silicone Slides	
	$\exp(-bz)$	$a*\exp(-bz) + c*\exp(dz)$	$\exp(-bz)$	$a*\exp(-bz) + c*\exp(dz)$
<i>n</i> by <i>n</i> pixels	R value		R value	
1	0.9807	0.9938	0.9952	0.9972
3	0.968	0.991	0.996	0.9975
5	0.9462	0.9875	0.9966	0.998
7	0.9433	0.9875	0.9957	0.998
9	0.9447	0.9884	0.99943	0.9979
21	0.9392	0.9911	0.9656	0.9975
201	NA	0.9868	-2.749	0.9763

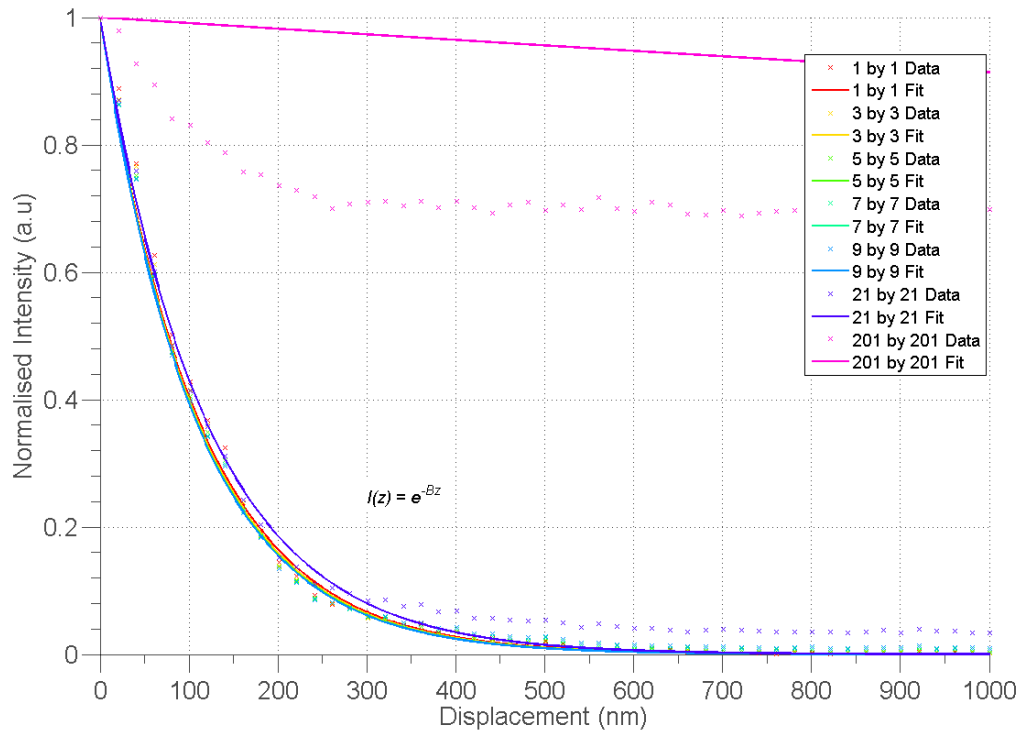
Effects of Analysis Window Size on the Evanescent Field Depth e^{-Bz}
 Plain slide | Glass/Water | $\theta_1 = 68.1^\circ$ | 635nm | Normalised



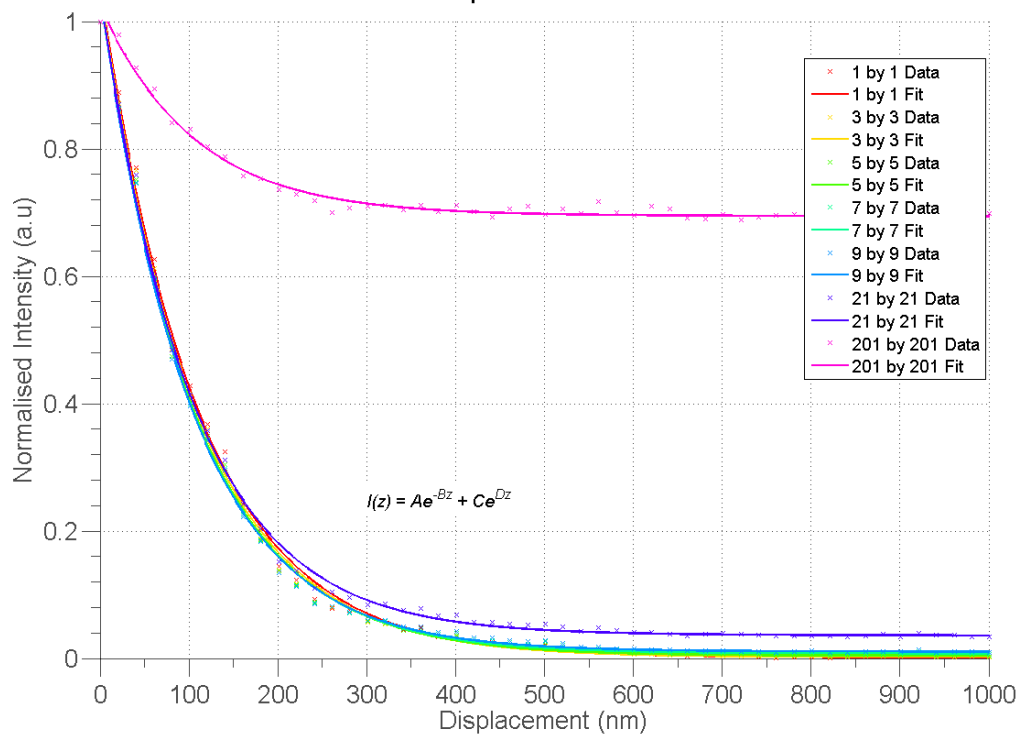
Effects of Analysis Window Size on the Evanescent Field Depth $Ae^{-Bz} + Ce^{Dz}$
 Plain slide | Glass/Water | $\theta_1 = 68.1^\circ$ | 635nm | Normalised



Effects of Analysis Window Size on the Evanescent Field Depth e^{-Bz}
 Silicone slide | Glass/Water | $\theta_i = 68.1^\circ$ | 635nm | Normalised



Effects of Analysis Window Size on the Evanescent Field Depth $Ae^{-Bz} + Ce^{Dz}$
 Silicone slide | Glass/Water | $\theta_i = 68.1^\circ$ | 635nm | Normalised



**Appendix VI Normalised mean intensity and
standard deviation used to calculate the coefficient of
variation in the three clusters**

Normalised Mean intensity						
Image	Bright-field			Waveguide		
	Cluster 1	Cluster 2	Cluster 3	Cluster 1	Cluster 2	Cluster 3
t = 100	0.500	0.517	0.693	0.283	0.173	0.310
t = 110	0.516	0.475	0.695	0.336	0.311	0.333
t = 120	0.568	0.414	0.661	0.305	0.217	0.268
t = 325	0.536	0.654	0.491	0.335	0.234	0.293

Standard Deviation						
Image	Bright-field			Waveguide		
	Cluster 1	Cluster 2	Cluster 3	Cluster 1	Cluster 2	Cluster 3
t = 100	0.198	0.156	0.132	0.166	0.126	0.180
t = 110	0.183	0.143	0.132	0.186	0.168	0.181
t = 120	0.183	0.152	0.156	0.169	0.149	0.157
t = 325	0.159	0.103	0.189	0.170	0.148	0.179

Appendix VII Results for tracked particles 5, 6 & 7

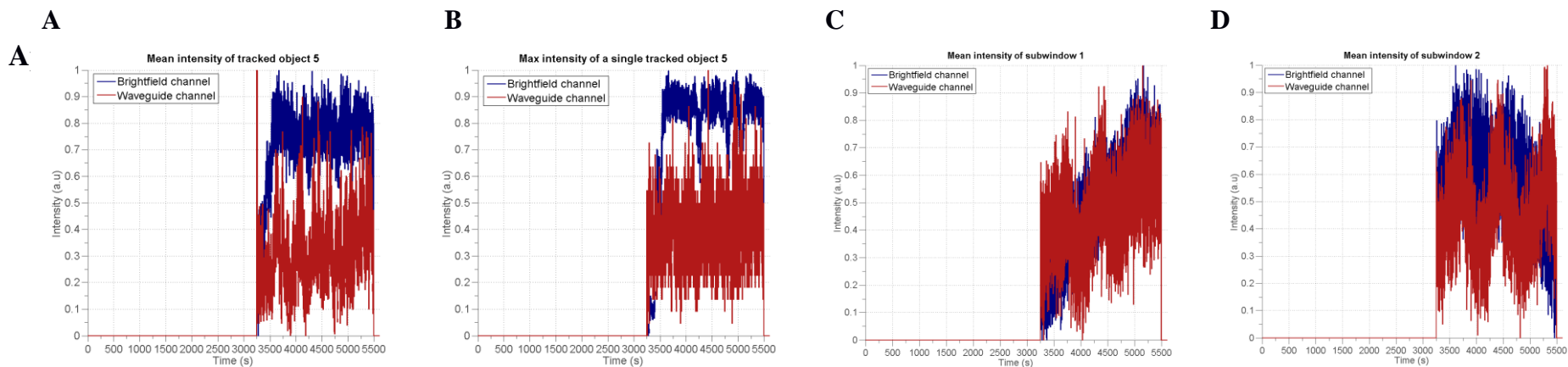


Figure VIII.1 Tracked object 5 – A - Mean intensity of the tracked object vs. time in both bright-field and waveguide channels. B - Maximum intensity of the track object against time. C , D - Mean intensity of subWindow1 and subWindow2 outside the trajectory of the tracked object, arrows indicate time points where solution dried out. E - Area of the tracked object against time. F - Path taken by the tracked object in orange.

Table VIII.1 Data statistics of the tracked object throughout its tracked path in both brightfield(BF) and waveguide(WG) channels. STD = Standard deviation; CV = coefficient of variation.

	Data statistics of the tracked object across the tracked path							
	Mean(a.u)		STD(a.u)		Range		CV	
	BF	WG	BF	WG	BF	WG	BF	WG
A. Mean intensity of tracked object	0.729	0.313	0.132	0.138	3060	67.2	0.181	0.442
B. Max intensity of tracked object	0.783	0.378	0.220	0.120	18768	352	0.281	0.318
C. Mean intensity of subWindow1	0.498	0.468	0.188	0.150	284	14	0.377	0.321
D. Mean intensity of subWindow2	0.556	0.451	0.151	0.155	239	16.3	0.272	0.343

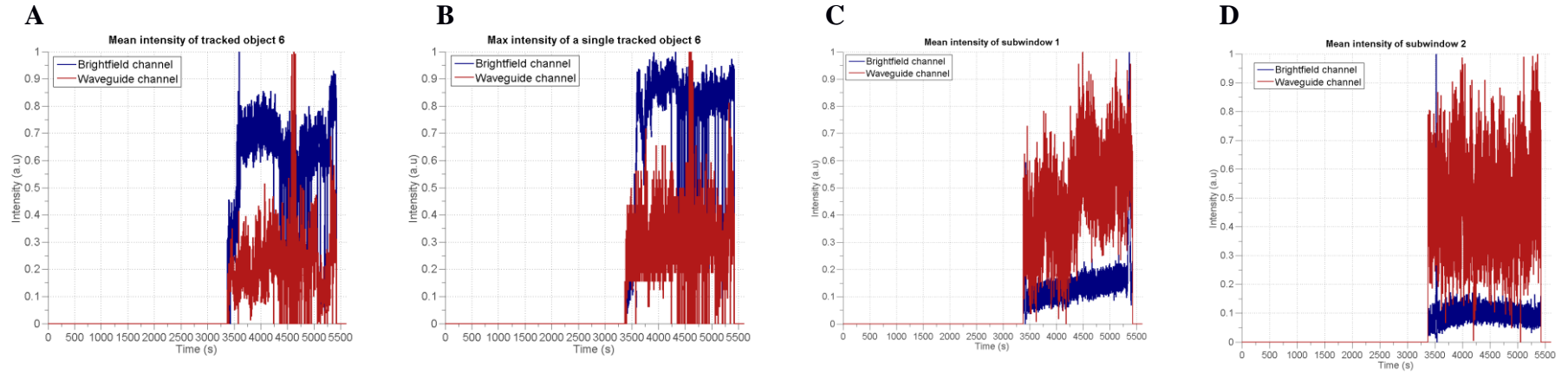
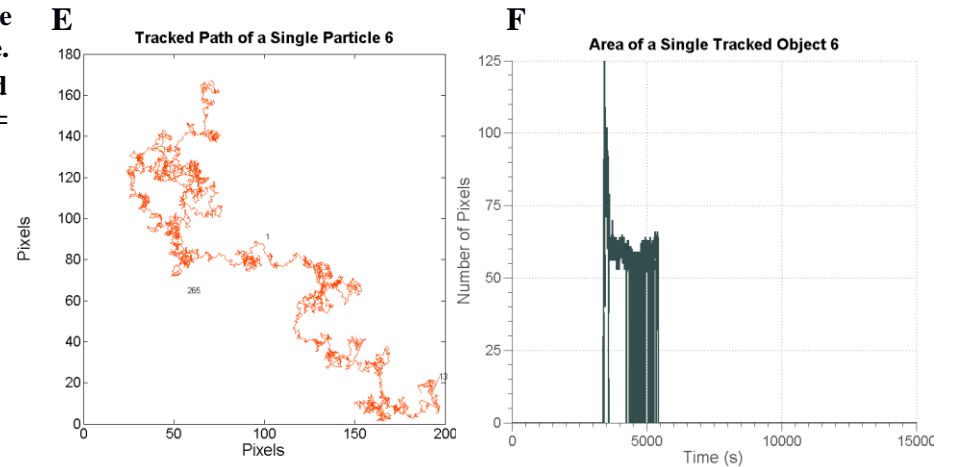


Figure VIII.2 Tracked object 6 – A - Mean intensity of the tracked object vs. time in both bright-field and waveguide channels. B - Maximum intensity of the track object against time. C , D - Mean intensity of subWindow1 and subWindow2 outside the trajectory of the tracked object, arrows indicate time point where solution dried up. E - Area of the tracked object against time. F - Path taken by the tracked object in orange.

Table VIII.2 Data statistics of the tracked object throughout its tracked path in both bright-fied(BF) and waveguide(WG) channels. STD = Standard deviation; CV = coefficient of variation.

	Data statistics of the tracked object across the tracked path							
	Mean(a.u)		STD(a.u)		Range		CV	
	BF	WG	BF	WG	BF	WG	BF	WG
A. Mean intensity of tracked object	0.640	0.230	0.132	0.117	7409	101	0.207	0.508
B. Max intensity of tracked object	0.776	0.313	0.212	0.112	27296	528	0.273	0.356
C. Mean intensity of subWindow1	0.142	0.469	0.092	0.157	1422	14.7	0.645	0.335
D. Mean intensity of subWindow2	0.095	0.485	0.046	0.150	2223	13.6	0.488	0.310



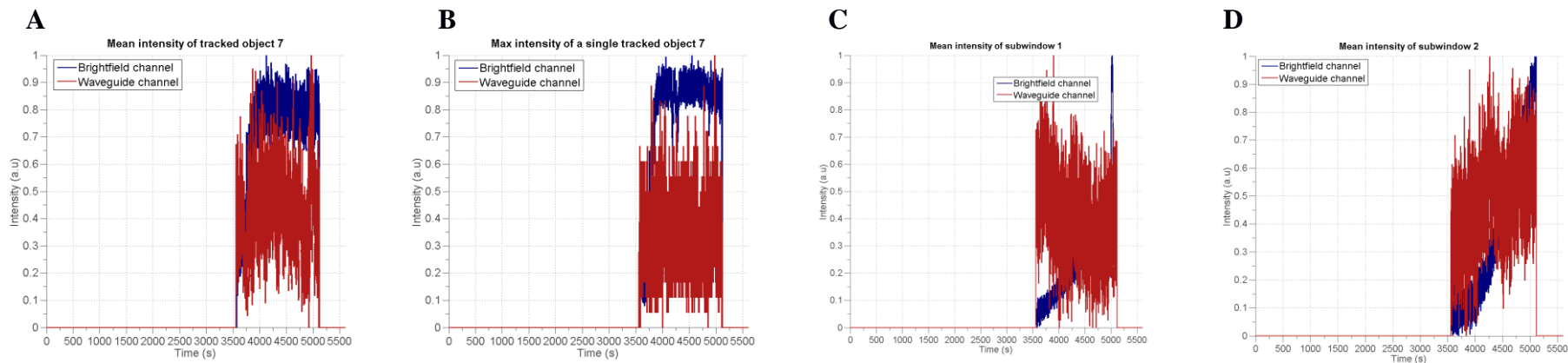
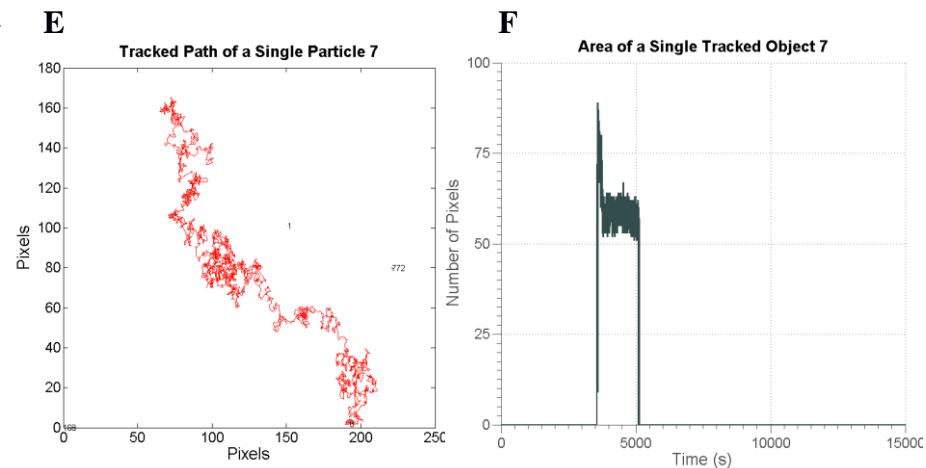


Figure VIII.3 Tracked object 7 – A - Mean intensity of the tracked object vs. time in both bright-field and waveguide channels. B - Maximum intensity of the track object against time. C , D - Mean intensity of subWindow1 and subWindow2 outside the trajectory of the tracked object, arrows indicate time point where solution dried up. E - Area of the tracked object against time. F - Path taken by the tracked object in red.

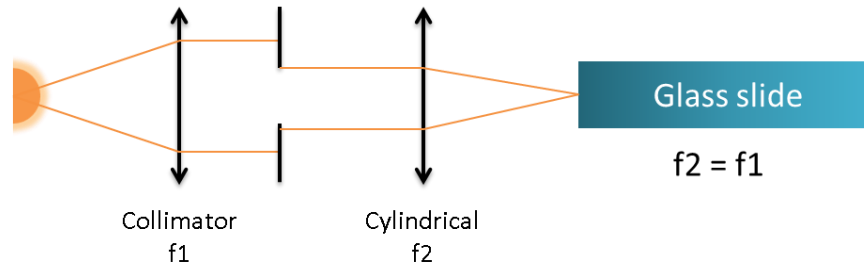
Table VIII.3 Data statistics of the tracked object throughout its tracked path in both bright-field(BF) and waveguide(WG) channels. STD = Standard deviation; Range – difference between max and min intensity over time.CV = coefficient of variation.

	Data statistics of the tracked object across the tracked path							
	Mean(a.u)		STD(a.u)		Range		CV	
	BF	WG	BF	WG	BF	WG	BF	WG
A. Mean intensity of tracked object	0.723	0.425	0.170	0.147	7007	57.4	0.235	0.346
B. Max intensity of tracked object	0.769	0.327	0.232	0.131	25744	38.4	0.302	0.400
C. Mean intensity of subWindow1	0.218	0.409	0.135	0.151	1033	12	0.619	0.368
D. Mean intensity of subWindow2	0.375	0.484	0.273	0.157	791	13	0.726	0.325

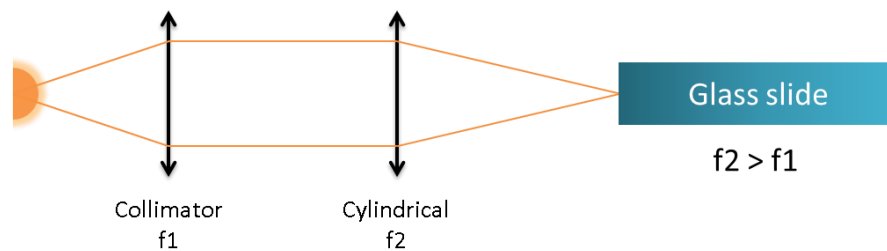


Appendix VIII Restriction of the incident angles produced by an LED source

Two configurations to control the range of angles produced by the source are displayed below.



In this configuration, the light source is collimated by placing the source at one times the focal length of the f_1 lens in front of f_1 lens. An aperture is placed at one times the focal length of the f_1 lens behind f_1 lens. A second lens, f_2 , with the same focal length of f_1 is placed at one times the focal length after the aperture to focus the plane where the aperture lies onto the edge of the slide.



In the second case, the focal length of the second lens is greater than the first lens, which results in a smaller range of angles being focused onto the edge of the slide.

LEDs are considered as an extended source, meaning the apparent source size is large opposed to a laser which is a point source. This means it is difficult to achieve a fully collimated beam because light is emitted from multiple point sources.